

Engineering entanglement for metrology using rotating matter waves

Luís Manuel Rico Gutiérrez

Submitted in accordance with the requirements for the degree of
Doctor of Philosophy

The University of Leeds

School of Physics and Astronomy

October 2013

The candidate confirms that the work submitted is his/her own, except where work which has formed part of jointly-authored publications has been included. The contribution of the candidate and the other authors to this work has been explicitly indicated below. The candidate confirms that appropriate credit has been given within the thesis where reference has been made to the work of others.

Chapter 4 and some parts of Chapter 3 are based on a jointly authored paper with my supervisor Jacob Dunningham and my second supervisor Tim Spiller. I am responsible for all calculations, figures, and most of the text. The coauthors provided valuable consultation, comments, feedback and some of the text. *Paper:* Rico-Gutierrez, L. M. and Spiller, T. P. and Dunningham, J. A. “Engineering entanglement for metrology with rotating matter waves”. *New Journal of Physics* **15**, 1367 (2013).

The material in chapter 5 that has not appeared in print is currently being prepared for publication. This is an interferometric scheme proposal which is the result of research carried out by me and both of my supervisors Jacob Dunningham, and Tim Spiller.

This copy has been supplied on the understanding that it is copyright material and that no quotation from the thesis may be published without proper acknowledgement.

©2013 The University of Leeds and Luis Manuel Rico Gutierrez

Acknowledgements

I would like to begin by thanking my supervisor Jacob Dunningham for all his support during my Ph.D. He is the prototype of an excellent supervisor, always looking after his students, providing advice, encouragement and making sure we had everything we needed in order to conduct our research in the best conditions. I am particularly grateful with him for providing a great balance between my independent ideas and his suggestions, he always made me feel that I was going in the right direction with my questions and ideas. I am equally grateful with my second supervisor Tim Spiller, because as busy as he is, being the head of the QI group, he always showed interest in the project and gave valuable contributions based on his ample experience.

I have had a wonderful time as part of the QI group in Leeds, and this is mainly due to the friendly atmosphere provided by my peers. I want to thank Suvabrata De, Shane Dooley, Oleg Kim, Paul Knott, Abbas Al-Shimary, Adam Stokes, Veiko Palge, Jaewoo Joo, James De Lisle, Tom Barlow, and Tim Proctor, for the very interesting and entertaining chats during lunch time, excellent discussions in our “interferometral” (informal) seminars, fun times at the pub, and gratifying times playing football with some of them.

Outside the office, I am in great debt with friends who made me feel at home at different times during my stay in Leeds. A big “thank you” goes to my NHH family, Maggie, David, Pedro, Yomar, Andy and Melissa; as well as Abdulmalik, Mimi and Denis; I had some of the happiest moments of my life in that house. Also, I want to express my gratitude with my friends Sol, Maria, Cristhian, Sam and Cecy, who were very kind with me and helpful in many occasions.

Special thanks to my best friends, Pablo de la Peña, Israel Trujillo, and Bernardo Rico, who have always believed in me, unconditionally. Also, I want to thank my other very good friends who have helped to shape my personality towards my strengths: José Luis López, Clifford Compeán, Pedro Ruíz, Fernando Heinz, and Roger Vega.

I am greatly thankful for my family back in Mexico, they have given me the best of support, encouragement, and unconditional love. I want to thank my brothers Gerardo, and David, as well as my sister Cecilia and their families for everything they have given me, even if some times I do not reciprocate in the same way, I love them all and I could not have wished for a better family. I always received the same support and love from other members of my family, Los Rico and Los Gutiérrez, thanks for letting me make you feel proud of me.

Above all, I want to express a very special gratitude to my best source of inspiration in life, my Mother; her noble and selfless personality I have always admired and many times has humbled me. She is an inexhaustible fountain of love who welcome me and stood by my side during the most tormentous and upsetting period of my life toward the end of my degree. Everything I know about being a better person everyday, I learned it from her. Hence, I want to dedicate this thesis to my Mother and my late Father, who I know would have been very proud of my accomplishment.

Last but not least, I want to thank God, who I still have to make good sense of, but whom I undoubtedly felt close to me many times. I will be eternally grateful for he gave me the opportunity to have a closer look at the inner workings of its creation, the ability to understand the language in which he has expressed his *magnum opus* at the atomic scale; it makes me feel extremely privileged to be part of these group of “blessed” people called physicists who represent a tiny part of the World’s population.

Without a doubt, God has written the most beautiful poem with energy and matter, rather than words.

Abstract

We present the first exact diagonalisation study of a rotating Bose-Einstein condensate stirred by a quadratic anisotropic potential near the threshold of the first vortex nucleation beyond the lowest Landau level (LLL) approximation.

Although the nucleation of the first vortex in this system has been the focus of extensive experimental and theoretical research in both mean-field studies, as well as in exact diagonalisation ones, they have all relied on the assumption of the interaction strength being weak enough so that the system is well described by the LLL approximation. The LLL approximation accurately predicts the rotation frequency at which the first vortex penetrates the gas, and correctly describes the appearance of a quantum phase transition at a critical rotation frequency Ω_c , which leads to quantum correlations between the atoms and entanglement in the ground state at Ω_c .

However, our research shows that the LLL approximation fails at describing the details of the entangled state and the quantum Fisher information, which bounds the accuracy of phase measurements in metrology schemes, even for weak interactions. Our results reveal a rich system that allows for the engineering of different promising entangled states for quantum metrology, which are also amenable to experimental investigation.

Finally, we propose an interferometric scheme that makes use of these entangled states, which is shown to have the potential of delivering nearly Heisenberg-limited precision for the measurement of small rotations. The scheme is conceptually very simple, and it is also within reach of current experimental technologies.

Contents

1	Introduction	1
1.1	Quantum metrology	3
1.2	Bose–Einstein condensation	6
1.3	Thesis overview	12
2	Preliminaries	14
2.1	Mach–Zehnder interferometer	14
2.2	Precision scaling for well-known input states	17
2.2.1	Uncorrelated and classical states	19
2.2.2	Yurke state	21
2.2.3	$N00N$ state	22
2.2.4	Bat state	25
2.3	Quantum Fisher information	28
2.4	Particle loss	31
2.5	Rotating Bose–Einstein condensates	32
2.5.1	Rapidly rotating condensates	34
3	Bose–Einstein condensate in an anisotropic rotating trap	36
3.1	Model	37
3.1.1	Solving the single-particle Schrödinger equation	38
3.1.2	Two-dimensional rotating gas	42
3.1.3	Convention for units	44
3.1.4	Non-interacting particles and Landau levels	44
3.2	Quantisation of the Hamiltonian	48
3.2.1	The Lowest Landau Level approximation	51

3.3	Diagonalisation of the Hamiltonian	55
3.3.1	The interacting case	55
3.3.2	The anisotropic case	60
3.3.3	Single particle density matrix	66
3.4	The many-body ground state at criticality	72
3.4.1	Fisher information of the ground state	74
3.5	Conclusions	77
4	Engineering entanglement with rotating matter waves	79
4.1	Tuning entanglement in the rotating trap	80
4.1.1	Quantum Fisher information of the entangled ground states	88
4.2	Assessing the validity of the LLL approximation	90
4.3	Conclusions	99
5	Interferometric scheme for rotation measurements	101
5.1	General overview	102
5.2	Adiabatic nucleation of the entangled state	103
5.3	Non-adiabatic rotation frequency shift and Phase accumulation .	112
5.3.1	Long waiting time regime	115
5.3.2	Short waiting time regime	128
5.4	Conclusions	134
6	Conclusions	136
6.1	Summary	136
6.1.1	Main results	137
6.2	Future work	140
6.2.1	Read-out schemes	140
6.2.2	Sub-shot noise precision without adiabatic nucleation of the entangled state	142
6.2.3	Non-linear phase accumulation	144
6.2.4	Decoherence factors	145
6.2.5	Miscellaneous	146

A	Determination of the Matrix Elements	147
A.1	The anisotropic term	147
A.2	The interaction term	149
References		162

List of Figures

2.1	The Mach–Zehnder interferometer	16
2.2	The quantum beam splitter (QBS)	23
2.3	Probability amplitudes for the bat state.	25
2.4	Mach–Zehnder interferometer with imaginary beam splitters which model the particle losses.	26
2.5	Phase precision in a Mach–Zehnder interferometer with particle losses for different input states.	31
3.1	Energy spectrum of independent bosons in a rotating axisymmetric trap ($A = 0$) for positive total angular momentum $L \geq 0$	45
3.2	Energy spectrum of independent bosons in a rotating axisymmetric trap ($A = 0$) for negative total angular momentum $L < 0$	47
3.3	The many-body Hamiltonian is block diagonal in the basis of definite total angular momentum for a n_{LL} -th Landau level approximation when $A = 0$	48
3.4	Energy spectrum for the case of $N = 6$ interacting particles in the isotropic case ($A = 0$) as a function of the rotation frequency.	57
3.5	Energy spectrum for the case of $N = 6$ interacting particles in the isotropic case ($A = 0$) as a function of the rotation frequency.	58
3.6	Average angular momentum profile of the ground state for $N = 6$ particles as a function of the rotation frequency.	59

LIST OF FIGURES

3.7	Analysis of the amplitudes of the coefficients $ C_k ^2$ for the single-vortex state at Ω_1 in the lowest Landau level approximation. The numbers of particles considered are $N = 6$ (left), and $N = 14$ (right). For both panels the truncation of the basis is $L_{\max} = N + 2$ and $g = 6/N$	60
3.8	Analysis of the angular momentum basis truncation for $N = 6$ particles in the lowest Landau level approximation.	61
3.9	Energy spectrum for the case of $N = 6$ interacting particles in the anisotropic case ($A = 0.03$) as a function of the rotation frequency.	63
3.10	Energy gap between the ground state and the first excited state as a function of the rotation frequency for different values of the interaction strength for $N = 6$ (top) and $N = 12$ (bottom).	64
3.11	Minimal energy gap between the ground state and the first excited state at Ω_{\min} as a function of N for different values of the interaction strength.	65
3.12	Weight of the angular momentum subspaces in the composition of the ground state for $N = 12$ particles and $g = 6/N$	66
3.13	Weight of the angular momentum subspaces in the composition of the ground state for $N = 12$ particles and $g = 6/N$ as a function of the rotation frequency.	67
3.14	Normalised occupations for the three most populated single-particle states of the SPDM as a function of Ω near the critical frequency.	71
3.15	The coefficients $P_n = \langle N - 2n, 2n \Psi_0(\Omega_c) \rangle ^2$ for the two-mode approximation at the critical frequency.	73
3.16	Fisher information for the ground state as a function of the rotation rate for $N = 12$ particles, calculated for the most populated mode of the SPDM at each value of Ω	74
3.17	Phase precision for the entangled ground state at Ω_c as a function of N . The interaction strength is $g = 6/N$ and $A = 0.03$ for all cases.	77
4.1	Energy spectrum as a function of the rotation frequency for $N = 6$ particles as calculated with a two Landau level approximation.	81

LIST OF FIGURES

4.2	Energy spectrum as a function of the rotation frequency for $N = 12$ particles as calculated with a two Landau level approximation. . .	83
4.3	Weight of the angular momentum subspaces in the composition of the ground state at Ω_c for $N = 12$ using a two Landau level approximation and $A = 0.03$	84
4.4	Normalised occupations for the three most populated single-particle states of the SPDM as a function of Ω near the critical frequency using two Landau levels for $N = 12$	85
4.5	Normalised occupations for the three most populated single-particle states of the SPDM as a function of Ω near the critical frequency using two Landau levels for $N = 12$ particles.	86
4.6	The coefficients $P_n = \langle N - 2n, 2n \Psi_0(\Omega_c) \rangle ^2$ for the two-mode approximation at the critical frequency using two Landau levels for $N = 12$ particles.	87
4.7	The coefficients $P_n = \langle N - 2n, 2n \Psi_0(\Omega_c) \rangle ^2$ for the two-mode approximation at the critical frequency using two Landau levels for $N = 12$ particles and two different values of the anisotropy strength.	88
4.8	Minimal energy gap between the ground state and the first excited state at Ω_{\min} as a function of N for different values of the interaction strength.	89
4.9	The quantum Fisher information as a function of the rotation rate Ω for $N = 12$ particles and an anisotropy strength of $A = 0.03$. . .	91
4.10	Phase precision for the entangled ground state at Ω_c as a function of N using two Landau levels. We plot the phase precision for the $N00N$ state $1/N$, bat state $\sqrt{2}/\sqrt{N(N+2)}$, and unentangled particles $1/\sqrt{N}$ for comparison purposes. All the calculations used $A = 0.03$ and a basis truncation of $L_{\max} = N + 2$	92
4.11	The fractional change in the position of the critical rotation frequency Ω_c as a function of the interaction strength for $N = 12$ particles, calculated using two different approximations differing by one Landau level.	93

4.12	The quantum Fisher information of the ground state for various basis truncations as a function of the interaction strength at the critical frequency Ω_c calculated with the respective truncated basis (Method I).	95
4.13	The fractional change in the quantum Fisher information F_Q as a function of the interaction strength, using the LLL approximation and two Landau levels. The Fisher information is calculated at the critical frequency obtained with the respective truncated basis (Method I), and the fractional change is calculated as $\Delta F_Q/F_Q = F_Q(g)_{2LL} - F_Q(g)_{LLL} /F_Q(g)_{2LL}$. The anisotropy strength is $A = 0.03$ for all cases and the horizontal axis is shown for a scaled g by a factor of $N/6$	96
4.14	The fractional change in the quantum Fisher information F_Q as a function of the interaction strength, calculated using two different approximations differing by one Landau level.	97
4.15	Analysis of the Fisher information width with different Landau levels.	98
5.1	Numeric results for the overlap between $ \Psi(t)\rangle$ and the stationary GS for $N = 6$ bosons, $A = 0.03$ and $g = 0.44$	106
5.2	Average total angular momentum of the resulting dynamic state as a function of the rotation frequency for $N = 6$ bosons, $A = 0.03$ and $g = 0.44$	107
5.3	Predicted adiabatic evolution time as a function of the interaction strength for $N = 6, 8, 10$ and 12 particles.	109
5.4	Comparison of the predicted adiabatic evolution time as a function of the interaction strength for $N = 6$ using one and two different linear ramps of the the rotation frequency.	110
5.5	Comparison of the predicted adiabatic evolution time as a function of the interaction strength for $N = 10$ using one and two different linear ramps of the the rotation frequency.	111

LIST OF FIGURES

5.6	Analysis of the factors determining the Fisher information in the regime of $\tau \gg 1$ using two Landau levels for $g = (6/N) \times 1.0$ and $\gamma = 0.46 \times 10^2$ for all cases.	120
5.7	Analysis of the quantum Fisher information in the regime of $\tau \gg 1$ using two Landau levels for $g = (6/N) \times 1.0$ and $\gamma = 0.46 \times 10^2$ for all cases.	121
5.8	Analysis of the factors determining the Fisher information in the regime of $\tau \gg 1$ using two Landau levels for $g = (6/N) \times 0.4$ and $\gamma = 0.46 \times 10^2$ for all cases.	122
5.9	Analysis of the quantum Fisher information in the regime of $\tau \gg 1$ using two Landau levels for $g = (6/N) \times 0.4$ and $\gamma = 0.46 \times 10^2$ for all cases.	123
5.10	Analysis of the factors determining the Fisher information in the regime of $\tau \gg 1$ using two Landau levels for $g = (6/N) \times 0.7$ and $\gamma = 0.46 \times 10^2$ for all cases.	124
5.11	Analysis of the quantum Fisher information in the regime of $\tau \gg 1$ using two Landau levels for $g = (6/N) \times 0.7$ and $\gamma = 0.46 \times 10^2$ for all cases.	125
5.12	Analysis of the factors determining the Fisher information in the regime of $\tau \gg 1$ using two Landau levels for a fixed value of $g = 0.42$ and $\gamma = 0.46 \times 10^2$ for all cases.	126
5.13	Analysis of the quantum Fisher information in the regime of $\tau \gg 1$ using two Landau levels for a fixed value of $g = 0.42$ and $\gamma = 0.46 \times 10^2$ for all cases.	127
5.14	Full numeric calculation of the Fisher information for $g = (6/N) \times 0.44$ and a frequency shift of $\Delta\Omega = -3 \times 10^3$	130
5.15	Full numeric calculation of the scaling of the lower bound for the rotation frequency precision with N for a different number of interaction strengths.	131
5.16	Full numeric calculation of the scaling of the lower bound for the rotation frequency precision with N for a different number of waiting times.	132

LIST OF FIGURES

- 6.1 Non-adiabatic nucleation of the entangled state at the avoided crossing for the case of a $N00N$ state. (Top) A non-adiabatic evolution of the system populates both the ground state and the first excited state at the anticrossing, where the system is allowed to evolve for a time τ . (Bottom) A fast rotation frequency shift away from the anticrossing populates the states $|N0\rangle$ and $|0N\rangle$, and the system undergoes another free evolution which imprints a phase between these two eigenstates that is proportional to N . . . 141
- 6.2 Fisher information obtained for two different angular acceleration values for $N = 6$ particles. The Fisher information is calculated for the state that results after shifting away the rotation frequency from the avoided crossing by an amount of 0.003. The calculation is obtained with two Landau levels, the interaction strength is $gN/6 = 1$, and the anisotropy $A = 0.03$ 142

Chapter 1

Introduction

The concept of entanglement lies at the very core of quantum mechanics. Once dubbed as “spooky action at a distance” by Einstein, it can be considered as the most non-classical feature of the quantum formalism. This central feature was first recognised by Einstein, Podolsky, and Rosen ([Einstein *et al.*, 1935](#)) and Schrödinger ([Schrödinger, 1935](#)) at the beginning of the 20th century. Invariably, due to seemingly bizarre implications of quantum entanglement which are in drastic contrast with concepts from classical physics, as well as its far reaching consequences for the locality and reality of quantum mechanics, the topic of entanglement motivated a great deal of discussion and skepticism among scientists since the early days of quantum mechanics. Already in 1935, Erwin Schrödinger gave a now very famous example of a thought experiment that highlights some of the bizarre consequences of entanglement, particularly when there is a macroscopic system involved. The experiment is the following. A cat and a radioactive atom are placed together inside a sealed box with a mechanism which releases poison when the atom is detected to have decayed, thus killing the cat. If the atom does not decay yet, the poison is not released and the cat gets to live. In modern quantum mechanics jargon, we say that the entire system, cat plus atom, after a duration equal to the half life of the radioactive atom, is in a superposition state of the cat being alive and dead simultaneously, expressed by the state

$$\psi = \frac{1}{\sqrt{2}} [|1\rangle|L\rangle + |0\rangle|D\rangle], \quad (1.1)$$

where $|1\rangle$ represents the state of the undecayed atom, $|0\rangle$ is the state of the decayed one, and live and dead states of the cat are represented by $|L\rangle$ and $|D\rangle$. This superposition state is nowadays referred as an entangled Schrödinger's "cat state", or simply a "cat state".

That an uncertainty originally restricted to the atomic domain translates into a macroscopic indeterminacy is completely out of our normal experience. After all, we do not observe simultaneously dead and alive cats in everyday life, or any other macroscopic superposition for that matter. This is because the indeterminacy implied in the superposition state is finally resolved by the act of observation or measuring, causing the collapse of the wave function. This resolution in itself poses a great dilemma for physicists, which is commonly dubbed as the measurement problem in quantum mechanics (Penrose, 2001). The problem consists in the following: the quantum system which is in a superposition and the measuring device together form a single larger and isolated quantum mechanical system, and thus its evolution must be dictated by the Schrödinger equation; in the same way, the act of measuring collapses the wave function of the open sub-system which is in a quantum superposition, and the full details of this collapse and the measurement process should in principle be derivable solely from the Schrödinger equation for the wave function of the composite system. However, up to this day, there is still disagreement between physicists about whether or not this is possible. Naturally, all the theoretical debate in the early 20th century was more than justified.

It took more than thirty years before the work of John Bell (Bell, 1966) opened the possibility of fundamental questions related to entanglement to be tested experimentally. He derived a set of inequalities involving correlations in experiments involving bipartite systems, that when found to be violated by experimental results, have the implication that entanglement is indeed physical reality. Then, it took another fifteen years until a convincing experimental test of violation of the Bell inequalities was performed by (Aspect *et al.*, 1981). After Aspect *et al.*, many more experimental tests were performed (Kwiat *et al.*, 1995; Ou & Mandel, 1988; Tittel *et al.*, 1998), all of them clearly confirming the predictions of the quantum theory. However, while these results are very convincing, there are pos-

sible loopholes and to date no experiment has simultaneously closed all of these loopholes.

The leading of all these experimental demonstrations opened the door to the exploration of many applications of quantum entanglement, which all demonstrate a “quantum enhancement” over their classical counterparts. Among these key discoveries we find, quantum cryptography (Bennet *et al.*, 1992; Ekert, 1991), quantum dense coding (Bennet & Wiesner, 1992), and quantum teleportation (Bennet *et al.*, 1993; Yurke & Stoler, 1992). All of these discoveries together with the idea of quantum computation (Deutsch, 1985; Feynman, 1982; Shor, 1995) gave birth to a new multidisciplinary area called quantum information (Nielsen & IL, 2000), which has the concept of entanglement as its central focus, being the primary resource which all of these ideas run on.

Among all these new emergent fields which incorporate entanglement as a central notion, we find quantum metrology, an exciting area of quantum physics that deals with accomplishing very precise measurements through the use of entanglement. The research carried out in this thesis pertains to this relatively new area of quantum mechanics, thus we briefly review some of the concepts and advances of this field in the next section. For an all-encompassing review of entanglement in quantum mechanics, (Amico *et al.*, 2008; Horodecki *et al.*, 2009) provide excellent reading material.

1.1 Quantum metrology

Quantum metrology is the collection of ideas, methods, theories and experiments that achieve any kind of quantum enhancement for measuring physical quantities beyond the classical limit (Dunningham, 2006; Giovannetti *et al.*, 2011).

Measurements play an important role in our everyday lives, as well as in technical applications and fundamental science. We are always in need of knowing the exact time in order to not miss an important event, at other times we are deeply concerned about how many pound we put on weight, and particularly in England, we ought to know how cold or warm it is outside. Likewise, an aeroplane pilot needs to know the altitude, velocity and orientation of the plane at all times in order to conduct a safe journey. More importantly, precise measurements are

crucial to science in order to define standards and prove or disprove scientific theories; the latter is epitomised by the Michelson-Morley interferometric experiment which helped to disprove the long-debated concept of an “ether” in which light was supposed to be propagated.

With the advent of modern technology such as transistors, the laser, and quantum control, the science of measurement has brought incredible achievements that were once thought to be impossible to attain, such as measurements of the variation of Earth’s rotation of one part in 10^5 (Gustavson *et al.*, 2000), atomic clocks with systematic errors below one part in 10^{17} (Rosenband *et al.*, 2008), which in turn allows for the observation of relativistic time dilation at bicycling speeds (Chou *et al.*, 2010).

However, in spite of the current powerful measuring technologies, all of these state-of-the-art devices are limited by the standard quantum limit (SQL) of measurements. The SQL or shot noise limit (SNL) is the best precision scaling for a phase measurement that any device can attain when the measurement process involves N independent or uncorrelated probes that couple to the parameter that needs to be estimated, and it is given by $1/\sqrt{N}$. The way this scaling comes about in strictly classical measuring devices is a consequence of the central-limit theorem: by repeating a large N independent measurements and averaging the outcomes, this average converges to a Gaussian distribution with standard deviation $\Delta\sigma/\sqrt{N}$, thus the precision of the measurement scales as $\sim 1/\sqrt{N}$. This limit to precision with uncorrelated resources is typically exemplified as being the best precision scaling attained by an optical interferometer in which an ordinary laser beam is inputted in only one port, and which measures the path difference between the arms of the interferometer which translates into a measurement of an optical phase ϕ . The phase sensitivity scales as $\Delta\phi \sim 1/\sqrt{\bar{N}}$, where \bar{N} is the mean number of photons that have run through the interferometer. Now, one could think that any desired precision $\Delta\phi$ could be attained by increasing the number of photons \bar{N} , which is obtained by increasing the power of the laser. However, when the laser power becomes too large, power fluctuations introduce additional noise terms that compromise and eventually limit the overall precision of the interferometer (Caves, 1981). Notably, the SQL is not a fundamental one,

and it has been known for more than 30 years that it can be surpassed using “quantum tricks”.

In 1981 Caves (Caves, 1981) showed that when phase-squeezed states are considered as the input to both ports of the interferometer, the phase precision can asymptotically approach $1/\sqrt{N}$, for large numbers of photons N , which is proportional to the optical power of the input states. Later on, Yurke and colleagues (Yurke, 1986; Yurke *et al.*, 1986) showed that using quantum number states which, unlike coherent states, do not experience number fluctuations and hence there is no possibility of squeezing in the conventional sense, it is also possible to surpass the SQL if these number states are highly entangled and used as the input to the interferometer. Since then, a vast amount of theoretical proposals (Cable & Dowling, 2007; Cooper *et al.*, 2010; Dunningham & Hallwood, 2006; Joo *et al.*, 2011; Mitchell *et al.*, 2004a) and experimental (Kacprowicz *et al.*, 2010; Mitchell *et al.*, 2004a; Nagata *et al.*, 2007; Okamoto *et al.*, 2008) demonstrations have been carried out which show the possibility of beating the SQL, particularly by using quantum entanglement as the main resource. The vast majority of the experimental demonstrations have been done with photons; however, the prospect of implementing quantum metrology with matter waves offers several advantages over the optical systems. One of the most important advantages resides in the fact that in order to produce squeezing, the particles need to strongly interact among themselves or through nonlinear terms in the Hamiltonian; however, photons do not interact with other photons and it is technically very difficult and challenging to produce a nonlinear medium capable of producing photon squeezing. On the other hand, atoms interact among themselves all the time almost “for free”, and usually, the interaction strength is highly tunable by either choosing different atom species with different scattering lengths or by using dynamic mechanisms such as Feshbach resonances. Among all the current promising atomic systems for matter wave metrology, Bose–Einstein condensates are the perfect candidates for superseding incoherent atomic systems for the use of quantum metrology, just as optical lasers superseded thermal light sources in high precision metrology. In the following section we touch upon the topic of Bose–Einstein condensates and their relevance to quantum metrology. For a very good review on the topic of

matter wave interferometers as prospects for precision measurements, we refer the reader to Refs. ([Cronin *et al.*, 2009](#); [Robins *et al.*, 2013](#)).

1.2 Bose–Einstein condensation

The description of Bose–Einstein condensation traces its origin back to 1924, when Satyendra Nath Bose ([Bose, 1924](#)) published a paper where he derived Planck’s law using non-classical arguments for photons which now forms the basis of the statistical description of identical quantum particles with integer spin. Einstein translated Bose’s paper to German and had it published on his behalf. Later on, Einstein adapted Bose’s work and extended the theory for massive particles ([Einstein, 1925](#)). This led to the prediction of the Bose–Einstein condensation phenomenon, a collection of bosonic particles can be forced to have a macroscopic occupancy of the lowest single-particle energy level below a certain finite critical temperature by purely statistical effects. Although creating a Bose–Einstein condensate (BEC) is quite simple in principle, i.e., cool down a bosonic gas to extreme low temperatures until the wavefunctions of the particles start to overlap, overcoming the actual technical problems proved to be extremely difficult. Even as late as 1994, Steve Chu, one of the pioneers of laser cooling, stated in a news article: “I am betting on Nature to hide Bose condensation from us. The last 15 years she’s been doing a great job” ([Ketterle, 2002](#)). But, in 1995, in a series of ground-breaking experiments, Bose–Einstein condensation was finally achieved by different groups in dilute gases of rubidium ([Anderson *et al.*, 1995](#)), lithium ([Bradley *et al.*, 1995](#)), and sodium ([Davis *et al.*, 1995](#)).

In order to obtain a Bose–Einstein condensate, the atomic cloud needs to be cooled down to extremely low temperatures. This can be achieved by a sequential use of laser cooling followed by evaporative cooling ([Pethick & Smith, 2008](#)). In laser cooling, two counter-propagating lasers which are red-detuned with respect to an atomic resonance, fire photons upon the atoms which are more likely to absorb photons that oppose their motion, due to the Doppler effect. The absorption of a photon leaves the atom in an excited state and causes a momentum transfer to the atom, which makes it recoil in the opposite direction to its motion. When the photon is re-emitted in a random direction by spontaneous emission,

the momentum exchange from this fluorescent radiation averages zero, so the net total effect is that of damping the motion of the atoms and slowing them down in the direction of the propagating lasers, similar to the motion of a marble inside a viscous medium; in fact, this cooling scheme has been dubbed “optical molasses”. In order to slow down the atoms in all directions, three orthogonal pairs of counter-propagating lasers are used, so that no matter what direction an atom moves in this optical molasses, it always feels a force opposing its motion. As the atoms slow down, they are no longer in resonance with the lasers and consequently the cooling mechanism stops working. Further cooling by this method can be achieved by tuning the atomic frequency with magnetic fields. However, there is a limit to how cold the atoms can be cooled down using laser cooling because the absorption of photons not only gives rise to an opposing force but it also heats the atoms. An atom at rest is equally likely to absorb a photon from either direction of the counter-propagating lasers, and since the absorption events are random and uncorrelated, the atom undergoes a random walk in momentum space, which effectively causes heating of the cloud. This laser cooling method can bring the atomic cloud to extremely low temperatures of the order of $\sim 200 \mu\text{K}$, which is still “too hot” to achieve Bose–Einstein condensation by a factor of 10^3 .

The required low temperatures for observing Bose–Einstein condensation can be obtained by applying evaporative cooling after having laser cooled down the atomic cloud. After the laser cooling process, the atoms are transferred to a magnetic-optical trap (MOT) which uses 3 pairs of circularly polarised lasers and a non-homogeneous magnetic field in order to tune atomic transitions via the Zeeman effect, in such a way so that laser radiation will always be absorbed in a manner that generates a force which keeps the atoms inside the trap. Evaporative cooling is then achieved by effectively causing a “hole” in the upper part of the potential allowing high energetic atoms corresponding to energies equal to the energy level of the trap at the position of the “hole”, to escape the confinement, thereby removing the high-energetic part of their thermal distribution. As a result, the rest of the atoms in the trap rethermalise to a lower temperature than the one they started with. In practice, this “hole” in the trap is realised using radio-frequency radiation that targets high-energetic atoms in order to flip their

1.2 Bose–Einstein condensation

spin state from a low-field seeking one to a high-field seeking one, causing these atoms to be expelled from the trap. The fact that the spatial spreading of an atom’s wave function depends on its energy in the trap, and that the atomic resonance acquires a larger Zeeman shift as the atom is farther away from the centre of the trap, allows one to tune the radio-frequency radiation in order to select the position of the “hole” in the trap. As energetic atoms are lost and the rest of the gas thermalises, the radio-frequency radiation is slowly adjusted to allow loss of atoms with lower and lower energy, until the necessary temperatures for Bose–Einstein condensation are achieved, which are of the order of \sim nK.

As the atomic cloud is cooled down, it approaches a critical temperature which corresponds to the onset of Bose–Einstein condensation. For an atomic gas trapped in a harmonic trap, the critical temperature is given by

$$k_{\text{B}}T_c \approx 0.94\hbar\omega_0 N^{1/3}, \quad (1.2)$$

where k_{B} is Boltzmann’s constant, ω_0 the harmonic trap frequency and N is the number of atoms. Therefore, the critical temperature can be raised by increasing the density of atoms in the trap. Unfortunately, if the density exceeds a certain critical value, the interactions become so strong that the simple theory of BEC fails. This diluteness condition is expressed as $a/r \ll 1$, where a is the scattering length and r is the mean interparticle separation. In one of the first experiments at JILA ([Anderson *et al.*, 1995](#)), the average harmonic level separation was about 9 nK, the number of atoms was roughly 40 000, and thus the critical temperature was about 300 nK. Below the critical temperature, there is a finite macroscopic fraction of the atoms occupying the lowest single-particle level, this fraction is given in a harmonic trap by ([Pethick & Smith, 2008](#))

$$\frac{N_0}{N} = 1 - \left(\frac{T}{T_c}\right)^3, \quad (1.3)$$

where N_0 is the fraction of atoms in the ground state. Imaging of the condensate after the trapping potential is switched off and the gas undergoes ballistic expansion, shows a sharp peak in the velocity distribution which is a clear signature that a macroscopic fraction of the atoms were occupying the same single-particle state, i.e. Bose–Einstein condensation.

So far, we have discussed the phenomenon of Bose–Einstein condensation without considering the interactions between the particles, which is not completely realistic. Nevertheless, Bogoliubov showed in 1947 (Bogoliubov, 1947) that the presence of interactions in very dilute and weakly interacting gases does not considerably alter the description of the BEC as an ideal quantum gas. The fact that particle separations in cold atomic gases are typically of the order 10^2 nm, which are usually an order of magnitude larger than the scattering length for atom-atom interactions, makes it possible to neglect three- and higher-body interactions, and only two-body ones primarily determine the behavior of cold interacting quantum gases. Moreover, since the atoms move at very low speeds in ultracold gases, and the interatomic van der Waals interaction is proportional to $1/r^6$, where r is the interatomic distance, it can be shown that only s-wave scattering contributes to the determination of the scattering cross section. Thus, in the limit of very low speeds, the total cross section σ is determined only by the scattering length a , and it is given by $\sigma = 4\pi a^2$ (Pethick & Smith, 2008). As it turns out, for ultra-cold dilute gases, the many-body description of the system depends only on this one parameter, the scattering length a , and not on the details of the interatomic potential (Dalibard, 1999). As a result, the interactions between the atoms can be modeled using an effective interaction potential which leads to the same scattering length as that obtained by using the bare potential. In principle, the simplest effective interaction between two particles is the contact interaction given by

$$V(\vec{\mathbf{x}}_1 - \vec{\mathbf{x}}_2) = \frac{4\pi\hbar^2 a}{M} \delta(\vec{\mathbf{x}}_1 - \vec{\mathbf{x}}_2), \quad (1.4)$$

where M is the mass of the atom. This potential is at the basis of the many-body approach to ultra-cold quantum gases, and will be used as our model of interactions when we introduce the system studied in this thesis.

Although the inclusion of weak interactions does not considerably alter the description of BECs, they play a major role in the exact behavior of the condensate; they can lead, for instance, to different quantum phases and impose dynamical restrictions. For example, an homogeneous BEC with attractive interactions is unstable beyond a certain critical number of atoms, whereas a condensate with repulsive interactions is stable. Likewise, it can be shown that for a BEC with

attractive interactions in a rotating harmonic trap, the angular momentum is absorbed by the centre of mass for slow rotations, whereas in a condensate with repulsive interactions, this rotation would lead to the formation of quantised vortices (Wilkin *et al.*, 1998).

Therefore, being able to manipulate the strength of the interactions between the atoms opens the possibility of engineering different systems with particular properties. Remarkably, the magnitude and sign of the interactions can be widely tuned by means of Feshbach resonances (Cornish *et al.*, 2000). When two atoms in internal states labeled by α and β collide with relative momentum $\hbar\vec{k}$, which is referred as the entrance channel $\hbar\vec{k}_{\alpha\beta}$, the product is a scattered wave that has components in different internal states $\alpha'\beta'$ corresponding to a so-called exit channel $\hbar\vec{k}'_{\alpha'\beta'}$. Due to the fact that hyperfine and Zeeman energies are generally different for the entrance and exit channels, the magnitude of their corresponding relative momentum is different too, and hence they are related by the condition that the total energy be conserved

$$\frac{\hbar^2 k'^2_{\alpha'\beta'}}{2M_r} = \frac{\hbar^2 k^2_{\alpha\beta}}{2M_r} + \epsilon_\alpha + \epsilon_\beta - \epsilon_{\alpha'} - \epsilon_{\beta'}, \quad (1.5)$$

where M_r is the reduced mass of the two atoms and ϵ_α represent the energy associated with the internal state α , and similarly for any other internal state. If $k'^2_{\alpha'\beta'} \leq 0$, the channel is said to be closed, there is not enough energy in the entrance channel to produce two stationary atoms in the internal states α' and β' corresponding to the exit channel (Pethick & Smith, 2008). Although the scattering of two atoms cannot produce a final state corresponding to a closed channel, it can highly influence the scattering amplitude of open ones, and this forms the basis of Feshbach resonances, which were introduced in the context of ultra-cold atoms in (Stwalley, 1976). Feshbach resonances occur when the total energy in an open channel matches that of a bound state in a closed channel. Although there is no first order coupling between an open and closed channel, two particles in an open channel can scatter to an intermediate state corresponding to the closed channel, after which the particles decay to an open exit channel state. This second-order process has the effect of changing the effective scattering length of the overall process. Therefore, by exploiting the fact that energies of

internal states depend on external parameters, such as the magnetic field, atomic interactions can be tuned by means of Feshbach resonances. In fact, for internal states whose energies can be shifted using a magnetic field, the effective scattering length can be shown to be

$$a = a_{\text{nr}} \left(1 - \frac{\Delta B}{B - B_0} \right), \quad (1.6)$$

where a_{nr} is the non-resonant scattering length when coupling between open and closed channels is neglected, ΔB is a rather complicated expression containing the magnetic moments of the open and closed channel and a term corresponding to the matrix element coupling open and closed channels, and B_0 is the magnitude of the magnetic field that produces a Feshbach resonance for the given open and closed channels. This shows that by varying the magnitude of the magnetic field B , the effective scattering length can be changed in magnitude and also its sign. As it turns out, experimentally, this tuning of the interactions can be made for a wide range of values of the scattering length (Cornish *et al.*, 2000).

The high tunability of interactions in BECs via Feshbach resonances allows for the manipulation of the non-linear aspect of interacting matter that can lead to squeezing and entanglement production in condensates; this feature makes BECs very well suited for metrology schemes. Another important feature that makes BEC a promising system for quantum metrology is its remarkable coherence. First-order coherence in BECs was experimentally demonstrated for the first time by Andrews *et al.* (Andrews *et al.*, 1997), where they split a BEC into two spatially separated condensates using a double-well potential, which was subsequently switched off, resulting in two freely expanding condensates which overlapped in space, creating an interference pattern with high visibility fringes, which was a clear sign of first-order coherence. Later on that same year, the group of Cornell (Burt *et al.*, 1997) experimentally demonstrated the existence of higher-order coherence in a BEC by measuring the three-body recombination rate, which was predicted to be 6 times slower than that for a non-condensed atomic cloud having the same density; therefore, it is said that the condensate shows signs of anti-bunching of atoms, which is a common feature in coherent laser light. These two experiments support the conclusion that a BEC ground

state is analogous to a number-squeezed coherent state like the ones produced with photons using lasers (Dowling, 1998), which prompted the use of the term “atom laser”. Since then, many theoretical proposals to use BEC in interferometric schemes have been put forward, some of them have been successfully realised in the laboratory. Although a breakthrough experiment in 2010 demonstrated the first atom interferometer with sensitivity greater than the classical limit (Gross *et al.*, 2010), real world applications with sub-shot noise interferometry are still far from reaching the retail stores, and the pursuit of more robust atom interferometers with sub-shot noise precision has become a research area which is quickly growing because the technological impact that it represents is very high.

One particular research avenue in atomic interferometry with BECs that concerns this thesis is that of rotating Bose–Einstein condensates. This configuration can take advantage of all the mentioned properties of BECs such as coherence and non-linearity provided by interactions, in order to create entangled states which can be used in interferometric protocols to measure rotation rates with sub-shot noise precision. One of the main results of this thesis is a proposal for such an interferometric protocol; we will expand on the topic of rotating BECs and its potential use in quantum metrology in the next chapter.

1.3 Thesis overview

We start with chapter 2, where preliminary concepts and tools in quantum metrology are presented. This material provides a broad context in which the work carried out in the rest of the thesis is embedded. In the following chapter 3, we introduce the physical system used throughout the thesis, that is, a rotating BEC in a stirred anisotropic trap; we solve the basic equations of motion and introduce the lowest Landau level (LLL) approximation which is central to this thesis. It is shown that within the LLL, the system undergoes a quantum phase transition for a certain critical rotation frequency, which implies correlations and entanglement in the ground state. Additionally, we review the general results for rotating BEC in an isotropic trap and provide numerical results concerning the Fisher information of the ground state, which bounds the accuracy of phase measurements in metrology schemes. Then, in chapter 4, we study the system

beyond the LLL approximation, showing that it fails to predict the exact form of the entangled state and its Fisher information in regimes where the LLL was thought to be valid. Incidentally, this shows that the system can be used to generate different quantum states which possess different entanglement characteristics, making it a very versatile system for producing entangled input states for quantum metrology. Finally, in chapter 5, we describe a theoretical proposal for an interferometric scheme using the rotating BEC, and show that the interferometer has the potential of delivering nearly Heisenberg-limited precision in measurements of rotation frequencies for a range of different entangled states. We argue that the proposal is amenable to experimental research and a proof-of-principle experiment should be within reach of current technologies.

Chapter 2

Preliminaries

In this chapter, we review the relevant background material for this thesis. We start by introducing the Mach–Zehnder interferometer, which is one of the most common schemes for metrology in many areas of science, and particularly in quantum metrology. We describe in detail all the elements that make up the interferometer, and obtain a general expression for the precision of a phase measurement for any given input state. Using this expression, we find the phase precision for different well-known input states used in quantum metrology, establishing that the classical limit can be overcome using entangled states. After this exercise, the important tool of quantum Fisher information is derived. The Fisher information plays a central role in this thesis since it allows us to establish the ultimate attainable precision for our schemes. Finally, we slightly switch gears and give a brief review of rotating Bose–Einstein condensates, in anticipation of the more detailed treatment of rotating condensates in a stirred anisotropic trap in chapter 3.

2.1 Mach–Zehnder interferometer

Although there exist many types of interferometers, such as the Fabry–Pérot interferometer, the Michelson interferometer or the Sagnac one, the Mach–Zehnder interferometer is one of the most widely used two-path interferometers in many areas of Physics. Particularly, it is conveniently well suited for investigating quantum entanglement and quantum enhancement of phase measurements. In a

2.1 Mach–Zehnder interferometer

way, it can be thought as being the most simple type of interferometer (besides a two-slit experiment) which captures all the main aspects and subtleties of interference as a mean of measuring unknown physical quantities. Hereinafter, we focus on the Mach–Zehnder interferometer in the context of quantum mechanics, where the interferometer represents a series of unitary operations that transform a quantum input state into a modified output state.

The prototypical two-path Mach–Zehnder interferometer is shown in Fig. (2.1). It consists of two input ports labeled A and B , corresponding to two different quantum modes, which are usually fed with a separable state $|\alpha\rangle|\beta\rangle$ representing an incoming flux of particles, where the first ket corresponds to port A and the second one to port B . These two modes are split into two arms inside the interferometer by using a first beam splitter (BS1). Afterward, the upper arm picks up an unknown phase ϕ which represents a path difference between the two arms. Then, the two streams of particles are reflected off the mirrors and recombined at a second beam splitter (BS2). Finally, the particles emerge from either the upper output port C or lower one D , after which they hit the detectors at the end of the interferometer. Measuring the particles at the output ports in principle allows the determination of the unknown phase.

As it was mentioned before, every element in the interferometer corresponds to a unitary transformation acting on two or one single mode. The unitary operator representing each element can be obtained from an appropriate Hamiltonian in the following way

$$U_H = e^{-iH\Delta t/\hbar}. \quad (2.1)$$

Using this unitary operator, we can express its action on products of Fock states through transformations in the creation and annihilation operators as follows

$$U|n\rangle|m\rangle = \frac{(U\hat{a}^\dagger U^\dagger)^n}{\sqrt{n!}} \frac{(U\hat{b}^\dagger U^\dagger)^m}{\sqrt{m!}} |0\rangle|0\rangle, \quad (2.2)$$

where \hat{a}^\dagger and \hat{b}^\dagger are the creation operators for the two input modes, $U\hat{a}^\dagger U^\dagger$ and $U\hat{b}^\dagger U^\dagger$ are the corresponding creation operators for the output modes of the device represented by the unitary U .

2.1 Mach–Zehnder interferometer

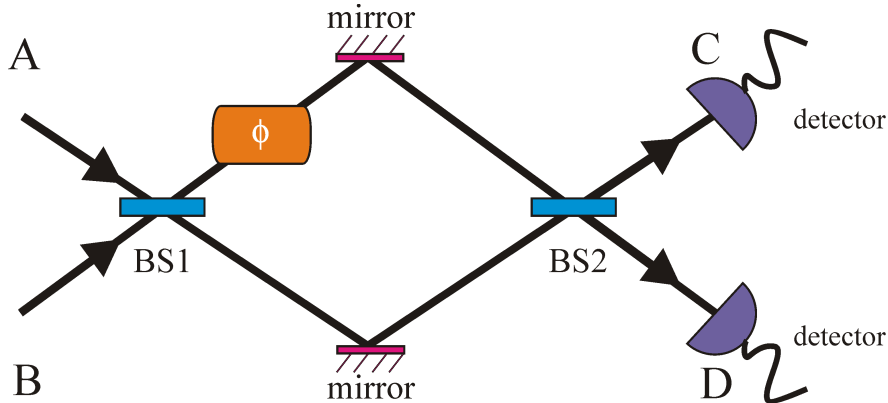


Figure 2.1: A two-mode Mach–Zehnder interferometer setup. Two incident streams of particles at input ports A and B are split into two modes corresponding to the upper and lower arm of the interferometer by a beam splitter (BS1). An unknown phase ϕ is picked up by the upper arm and the two modes are recombined using another beam splitter (BS2). As a final step, the particles are detected at the output ports C and D .

Let us review the unitary transformations for each element in the interferometer. The beam splitter, which in optical systems usually consists of a semi-reflective mirror that when light passes through it, part will be reflected and part will be transmitted. For atoms, this may correspond to a double-well potential which creates two spatially separated groups of particles corresponding to the two output ports of the beam splitter. In any case, the general beam splitter is defined by the transformations

$$U\hat{a}^\dagger U^\dagger = \cos\theta a_{\text{in}}^\dagger + ie^{-i\phi} \sin\theta b_{\text{in}}^\dagger, \quad (2.3)$$

$$U\hat{b}^\dagger U^\dagger = ie^{i\phi} \sin\theta a_{\text{in}}^\dagger + \cos\theta b_{\text{in}}^\dagger, \quad (2.4)$$

with the interaction Hamiltonian,

$$H = \hbar\theta \left(e^{i\phi} \hat{a}^\dagger \hat{b} + e^{-i\phi} \hat{a} \hat{b}^\dagger \right). \quad (2.5)$$

The physical beam splitter can be described by any choice of θ and ϕ , where θ is a measure of the transmissivity, and ϕ gives the phase shift due to the coating of the mirror in optical systems. An additional phase shift may be necessary to

2.2 Precision scaling for well-known input states

describe the workings of the physical object correctly. Here, we use 50-50 beam splitters with $\theta = \pi/4$ and $\phi = 0$.

The transformations for the mirrors are simpler. They correspond to a beam splitter with a transmissivity of $\theta = \pi/2$ and a phase shift of $\phi = 0$. Therefore, the transformations are given by

$$U\hat{a}^\dagger U^\dagger = ib_{\text{in}}^\dagger, \quad (2.6)$$

$$U\hat{b}^\dagger U^\dagger = ia_{\text{in}}^\dagger. \quad (2.7)$$

Finally, the phase shift acts only on one mode, which gives rise to an overall phase factor that depends on the number of particles in the given mode. The transformation in this case is

$$\hat{a}^\dagger = e^{i\phi}\hat{a}^\dagger, \quad (2.8)$$

with the interaction Hamiltonian $H_\phi = \phi\hbar a_{\text{in}}^\dagger a_{\text{in}}$. This means, for example, that $U|n\rangle|m\rangle = e^{in\phi}|n\rangle|m\rangle$ for a phase shift in the first mode. In optical systems a phase shift can be implemented using a transparent element with an index of refraction that is different from free space, or an optical fibre. In atomic systems, this phase is usually associated with a free evolution of a quantum state in a superposition of two eigenstates of the full many-body Hamiltonian, typically the ground state and the first excited state, where the phase factor is given by $\exp(-i\Delta E\tau/\hbar)$, ΔE is the energy gap between these two eigenstates, and τ is the waiting time during the free evolution.

2.2 Precision scaling for well-known input states

In what follows, we study the precision with which a measurement of an unknown phase can be achieved using a Mach–Zehnder interferometer, for a range of prominent input states widely considered in metrology schemes. We closely follow the derivations in (Dowling, 1998) for the study of the coherent and the Yurke state, and apply the same machinery for other input states.

Let \hat{a}^\dagger and \hat{b}^\dagger be the creation operators for the input ports A and B , respectively, and \hat{a} and \hat{b} the corresponding annihilation operators. Likewise, let \hat{c}^\dagger and

2.2 Precision scaling for well-known input states

\hat{d}^\dagger be the creation operators for the output ports C and D , respectively. Furthermore, assume without loss of generality that we are dealing with bosons and thus these operators satisfy the usual commutation relations, such as $[\hat{a}, \hat{a}^\dagger] = 1$ and similarly for the other operators.

Using the unitary transformations that we described above for each element in the interferometer, it can be shown that the input annihilation operators are related to the output ones through a scattering matrix-like relationship given by

$$\begin{bmatrix} \hat{c} \\ \hat{d} \end{bmatrix} = \begin{bmatrix} \sin(\phi/2) & \cos(\phi/2) \\ \cos(\phi/2) & -\sin(\phi/2) \end{bmatrix} \begin{bmatrix} \hat{a} \\ \hat{b} \end{bmatrix}, \quad (2.9)$$

where a similar expression for the creation operators is obtained by taking the hermitian conjugate of this matrix equation. For an interferometric set-up like the Mach-Zehnder interferometer, the phase ϕ is to be estimated from the specific distribution of particle counts at the detectors. In order to do this, we define the output-port sum and difference operators \hat{N} and \hat{M} as

$$\hat{N} = \hat{d}^\dagger \hat{d} + \hat{c}^\dagger \hat{c}, \quad (2.10)$$

$$\hat{M} = \hat{d}^\dagger \hat{d} - \hat{c}^\dagger \hat{c}. \quad (2.11)$$

Then, carrying out the matrix multiplication in Eq.(2.9), these two operators can be expressed in terms of the input-port creation and annihilation operators as

$$\hat{N} = \hat{a}^\dagger \hat{a} + \hat{b}^\dagger \hat{b}, \quad (2.12)$$

$$\hat{M} = (\hat{a}^\dagger \hat{a} - \hat{b}^\dagger \hat{b}) \cos \phi - (\hat{a}^\dagger \hat{b} + \hat{b}^\dagger \hat{a}) \sin \phi. \quad (2.13)$$

The first of these expressions is nothing but the statement of particle conservation. The second one contains information about the unknown phase, and thus a measurement of $\langle \hat{M} \rangle$ at the output ports can be used to estimate ϕ . The precision for a repeated measurement of any quantity, such as the phase ϕ , is a measure of how spread out the distribution around the mean measured value is, and it is usually characterised by the second moment of the distribution, the variance $\Delta\phi^2$; although normally, the standard deviation $\Delta\phi$ is the preferred choice for expressing the precision. Therefore, the phase precision resulting from measuring the mean value of the difference number operator and its variance, can be found

2.2 Precision scaling for well-known input states

in terms of these measurements by a simple manipulation of the errors (Dowling, 1998; Dunningham, 2006)

$$\Delta\phi^2 = \frac{\Delta M^2}{|\partial\langle\hat{M}\rangle/\partial\phi|^2}, \quad (2.14)$$

where $\Delta M^2 = \langle\hat{M}^2\rangle - \langle\hat{M}\rangle^2$ is the usual variance for operators.

From here, Dowling expands this last expression in terms of operators \hat{X} and \hat{Y} which are defined in terms of the input-port creation and annihilation operators as

$$\hat{X} = \hat{a}^\dagger\hat{a} - \hat{b}^\dagger\hat{b}, \quad (2.15)$$

$$\hat{Y} = \hat{a}^\dagger\hat{b} + \hat{b}^\dagger\hat{a}, \quad (2.16)$$

resulting in the expression

$$\Delta\phi^2 = \frac{\Delta X^2 \cos^2 \phi - \left(\langle\hat{X}\hat{Y}\rangle - 2\langle\hat{X}\rangle\langle\hat{Y}\rangle + \langle\hat{Y}\hat{X}\rangle\right) \sin \phi \cos \phi + \Delta Y^2 \sin^2 \phi}{\left|\langle\hat{X}\rangle \sin \phi + \langle\hat{Y}\rangle \cos \phi\right|^2}. \quad (2.17)$$

Despite its seemingly contrived form, this equation is very convenient for calculating the precision of the phase measurement in terms of expectation values of the operators \hat{X} and \hat{Y} , and their combinations. The expectation values are computed with respect to the input state, since these operators only involve creation and annihilation operators at the input ports.

We now proceed to use Eq.(2.17) to calculate the expected precision in the phase measurement using different well-known input states studied in the literature.

2.2.1 Uncorrelated and classical states

The most simple case to calculate is the one corresponding to the case of N uncorrelated particles entering only one of the input ports. This case corresponds to the input state

$$|\psi\rangle_{\text{in}} = |N\rangle|0\rangle, \quad (2.18)$$

2.2 Precision scaling for well-known input states

which can be thought as feeding the interferometer with N particles, one at a time in only the upper input port. The necessary expectation values are straightforward to calculate for this case, and they are given by (Dowling, 1998)

$$\langle \hat{X} \rangle = N, \quad \langle \hat{Y} \rangle = 0, \quad (2.19)$$

$$\langle \hat{X}^2 \rangle = N^2, \quad \langle \hat{Y}^2 \rangle = N, \quad (2.20)$$

$$\langle \hat{X}\hat{Y} \rangle = \langle \hat{Y}\hat{X} \rangle = 0. \quad (2.21)$$

Inserting these expression into Eq.(2.17), we obtain the precision for this input state with independent particles

$$\Delta\phi_{\text{indep}} = \frac{1}{\sqrt{N}}. \quad (2.22)$$

This is the shot-noise limit, and in this case, it is almost a pure consequence of the central-limit theorem for classical random measurements of samples taken from an unknown distribution. This statistical noise is the main limitation in high-precision measurements

In conventional interferometry, however, one uses a laser as an input to one of the ports instead of a Fock state, and vacuum in the other port. The output state of a single-frequency laser well above threshold can be very well approximated by a coherent state $|\alpha\rangle$ (Glauber, 1963)

$$|\alpha\rangle = e^{-|\alpha|^2/2} \sum_n \frac{\alpha^n}{\sqrt{n!}} |n\rangle, \quad (2.23)$$

where α is a complex parameter which determines the average photon number $\bar{N} = |\alpha|^2$, and the phase of the coherent state.

In some respects, the coherent state closely resembles a classical state of light. For instance, if the electric field corresponding to a coherent state is measured with homodyne detection, the oscillations have a clear distinctive amplitude and frequency, as in a classical single-frequency electromagnetic wave, apart from some superimposed quantum noise. Also, in the context of the harmonic oscillator, a coherent state behaves as a wave packet that bounces back and forth without spreading in shape, and satisfies the minimum uncertainty product relation at all times (Sakurai, 1967).

2.2 Precision scaling for well-known input states

Let us now calculate the phase precision for the input state

$$|\psi\rangle_{\text{in}} = |\alpha\rangle|0\rangle, \quad (2.24)$$

representing the typical input in conventional interferometry. Again, finding the expectation values for \hat{X} , \hat{Y} , and their combinations, we arrive at the result

$$\Delta\phi_{\text{coherent}} = \frac{1}{\sqrt{N}|\sin\phi|}. \quad (2.25)$$

This precision exhibits the same scaling with the number of particles as the one obtained for Fock states, i.e. shot-noise scaling, reinforcing the idea of the coherent state resembling a classical state; however, the precision is not independent of the phase and it becomes progressively worse by a constant factor as we try to measure phase shifts close to 0. The measurement is optimal for a phase shift of $\pi/2$, so in principle, if the unknown phase ϕ produces a very low-precision measurement, meaning that its value is close to zero, we could add a deliberate phase shift of $\pi/2$ in order to “push” the overall phase shift toward the optimal regime for this setup and achieve precision of the order $\sim 1/\sqrt{N}$.

2.2.2 Yurke state

Let us set $\phi = 0$ in Eq.(2.17) for now, in order to gain some insight as to how the phase precision could be improved. There is no loss of generality because, again, we can always add a deliberate phase shift that produces an overall phase shift (unknown shift plus deliberate one) of zero. This is usually easy to realise using a feedback mechanism that adjusts the deliberate phase shift by checking a null in the interference pattern, which indicates in turn a null overall phase shift (Dowling, 1998).

For $\phi = 0$, the phase precision is

$$\Delta\phi^2|_{\phi=0} = \frac{\Delta X^2}{|\langle\hat{Y}\rangle|^2}. \quad (2.26)$$

Therefore, we see that the phase precision can be made smaller by finding an input state which has a small variance in \hat{X} , and a corresponding larger mean value of \hat{Y} . Since \hat{X} is the number difference between the two input ports, it is

2.2 Precision scaling for well-known input states

natural to look for states that have approximately equal numbers of particles in both modes. In 1986, Yurke suggested such a state (Yurke, 1986; Yurke *et al.*, 1986), which is given by

$$|\psi\rangle_{\text{in}} = \frac{1}{2} \left(\left| \frac{N+1}{2} \right\rangle \left| \frac{N-1}{2} \right\rangle + \left| \frac{N-1}{2} \right\rangle \left| \frac{N+1}{2} \right\rangle \right), \quad (2.27)$$

where the total number of particles N is assumed to be odd. Then, it can be shown that the phase precision is

$$\Delta\phi^2|_{\phi=0} = \frac{2}{N+1}, \quad (2.28)$$

which scales as $\sim 1/N$, overcoming the shot-noise limit. This type of scaling is known as Heisenberg-limited precision and the conventional wisdom nowadays seems to be that this is the best precision scaling we can achieve for phase measurements (Giovannetti & Maccone, 2012).

For photons, one way to realise the Yurke state is using four-wave mixers (Yurke *et al.*, 1986), whereas for atoms, it could be obtained using a dual condensate in a double well (Spekkens & Sipe, 1999).

The Yurke state is a highly correlated quantum state, and these results suggest that the sub-shot noise limit can be overcome by using similar entangled states as the input to the interferometer. Therefore, it is natural to consider the case of maximally entangled states such as the $N00N$ one for quantum interferometry. We now proceed to study this highly entangled state.

2.2.3 $N00N$ state

In our current context, The $N00N$ state or “cat state” is a macroscopic superposition of all the particles being in one of the modes (corresponding to one path of the interferometer) and all on the other mode. Bollinger *et al* first put forward the idea of using these entangled states to measure frequencies of atomic transitions with high precision (Bollinger *et al.*, 1996).

A $N00N$ state is represented by

$$|N00N\rangle = \frac{1}{\sqrt{2}} (|N, 0\rangle + |0, N\rangle). \quad (2.29)$$

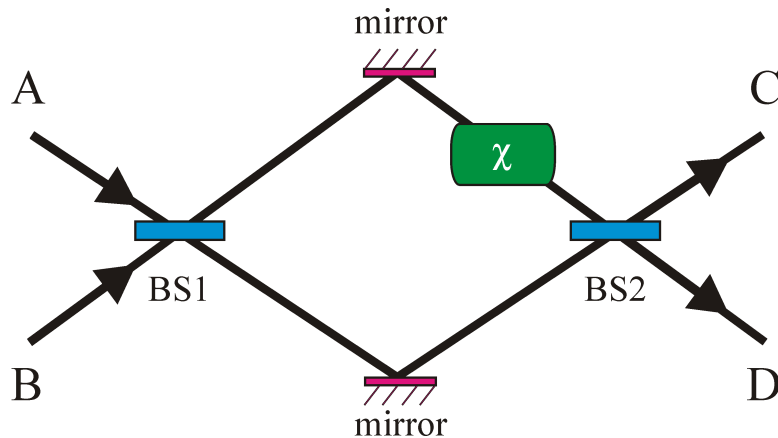


Figure 2.2: A quantum beam splitter (QBS). Two incident streams of particles at input ports A and B are split into two modes corresponding to the upper and lower arms by a beam splitter (BS1). A non-linear phase characterised by χ is applied in the upper arm. The resulting non-linear phase depends quadratically with the number of particles in that mode. Finally, the two modes are recombined using another beam splitter (BS2).

In this section, we closely follow the work in (Dunningham & Kim, 2006), where they demonstrate how to create a $N00N$ state similar to Eq.(2.29) from a Fock state, and also show that a quantum interferometer can be realised which uses the $N00N$ state to attain Heisenberg-limited precision in phase measurements.

The quantum interferometer is just like the normal Mach–Zehnder interferometer in Fig. (2.1), except that the beam splitters are replaced by quantum beam splitters. A quantum beam splitter (QBS) is in itself another Mach–Zehnder interferometer which has been modified by replacing the phase shift with a non-linear element χ as shown in Fig. (2.2). The effect of the non-linear element is that of applying a phase shift that depends quadratically on one of the modes. The unitary operator corresponding to this non-linear element has the form $\exp(-i\chi(\hat{a}^\dagger\hat{a}))$.

If the QBS is inputted with a separable Fock state $|N, 0\rangle$, the outcome state at the output ports can be shown to be

$$|N, 0\rangle \rightarrow \frac{1}{\sqrt{2}} (|N, 0\rangle + i^{N-1}|0, N\rangle), \quad (2.30)$$

up to a global phase. This is a $N00N$ state with a relative phase between the

2.2 Precision scaling for well-known input states

two macroscopic states, which does not change its qualitative behaviour in interferometric schemes.

Then, it can be shown that, when the Fock state $|N, 0\rangle$ is used as the input to the interferometer in Fig. (2.1) with the beam splitters replaced by quantum beam splitter, the output state is (Dunningham & Kim, 2006)

$$|\psi\rangle_{\text{out}} = \frac{i}{2} [(-1)^N (e^{iN\phi} - 1) |N, 0\rangle + i^{N-1} (e^{iN\phi} + 1) |0, N\rangle]. \quad (2.31)$$

The first thing to notice about this output state is the fact that all particles will be detected at one mode or all the particles at the other. This implies that, for this particular interferometric set-up, the scheme will be robust against imperfect detectors. This can actually be proven in a more rigorous way using the model of nonideal photodetection. However, if particle losses are considered within the interferometer, the precision in the measurement of the phase ϕ degrades very rapidly with the particle loss rate, as we shall see in the next section.

This time, we cannot use Eq.(2.17) because this expression is dependent on the actual details of the interferometer. However, it is straightforward to verify that in this case $\langle \hat{M} \rangle = N \cos N\phi$ and $\Delta M^2 = (N \sin N\phi)^2$. Thus, the phase resolution can be obtained again with the manipulation of errors as

$$\Delta\phi^2 = \frac{\Delta M^2}{|\partial\langle \hat{M} \rangle/\partial\phi|^2} = \frac{1}{N^2}. \quad (2.32)$$

This shows that the use of $N00N$ states can attain the exact Heisenberg limit for the phase resolution. Unfortunately, one of the main disadvantages of $N00N$ states is its formidable fragility, and it is the very same reason why we do not observe such superpositions in our everyday lives. From the double-slit experiment we know that when the particles are monitored in order to determine which slit they went through, the interference pattern is destroyed. In the same way, if a particle is lost from a $N00N$ state, it can leave “forensic” evidence in the environment about what state it was in. For the case of a $N00N$ state, knowing what the state is for any of the particles, betrays the state of the rest of them, destroying the entanglement. Decoherence due to environmental coupling has been the major obstacle in creating these entangled states; nevertheless, $N00N$ states

2.2 Precision scaling for well-known input states

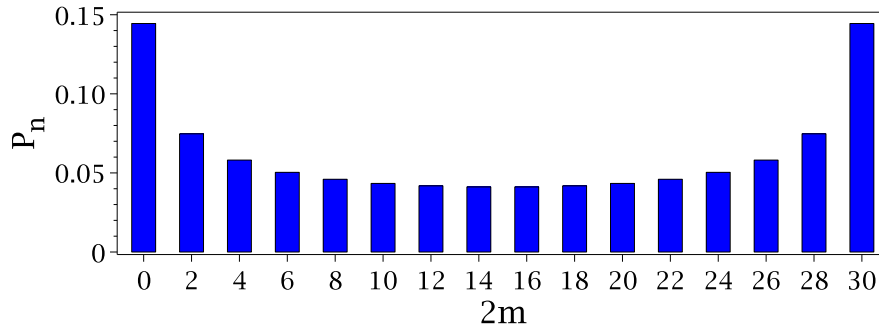


Figure 2.3: Probability distribution for a number of atoms $2m$ in the upper arm ($N - 2m$ at the lower arm) at the output of a 50:50 beam splitter, when the input is a twin Fock state with 30 particles. The output state corresponds to the bat state.

with small numbers of atoms have been produced in experiments, such as states with three photons (Mitchell *et al.*, 2004b) or four ions (Sackett *et al.*, 2000).

In realistic scenarios with particle losses, an entangled input state that is robust against decoherence, capable of attaining sub-shot noise precision is preferred over a $N00N$ state. In the following section we introduce the so-called “bat state” which has exactly those properties.

2.2.4 Bat state

A “bat state” is produced when a twin Fock state $|\frac{N}{2}, \frac{N}{2}\rangle$ is passed through a regular beam splitter, where N is the total number of particles, an even number. The resulting state after the beam splitter operation is (Dunningham, 2006)

$$|\psi\rangle_{\text{bat}} = \frac{1}{2^{N/2}} \sum_{m=0}^{N/2} \frac{[(2m)!(N-2m)!]^{1/2}}{m!(N/2-m)!} |2m\rangle |N-2m\rangle. \quad (2.33)$$

A plot of the probabilities corresponding to the square value of the coefficients is shown in Fig. (2.3). The probability plot resembles the ears of a bat, hence the name bat state. Since the creation of a bat state does not require quantum beam splitters, a normal Mach–Zehnder interferometer is used for producing the bat state and measuring the unknown phase. This means we can use Eq.(2.17) to calculate the precision of the phase measurement for the state in Eq.(2.33).

2.2 Precision scaling for well-known input states

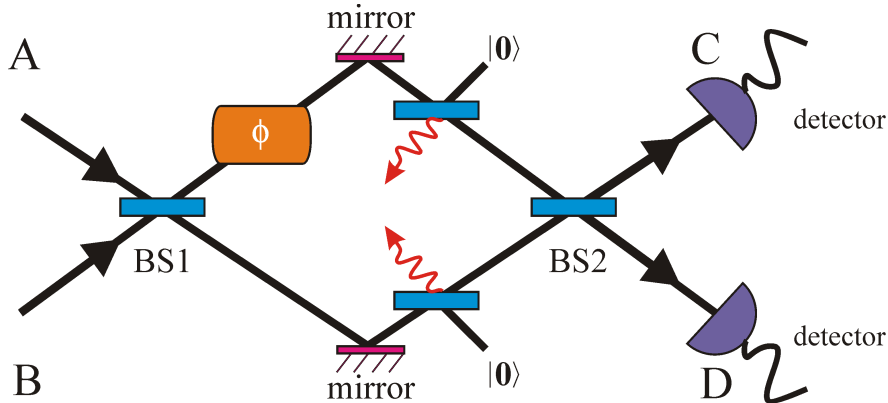


Figure 2.4: Mach–Zehnder interferometer with imaginary beam splitters which model the particle losses. The unused output ports are traced out in order to estimate the effect of losses.

If the input to the normal Mach–Zehnder interferometer in Fig (2.1) is taken to be $|N_1, N_2\rangle$, with $N = N_1 + N_2$, the resulting phase precision is given by (Kim *et al.*, 1998)

$$\Delta\phi^2 = \frac{N_1 + 2N_1N_2 + N_2}{(N_1 - N_2)^2}. \quad (2.34)$$

When $N_1 = N$ and $N_2 = 0$, we recover the result for the uncorrelated state which gives a shot-noise scaling $\sim 1/\sqrt{N}$. However, when the input state is the twin Fock state with $N_1 = N_2 = N/2$, we see from the last expression that the phase resolution diverges $\Delta\phi^2 \rightarrow \infty$, meaning that no information of the unknown phase shift can be obtained if we only measure expectation values related to the output-port difference operator \hat{M} .

Although the difference in the number of particles at the output ports does not contain any information about the phase resolution for the twin Fock state, their product does contain useful information about the phase. Defining the output-port coincidence operator as $\hat{N}_c = (\hat{c}^\dagger \hat{c})(\hat{d}^\dagger \hat{d})$, the phase precision can be obtained by a simple manipulation of the errors in a similar way as we did before, resulting in

$$\Delta\phi^2 = \frac{\Delta N_c^2}{|\partial\langle\hat{N}_c\rangle/\partial\phi|^2}. \quad (2.35)$$

After some algebra, it can be shown that this last expression gives the following

2.2 Precision scaling for well-known input states

phase precision for the bat state (Kim *et al.*, 1998)

$$\Delta\phi^2 = \frac{1}{2N^2} + \frac{1}{8} \tan^2 \phi. \quad (2.36)$$

Therefore, for a null phase shift, we obtain Heisenberg-limited phase resolution $\sqrt{2}/N$, which is only slightly worse than that of a $N00N$ state. Unfortunately, along with this enhancement in the precision, there is a major drawback to measuring a phase using coincidences at the output ports. When the detectors are not ideal, that is, their efficiency is smaller than one, it has been shown that in order to beat the shot-noise limit, the efficiencies in the detectors need to be better than $1 - 1/\sqrt{N}$ and, to attain the Heisenberg limit, efficiencies better than $1 - 1/N$ are needed (Kim *et al.*, 1999). The finite efficiency of any realistic detector imposes a serious limitation when the particles are any more than a handful of them, deterring the purpose of using an entangled state to improve the phase precision. However, this problem can be overcome by making use of collapses and revivals of the relative phase of the output state (Dunningham & Burnett, 2004), thus allowing us to attain Heisenberg-limited precision using bat states.

The real advantage of bat states is, as mentioned earlier, their robustness to particle losses, which makes them ideal for realistic quantum metrology schemes. In fact, bat states with roughly 10^4 ^{87}Rb atoms have been experimentally demonstrated, showing a substantial improvement over the shot-noise limit (Luecke *et al.*, 2011). However, detection inefficiency drastically affects the precision of measurements in this experiment, where they show that the smallest phase precision with their setup is $\sim 0.83/\sqrt{N}$, which is below the sub-shot noise limit but the scaling is not Heisenberg scaling at all. This experiment shows that even if entanglement is produced for a large number of particles, the actual read-out of the phase is usually a very challenging endeavour if we want to obtain Heisenberg-limited precision.

In order to study the effect of particle losses inside the interferometer, we need to introduce a standard tool in quantum metrology called the quantum Fisher information which bounds the accuracy of the phase precision regardless of the measuring scheme.

2.3 Quantum Fisher information

The actual precision of a measurement as obtained with a particular scheme depends on the details of such scheme and the measuring procedure, as it is evident from our earlier example of the bat state where measuring the imbalance of particles at the output ports resulted in an infinitely imprecise measurement, but the use of coincidences allowed for a Heisenberg-limited precision. In this case, the use of coincidences provides an optimal measurement scheme for the bat state with ideal detectors, as we shall see shortly, but it is not evident at all how one can find and realise optimal measurement schemes for any given quantum state. The concept of quantum Fisher information partially fills this gap by providing us with a lower bound for the precision of any measurement of an unknown parameter, i.e. provides the ultimate optimal precision attainable for a given quantum state. Finding the actual measurement scheme that saturates this lower bound is more difficult, but the Fisher information can be a good guide on this quest.

In order to find the lower bound for phase precision, it is first shown that the precision is bounded by the inverse of the classical Fisher information for a given measurement; then, the classical Fisher information is minimised over all possible measurements showing that the classical Fisher information of any given measurement is bounded by the quantum Fisher information, which is independent of the measurement. This derivation was carried out in detail by Braunstein and Caves ([Braunstein & Caves, 1994](#)), where they gave a less obscure proof of the quantum Cramér-Rao bound than the one first given by Helstrom ([Helstrom, 1967](#)). Here, we briefly outline their derivation to introduce the concept of quantum Fisher information and the Cramér-Rao bound.

In classical estimation theory, one attempts to estimate an unknown parameter ϕ which is encoded in the probability density $f(x|\phi)$ of a random variable x by using an estimator function $\Phi(x_1, x_2, \dots, x_n)$, where x_1, \dots, x_n are random variables corresponding to n outcomes of n probabilistic experiments for the given distribution. For example, ϕ could be the average height of a given large population of people, and the estimator function could be the mean value of heights in a sample of n people, i.e. $\Phi(x_1, x_2, \dots, x_n) = (x_1 + x_2 + \dots + x_n)/n$. Associated with

2.3 Quantum Fisher information

the estimator function and the original distribution, there is a conjoint probability density $P(x_1, x_2, \dots, x_n | \phi)$ which in the case of independent variables can be written as

$$P(x_1, x_2, \dots, x_n | \phi) = f(x_1 | \phi) f(x_2 | \phi) \cdots f(x_n | \phi). \quad (2.37)$$

If the estimator is assumed to be unbiased, its average value is equal to the unknown parameter, thus

$$\int (\Phi(x_1, x_2, \dots, x_n) - \phi) f(x_1 | \phi) f(x_2 | \phi) \cdots f(x_n | \phi) dx_1 dx_2 \cdots dx_n = 0. \quad (2.38)$$

Differentiating this identity with respect to ϕ and applying the Cauchy-Schwarz inequality gives

$$\Delta\phi^2 \geq \frac{1}{nF}, \quad (2.39)$$

where $\Delta\phi^2$ is the variance associated with the sampling of the estimator function, and F is the classical Fisher information given by

$$F = \int \left(\frac{\partial \ln f(x | \phi)}{\partial \phi} \right)^2 f(x | \phi) dx. \quad (2.40)$$

The inequality in Eq.(2.39) is the classical Cramér-Rao bound, and it holds for classical and quantum systems under the assumptions made here. However, as we shall see shortly, the classical Fisher information depends on the chosen Hermitian operator that represents the measurement; therefore, it does not give an ultimate lower bound for the phase precision.

In quantum metrology, all the statistical information about the unknown phase is encoded in the density matrix $\rho(\phi)$, corresponding to the quantum state of the interferometer before a measurement takes place. A generalised measurement is described by a set of non-negative Hermitian operators $\hat{X}(x)$, where x is a particular outcome for the measurement, and the operators are complete in the sense that

$$\int \hat{X}(x) dx = \mathbb{1}. \quad (2.41)$$

The probability density of obtaining the value x as the outcome of a measurement represented by \hat{X} is given by the standard expression from quantum mechanics

$$f(x | \phi) = \text{Tr} \left[\hat{X}(x) \rho(\phi) \right]. \quad (2.42)$$

2.3 Quantum Fisher information

Substituting this expression in the classical Fisher information gives

$$F(\hat{X}) = \int \frac{\left(\text{Tr} \left[\hat{X} \rho'(\phi) \right] \right)^2}{\text{Tr} \left[\hat{X} \rho(\phi) \right]} dx, \quad (2.43)$$

where $\rho'(\phi) = \partial\rho/\partial\phi$, and as we can see, it depends on \hat{X} as was mentioned before.

Now, introducing the symmetric logarithmic derivative λ , which is implicitly defined by

$$\frac{\partial\rho(\phi)}{\partial\phi} = \frac{1}{2} (\lambda\rho(\phi) + \rho(\phi)\lambda), \quad (2.44)$$

and making use of one of its properties $\text{Tr} [B\rho'(\phi)] = \text{Tr} [\rho(\phi)B\lambda]$, where B is any Hermitian operator, the Fisher information can be expressed as

$$F(\hat{X}) = \int \frac{\left(\text{Re} \left(\text{Tr} \left[\rho(\phi) \hat{X} \lambda \right] \right) \right)^2}{\text{Tr} \left[\hat{X} \rho(\phi) \right]} dx \leq \int \frac{\left| \text{Tr} \left[\rho(\phi) \hat{X} \lambda \right] \right|^2}{\text{Tr} \left[\hat{X} \rho(\phi) \right]} dx. \quad (2.45)$$

Finally, making use of the cyclic properties of the trace on the integral in the far right, and applying the Schwarz inequality ([Braunstein & Caves, 1994](#)) gives

$$\int \frac{\left| \text{Tr} \left[\rho(\phi) \hat{X} \lambda \right] \right|^2}{\text{Tr} \left[\hat{X} \rho(\phi) \right]} \leq \text{Tr} \left[\rho(\phi) \lambda^2 \right]. \quad (2.46)$$

The term on the far right is the quantum Fisher information

$$F_Q = \text{Tr} \left[\rho(\phi) \lambda^2 \right], \quad (2.47)$$

which is independent of \hat{X} as needed. Consequently, we have

$$\Delta\phi^2 \geq \frac{1}{nF} \geq \frac{1}{nF_Q}, \quad (2.48)$$

which is the quantum Cramér-Rao bound and determines the ultimate best possible precision with which a quantum system can determine the parameter ϕ , independent of the measurement process.

It is possible to show that for a pure states $|\Psi(\phi)\rangle$, the quantum Fisher information simplifies to

$$F_Q [|\Psi(\phi)\rangle] = 4 \left[\langle \Psi'(\phi) | \Psi'(\phi) \rangle - |\langle \Psi'(\phi) | \Psi(\phi) \rangle|^2 \right], \quad (2.49)$$

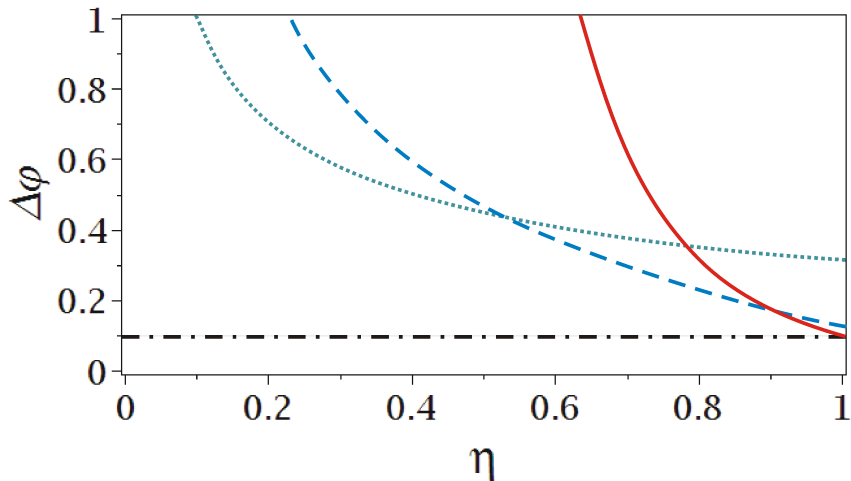


Figure 2.5: Phase precision in a Mach–Zehnder interferometer with particle losses as a function of the transmissivity η for different input states with $N = 10$ particles. The solid red line corresponds to a $N00N$ state, the blue dashed line to a bat state, the turquoise dotted one corresponds to uncorrelated particles with losses, and the black dash-dotted line is the Heisenberg limit. Adapted from (Cooper *et al.*, 2010).

where $|\Psi'(\phi)\rangle = \partial|\Psi(\phi)\rangle/\partial\phi$, and this expression will provide the workhorse for calculation of Fisher information throughout the thesis.

For future reference, it is worth stating the quantum Fisher information for $N00N$ and bat states, which are given by N^2 , and $N(N + 2)/2$, respectively.

2.4 Particle loss

Particle losses can be one of the major mechanisms of decoherence for entangled states, particularly in Bose–Einstein condensates, where collisions between atoms can result in some of them acquiring enough energy to escape the trapping potential or be recombined as a molecule, thus leaving the condensed state. The most simple model to account for particle losses in a Mach–Zehnder interferometer involves the addition of two imaginary beam splitters inside the interferometer whose transmissivity represents the rate of loss at the point where the imaginary beam splitter is located. The scheme is shown in Fig. (2.5), where it is assumed

2.5 Rotating Bose–Einstein condensates

that losses are equally likely from both modes and thus the transmissivity coefficient η is the same for both beam splitters.

Calculation of the quantum Fisher information for this set-up allows us to find the best possible precision when decoherence is present in the setup. Accounting for the presence of the imaginary beam splitters results in a mixed state inside the interferometer, and analytical determination of the Fisher information for the $N00N$ or bat states becomes difficult. (Cooper *et al.*, 2010) have calculated the Fisher information numerically for $N = 10$ particles, and the resulting bound for the phase precision is shown in Fig. (2.5). As we might expect, the $N00N$ state performs better than the bat state or uncorrelated particles when there are no losses, i.e. $\eta = 1$. However, as soon as there are around $\sim 20\%$ of losses, the uncorrelated particles outperforms the $N00N$ state, whereas the bat state still performs much better than the uncorrelated particles at this loss rate. Even when losses are close to 50%, the bat state still shows an advantage over uncorrelated particles. Since it is very unlikely than in a good experiment half of the atoms are lost, the bat state offers a feasible experimental advantage over the classical input states in precision measurement schemes.

2.5 Rotating Bose–Einstein condensates

Unlike a conventional fluid, a Bose–Einstein condensate does not undergo rigid body rotation, and this unusual feature gives rise to very interesting quantum effects in rotating BECs. The rotation of a Bose–Einstein condensate leads to the formation of quantised vortex lines, which can be present in different configurations, and can open the possibility of creating strongly correlated ground states. From the metrology point of view, these strongly correlated states are attractive for implementations of high-precision measurements, since we saw earlier that entangled states can achieve sub-shot noise precision in interferometric schemes. The research in this thesis is based on the properties of slowly rotating BECs; therefore, here we give a brief overview of this topic to establish the context of our research, and in the next chapter, we will consider in detail the rotational motion of a Bose–Einstein condensate.

2.5 Rotating Bose–Einstein condensates

In the mean-field treatment of a trapped Bose–Einstein condensate, the quantum state of the condensate is described by the wave function $\psi(\vec{x})$, usually called the “order parameter”, and its squared absolute value $|\psi(\vec{x})|^2 = n(\vec{x})$ gives the non-uniform density of particles inside the trap. This wave function can be expressed in terms of its amplitude and phase as $\psi(\vec{x}) = \sqrt{n(\vec{x})}e^{i\phi}$, and the velocity field inside the condensate is then given by (Pethick & Smith, 2008)

$$\vec{v} = \frac{\hbar}{M} \vec{\nabla} \phi, \quad (2.50)$$

where M is the particle mass. Taking the curl of this velocity gives

$$\vec{\nabla} \times \vec{v} = 0. \quad (2.51)$$

We see that in the case of a BEC, the flow is irrotational. At first sight, this result leads to a paradox when describing the behavior of the rotating BEC. For instance, in the case of a conventional fluid, the viscous drag between the walls of the container and the fluid generate a velocity field (far from the walls) analogous to the motion of a rotating solid, for which the vorticity is uniform and equal to $\vec{\nabla} \times \vec{v} = 2\vec{\Omega}$, where $\vec{\Omega}$ is the angular rotation vector. As a result, the free surface of the liquid acquires a characteristic parabolic shape. Therefore, since $\vec{\nabla} \times \vec{v} = 0$ for a BEC, we could expect its free surface to be undisturbed. However, experiments show that just as in the case of a conventional fluid, the free surface of a fast rotating BEC is a parabola.

The paradox can be resolved by noting that the irrotational nature of the flow in a BEC is a result of considering that the phase is a smooth function of the position; however, if the condensate phase ϕ has a line-like singularity, from the single-valuedness of the condensate wave function, it follows that the circulation around such singularity must be quantised as (Pethick & Smith, 2008)

$$\oint \vec{v} \cdot d\vec{l} = \frac{\hbar}{M} \times l, \quad (2.52)$$

where l is an integer number. These quantised line-like singularities are the quantised vortex lines, and their appearance is the mechanism that allows the condensate to acquire angular momentum. The condensate density vanishes at the exact location of the vortex line, and the density rapidly falls to zero in a scale

2.5 Rotating Bose–Einstein condensates

set by the so-called healing length $\xi = 1/\sqrt{8\pi\bar{n}a_s}$, where \bar{n} is the mean density and a_s is the s-wave scattering length.

In most experiments, the rotation frequency of the condensate is such that the mean inter-vortex spacing a_v is small compared with the condensate size, allowing a large number of vortices to be observed, which can be up to 160 (Cooper, 2008). In this typical condition, the BECs are in the regime $\xi \leq a_v$ where the structure of the vortex array is mainly determined by the interplay between trapping and the Magnus force. The role of the trapping force is to attract the vortices to the centre of the trap, while the Magnus force effect results in a net repulsion between two corotating vortices.

2.5.1 Rapidly rotating condensates

Notably, for high rotation frequencies, the condensate enters a regime of high vortex density where the separation between vortices a_v becomes much smaller than the healing length ξ , and the number of vortices is comparable to the number of particles. In this case, the atom cloud expands in its transverse dimension because the quadratic confinement potential is nearly balanced by the centrifugal potential which is also quadratic; as a consequence, the density of the condensate drops down and the mean interaction between particles is reduced. As the rotation frequency gets higher, the system enters a strongly correlated phase, which is understood as a bosonic analogue to the correlated phases of electrons in semiconductors, responsible for the quantum Hall effect. In order to reach these strongly correlated states, the rotation frequency needs to be exceedingly close to the centrifugal limit, typically $\sim 0.99\omega_\perp$, where ω_\perp is the harmonic frequency of the trap, this in turn means total angular momentum of the order of $\sim \hbar N^2$. The Boulder group has been able to achieve this high rotation regime by using a technique called “evaporative spin up” (Schweikhard *et al.*, 2004), as evidenced by the observation of very low frequency Tkachenko modes.

The physics of very rapidly rotating condensates is reminiscent of a charged particle in a magnetic field. A particle in the rotating condensate, located at position \vec{x} , experiences a force which in the rotating frame is the sum of the

2.5 Rotating Bose–Einstein condensates

trapping, centrifugal and Coriolis terms

$$\vec{F} = -M\omega_{\perp}^2\vec{x} + M\Omega^2\vec{x} + 2M\vec{\Omega} \times \vec{v}. \quad (2.53)$$

When the rotation frequency reaches the centrifugal limit, i.e. $\Omega = \omega_{\perp}$, the only force acting on the particle is the Coriolis one, which is mathematically equivalent to the magnetic force experienced by a moving charged particle, where the equivalent charge and magnetic field are given by $q\vec{B} = 2M\vec{\Omega}$. Then, for rapidly rotating BECs, we can borrow some of the results from familiar studies of the quantum Hall effect to describe bosonic systems. In particular, the energy spectrum is found to be tightly grouped in quasi-degenerate Landau levels (Cooper, 2008). The concept of Landau levels plays a very important role in this thesis and will be addressed in great detail in the next chapter.

As a final note to this section, it is worth mentioning that there have been a large number of proposals to use Bose–Einstein condensate in different rotating geometries in order to achieve sub-shot noise precision in measurements of rotations. For example, BECs in a lattice of potential nodes in a ring configuration allow to create $N00N$ and bat states, and perform rotation measurements with sub-shot noise precision (Cooper *et al.*, 2010). A Bose–Einstein condensate trapped in a one-dimensional ring with a moving barrier that helps to stir the condensate around the loop has been shown to allow for the creation of $N00N$ states and a Tonks-Girardeau state which is robust against particle losses (Hallwood *et al.*, 2010). Finally, some of the most precise rotation sensors have been achieved using cold atoms in a Sagnac interferometer (Gustavson *et al.*, 2000), and although the precision is still limited by the sub-shot noise, the use of even colder atoms, i.e. Bose–Einstein condensates, could make it possible to create practical gyroscopes which surpass the classical limit.

Chapter 3

Bose–Einstein condensate in an anisotropic rotating trap

We saw in chapter 2 that the use of quantum entangled states as inputs to interferometers leads to the possibility of attaining sub-shot noise precision for measurements of different physical magnitudes. Particularly, much work has been carried out regarding measurements of angular rotation, and different measurement scheme proposals have been put forward (Dunningham & Hallwood, 2006; Dunningham J.A. & D.W., 2011; Holland & Burnett, 1993; Nunnenkamp *et al.*, 2008; Zimmer & Fleischhauer, 2006). Some of these works have shown that the use of Bose–Einstein condensates in different rotating geometries allow for the creation of highly entangled states, useful for measuring rotation rates with sub-shot noise precision. In this chapter, we follow the lead of (Dagnino *et al.*, 2009a) and study a simple promising system to generate macroscopic entanglement. The system is a relatively slow rotating two-dimensional BEC in a stirring anisotropic trap which has been experimentally demonstrated in the past (Madison *et al.*, 2000a). As the rotation frequency increases, a certain critical frequency Ω_c is reached for which the ground state develops quantum correlations with entanglement. We study the performance of this state for quantum metrology schemes by calculating the quantum Fisher information, finding (Rico-Gutierrez *et al.*, 2013) that it allows for sub-shot noise precision in linear interferometry.

3.1 Model

We study the system considered in (Dagnino *et al.*, 2009a), a mesoscopic sample of N bosonic atoms of mass M in an axially symmetric harmonic potential, with frequency ω_\perp in the xy plane and ω_z in the z axis, weakly interacting through hard-core-type elastic collisions. Additionally, the gas is set in rotation at angular frequency Ω around the z axis with the aid of an external potential which in the rotating frame of reference appears as an anisotropic quadratic potential V in the xy plane. Thus, the Hamiltonian in the rotating frame of reference is

$$H = \sum_{i=1}^N \left(-\frac{\hbar}{2M} \nabla_i^2 + \frac{1}{2} M \omega_z z_i^2 + \frac{1}{2} M \omega_\perp^2 \rho_i^2 + 2AM \omega_\perp^2 (x_i^2 - y_i^2) - \Omega L_{zi} \right) + \frac{1}{2} \sum_{j \neq k}^N \frac{g \hbar^2}{M} \delta(\vec{\mathbf{r}}_j - \vec{\mathbf{r}}_k), \quad (3.1)$$

where the dimensionless parameter $A (\ll 1)$ measures the strength of the anisotropy and it will be considered very small so that we can find a truncated many-body basis for which the solutions to the Hamiltonian converge. Here, $\rho_i^2 = x_i^2 + y_i^2$ and L_{zi} is the angular momentum component in the z direction of the i -th atom. The addition of the term $-\vec{\Omega} \cdot \vec{L}$ to the Hamiltonian is the well-known (Fetter, 2009) prescription for transforming to the rotating frame. Finally, for dilute gases, the scattering of a pair of particles is dominated by the s-wave contribution thus the interactions can be modeled using an effective contact potential which is the two-particle operator U at the right-most of Eq.(3.1), where g is the 3D interaction coupling constant which measures the strength of two-particle interactions, and is related to the three-dimensional scattering length a_s as $g = 4\pi a_s$ (Pethick & Smith, 2008).

The natural approach to this many-body problem is the second quantisation formalism. In order to express Eq.(3.1) in second quantised form, we need the matrix elements appearing in the general form for one- and two-particle operators, which are, respectively (Bruus & Flensberg, 2004)

$$\hat{T} = \sum_{n_1, n_2} T_{n_1 n_2} a_{n_1}^\dagger a_{n_2}, \quad (3.2)$$

$$\hat{V} = \frac{1}{2} \sum_{m_1, m_2} \sum_{n_1, n_2} V_{m_1 m_2, n_1 n_2} a_{m_1}^\dagger a_{m_2}^\dagger a_{n_1} a_{n_2}, \quad (3.3)$$

where the matrix elements are obtained as,

$$T_{n_1 n_2} = \int \psi_{n_1}^*(\vec{r}) T \psi_{n_2}(\vec{r}) d^3 \vec{r}, \quad (3.4)$$

$$V_{m_1 m_2, n_1 n_2} = \int \int \psi_{m_1}^*(\vec{r}_1) \psi_{m_2}^*(\vec{r}_2) V \psi_{n_1}(\vec{r}_1) \psi_{n_2}(\vec{r}_2) d^3 \vec{r}_1 d^3 \vec{r}_2. \quad (3.5)$$

The wave functions $\psi_n(\vec{r})$ are the solutions to the single-particle problem for the Hamiltonian considered in Eq.(3.1), which are found by solving the Schrödinger equation,

$$\left(-\frac{\hbar}{2M} \nabla^2 + \frac{1}{2} M \omega_{\perp}^2 \rho^2 + \frac{1}{2} M \omega_z^2 z^2 - \Omega L_z + 2AM \omega_{\perp}^2 (x^2 - y^2) \right) \psi(\vec{r}) = E \psi(\vec{r}). \quad (3.6)$$

Consequently, in order to proceed with the second quantised treatment, we first have to solve Eq.(3.6); this is done in the following section.

3.1.1 Solving the single-particle Schrödinger equation

We start by solving Eq.(3.6) in the absence of the anisotropic term ($A = 0$); later on, we will see how to include this term back into the calculations at the level of the second quantisation formalism. Furthermore, since every term in the LHS of Eq.(3.6) commutes with L_z when $A = 0$, we only need to solve the following Schrödinger equation

$$\left(-\frac{\hbar}{2M} \nabla^2 + \frac{1}{2} M \omega_{\perp}^2 \rho^2 + \frac{1}{2} M \omega_z^2 z^2 \right) \psi(\vec{r}) = E \psi(\vec{r}). \quad (3.7)$$

That L_z commutes with $-\hbar \nabla^2 = \vec{p}^2$, ρ^2 and z^2 can be easily understood since L_z is the generator of rotations around the z axis and, under such a rotation, the modulus of the linear momentum and the radial coordinate transform as scalar quantities, and z remains unchanged by definition. The solutions to Eq.(3.7) are also eigenfunctions of $-\Omega L_z$ by the virtue of L_z commuting with all the operators appearing in the LHS of this equation, as was previously mentioned. We see that Eq.(3.7) is nothing but a two-dimensional harmonic oscillator in the xy plane with angular frequency ω_{\perp} and a one-dimensional harmonic oscillator in the z direction with angular frequency ω_z . This equation can be solved by the

standard treatment of separation of variables in cylindrical coordinates, where one assumes a solution which is a product of axial, azimuthal, and radial wave functions, $\psi(\vec{r}) = Z(z)\Phi(\phi)R(\rho)$. In cylindrical coordinates Eq.(3.7) reads,

$$\left(-\frac{\hbar^2}{2M} \left[\frac{1}{\rho} \frac{\partial}{\partial \rho} \left(\rho \frac{\partial}{\partial \rho} \right) + \frac{1}{\rho^2} \frac{\partial^2}{\partial \phi^2} + \frac{\partial^2}{\partial z^2} \right] + \frac{1}{2} M \omega_{\perp}^2 \rho^2 + \frac{1}{2} M \omega_z^2 z^2 \right) \psi(\vec{r}) = E \psi(\vec{r}) \quad (3.8)$$

When the proposed solution is substituted in the previous equation, it leads to an immediate decoupling of the partial differential equation into

$$\left(-\frac{\hbar^2}{2M} \frac{\partial^2}{\partial z^2} + \frac{1}{2} M \omega_z^2 z^2 \right) Z(z) = E_z Z(z), \quad (3.9)$$

and

$$\begin{aligned} \left(-\frac{\hbar^2}{2M} \left[\frac{1}{\rho} \frac{\partial}{\partial \rho} \left(\rho \frac{\partial}{\partial \rho} \right) + \frac{1}{\rho^2} \frac{\partial^2}{\partial \phi^2} \right] + \frac{1}{2} M \omega_{\perp}^2 \rho^2 \right) \Phi(\phi) R(\rho) \\ = E_{\perp} \Phi(\phi) R(\rho), \end{aligned} \quad (3.10)$$

where $E = E_z + E_{\perp}$. Further algebraic manipulation of the last equation leads to a decoupling of the radial and azimuthal degrees since Eq.(3.10) can be cast into the form

$$\begin{aligned} \frac{\rho^2}{R(\rho)} \frac{\partial^2}{\partial \rho^2} R(\rho) + \frac{\rho}{R(\rho)} \frac{\partial}{\partial \rho} R(\rho) - \frac{2M}{\hbar^2} \left[E_{\perp} \rho^2 - \frac{1}{2} \omega_{\perp}^2 \rho^4 \right] + \frac{1}{\Phi(\phi)} \frac{\partial^2}{\partial \phi^2} \Phi(\phi) \\ = 0. \end{aligned} \quad (3.11)$$

Consequently, the decoupled azimuthal equation is

$$\frac{1}{\Phi(\phi)} \frac{\partial^2}{\partial \phi^2} \Phi(\phi) = -m_l^2, \quad (3.12)$$

which has the well-known solution

$$\Phi(\phi) = e^{im_l \phi}, \quad (3.13)$$

where m_l is a separation constant giving the quantum number for the projection of the angular momentum in the z direction, as will be discussed later on. Since the wave functions must be single-valued, the constant can only assume discrete

values $m_l = 0, \pm 1, \pm 2, \dots$. Therefore, having decoupled the azimuthal equation, we are left with the radial equation

$$\frac{\partial^2}{\partial \rho^2} R(\rho) + \frac{1}{\rho} \frac{\partial}{\partial \rho} R(\rho) - \frac{m_l^2}{\rho^2} R(\rho) + \frac{2M}{\hbar^2} \left(E_{\perp} - \frac{1}{2} \omega_{\perp}^2 \rho^2 \right) R(\rho) = 0. \quad (3.14)$$

The solution to this equation can be cast into the form

$$R(\rho) = \rho^{|m_l|} e^{-\frac{1}{2} \frac{\rho^2}{\rho_0^2}} W(\rho), \quad (3.15)$$

where $\rho_0 = \sqrt{\frac{\hbar}{M\omega}}$ and $W(\rho)$ is a function of the radial coordinate. Substituting this solution in Eq.(3.14), we obtain

$$\rho \frac{\partial^2}{\partial \rho^2} W(\rho) + \left(2|m_l| + 1 - 2 \frac{\rho^2}{\rho_0^2} \right) \frac{\partial}{\partial \rho} W(\rho) + \left[\frac{2ME_{\perp}}{\hbar^2} - \frac{2(|m_l| + 1)}{\rho_0^2} \right] \rho W(\rho) = 0. \quad (3.16)$$

As a last algebraic manipulation, we multiply the last equation by $\frac{\rho_0^2 \rho_0^{|m_l|}}{\rho}$, followed by a change of variables, $W(\rho) = \frac{g(x)}{\rho_0^{|m_l|}}$ and $\rho = \rho_0 x$, leading to the new equation

$$x \frac{\partial^2}{\partial x^2} g(x) + [(|m_l| + 1) - x] \frac{\partial}{\partial x} g(x) - \frac{1}{2} \left[(|m_l| + 1) - \frac{E_{\perp}}{\hbar\omega_{\perp}} \right] g(x) = 0. \quad (3.17)$$

This is the well known Kummer–Laplace equation whose regular solution at $x = 0$ is the confluent hypergeometric function

$$g(x) = {}_1F_1(a, c; x) = M(a, c; x), \quad (3.18)$$

with

$$a = \frac{1}{2} \left[(|m_l| + 1) - \frac{E_{\perp}}{\hbar\omega_{\perp}} \right], \quad c = |m_l| + 1. \quad (3.19)$$

This means that the radial wave equation is given by

$$R(\rho) = N_R e^{-\frac{1}{2} \frac{\rho^2}{\rho_0^2}} \rho^{|m_l|} {}_1F_1(a, c; \rho^2/\rho_0^2), \quad (3.20)$$

where N_R is a normalisation constant. The confluent hypergeometric function converges for all finite ρ whether a and c are integers or not. However, $R(\rho)$

diverges when ρ tends to infinity, which is an unacceptable property of the wave function for bound states, unless a is 0 or a negative integer, in which case, the confluent hypergeometric function simply becomes a polynomial. Thus, we must have

$$a = \frac{1}{2} \left[(|m_l| + 1) - \frac{E_\perp}{\hbar\omega_\perp} \right] = -n_\rho, \quad (3.21)$$

where $n_\rho = 0, 1, 2, \dots$. This in turn means that the energy associated to the degrees of motion in the xy plane is quantised, which is explicitly stated by solving for E_\perp in the last equation, giving

$$E_\perp = 2\hbar\omega_\perp n_\rho + \hbar\omega_\perp (|m_l| + 1). \quad (3.22)$$

When $a = -n_\rho$, the confluent hypergeometric function becomes proportional to the associated Laguerre polynomials (Arfken, 1985)

$$F_1(-n_\rho, |m_l| + 1; \rho^2/\rho_0^2) = \frac{n_\rho! |m_l|!}{(n_\rho + |m_l|)!} L_{n_\rho}^{|m_l|}(\rho^2/\rho_0^2). \quad (3.23)$$

The solutions to the axial $Z(z)$ wave equation in Eq.(3.9) are nothing but the standard harmonic oscillator functions

$$Z(z) = N_Z e^{-\frac{1}{2} \frac{z^2}{z_0^2}} H_{n_z}(z/z_0), \quad (3.24)$$

where the H_{n_z} functions are the Hermite polynomials and $z_0 = \sqrt{\frac{\hbar}{M\omega_z}}$.

Thus, bringing all the pieces together, we see that the wave functions are of the form

$$\psi_{n_\rho m_l n_z}(\vec{r}) = N e^{-\frac{1}{2} \frac{z^2}{z_0^2}} H_{n_z}(z/z_0) e^{im_l \phi} e^{\frac{1}{2} \frac{\rho^2}{\rho_0^2}} \rho^{|m_l|} L_{n_\rho}^{|m_l|}(\rho^2/\rho_0^2), \quad (3.25)$$

and the respective energy levels are

$$E_{n_\rho m_l n_z} = \hbar\omega_z \left(n_z + \frac{1}{2} \right) + 2\hbar\omega_\perp n_\rho + \hbar\omega_\perp (|m_l| + 1). \quad (3.26)$$

Finally, we take into account the $-\Omega L_z$ term to obtain the complete solution to the single-particle problem. Since L_z commutes with all the terms of the Hamiltonian in Eq.(3.7), the solutions

$$\psi_{n_\rho m_l n_z}(\vec{r}) = N e^{-\frac{1}{2} \frac{z^2}{z_0^2}} H_{n_z}(z/z_0) e^{im_l \phi} e^{-\frac{1}{2} \frac{\rho^2}{\rho_0^2}} \rho^{|m_l|} L_{n_\rho}^{|m_l|}(\rho^2/\rho_0^2) \quad (3.27)$$

are also eigenfunctions of L_z . In fact, since $L_z = -i\hbar\frac{\partial}{\partial\phi}$, it is easily seen that

$$L_z\psi(\vec{r}) = \hbar m_l\psi(\vec{r}). \quad (3.28)$$

Therefore, when the anisotropy is $A = 0$, the solutions to our original problem, i.e., that of Eq.(3.6) are the same $\psi_{n_\rho m_l n_z}(\vec{r})$ appearing in Eq.(3.25). However, the energy levels are shifted and given by

$$E_{n_\rho m_l n_z} = \hbar\omega_z\left(n_z + \frac{1}{2}\right) + 2\hbar\omega_\perp n_\rho + \hbar\omega_\perp(|m_l| + 1) - \hbar m_l\Omega, \quad (3.29)$$

where $n_z = 0, 1, 2, \dots$, $n_\rho = 0, 1, 2, \dots$, and $m_l = 0, \pm 1, \pm 2, \dots$. In the rest of the thesis, we consider $\hbar\omega_z$ to be large compared with the interaction energy and the energy of the trap in the xy plane so that the dynamics along z is frozen and the gas is effectively two-dimensional at sufficiently low temperature. We need to perform a slight modification to our equations if we are to consider a 2D gas instead of a 3D one; we address this subject in the next section.

3.1.2 Two-dimensional rotating gas

When $\hbar\omega_z$ is much larger than the interaction strength and the energy of the trap in the xy plane, we assume that the system is in the ground state of the axial component, and integrate out the z dependence from Eq. (3.1) in order to find the corresponding two-dimensional Schrödinger equation for the condensate. Thus, we assume that all the N atoms are in the ground state of the axial trap $Z_0(z)$ and in some properly symmetrised quantum state in the plane $\Psi_{(2D)}(x_1, y_1, x_2, y_2, \dots, x_N, y_N)$. Consequently, for this quantum state of the system, the many-body Schrödinger equation is

$$\left(H_{xy} + H_z + g\frac{\hbar^2}{2M} \sum_{i \neq j} \delta^{(2D)}(\vec{\mathbf{r}}_i - \vec{\mathbf{r}}_j) \delta(z_i - z_j) \right) \Psi_{(2D)}\Psi_0 = E\Psi_{(2D)}\Psi_0, \quad (3.30)$$

where H_{xy} is the sum of single-particle Hamiltonians without including the axial trap term, H_z is the sum of harmonic trap potentials in the z direction for N particles, $\delta^{(2D)}(\vec{\mathbf{r}}_i - \vec{\mathbf{r}}_j) = \delta(x_i - x_j)\delta(y_i - y_j)$, and

$$\Psi_0 = Z_0(z_1)Z_0(z_2) \dots Z_0(z_N). \quad (3.31)$$

In order to obtain the two-dimensional Schrödinger equation for the gas, we multiply Eq.(3.30) by Ψ_0^* followed by an integration over $\int dz_1 dz_2 \dots dz_N$, giving

$$\left(H_{xy} + g \frac{\hbar^2}{2M} \sum_{i \neq j} \delta^{(2D)}(\vec{\mathbf{r}}_i - \vec{\mathbf{r}}_j) \int_{-\infty}^{\infty} \int_{-\infty}^{\infty} \delta(z_i - z_j) |Z_0(z_i)|^2 |Z_0(z_j)|^2 dz_i dz_j \right) \Psi_{(2D)} = \left(E - \frac{1}{2} \hbar \omega_z N \right) \Psi_{(2D)}. \quad (3.32)$$

The double integral in the last equation involving the axial ground state given by Eq. (3.24) for $n_z = 0$ is easily evaluated to $1/(\sqrt{2\pi}z_0)$. Therefore, the two-dimensional Schrödinger equation is given by

$$\left(H_{xy} + g^{(2D)} \frac{\hbar^2}{2M} \sum_{i \neq j} \delta^{(2D)}(\vec{\mathbf{r}}_i - \vec{\mathbf{r}}_j) \right) \Psi_{(2D)} = E^{(2D)} \Psi_{(2D)}. \quad (3.33)$$

We see that the two-dimensional Schrödinger equation is identical to the three-dimensional one except for the absence of any axial term and the fact that the interaction parameter is rescaled as $g^{(2D)} = g/(\sqrt{2\pi}z_0)$. We use this dimensionless parameter $g^{(2D)}$ to characterise the interaction strength in numeric calculations, where we drop the (2D) superscript and we simply write g , since from now on, we are only concerned with the two-dimensional gas.

Consequently, in the case of a two-dimensional Bose–Einstein gas, the single-particle solutions which satisfy this equation needed to quantise the many-body Hamiltonian are exactly the same ones that we already found in the previous section, which properly normalised are

$$\psi_{\mathbf{k}}(\rho, \phi) = \frac{\sqrt{n_{\mathbf{k}}!}}{\rho_0^{|m_{\mathbf{k}}|+1} \sqrt{\pi(n_{\mathbf{k}} + |m_{\mathbf{k}}|)!}} e^{im_{\mathbf{k}}\phi} e^{-\frac{\rho^2}{2\rho_0^2}} \rho^{|m_{\mathbf{k}}|} L_n^{|m_{\mathbf{k}}|}(\rho^2/\rho_0^2), \quad (3.34)$$

where \mathbf{k} is a collective index representing the distinct pair of numbers $(n_{\mathbf{k}}, m_{\mathbf{k}})$.

The corresponding energy levels are thus given by

$$E_{nm} = \hbar \omega_{\perp} (2n + |m| - m\Omega/\omega_{\perp} + 1). \quad (3.35)$$

These single-particle wave functions will be used to quantise the many-body Hamiltonian in order to find the solution to the problem of interacting particles in a rotating anisotropic trap. Nevertheless, it is instructive to have a closer look

at the energy spectrum of the non-interacting problem in order to introduce the concept of Landau levels which plays a very important role in this thesis. This is done in the next section, after a remark on the units used throughout the rest of this thesis.

3.1.3 Convention for units

For calculations, it is convenient to work with the standard unitless system consistently used in the literature (Fetter, 2009) where rotation frequencies are measured in units of the harmonic trap frequency ω_{\perp} , length in units of ρ_0 , time in units of $1/\omega_{\perp}$ and thus energy is measured in units of $\hbar\omega_{\perp}$, and angular momentum in units of \hbar . We assume the use of these units throughout the rest of the thesis and whenever it is needed to go back to the SI units, we place a tilde over the quantity to be expressed in the SI system.

3.1.4 Non-interacting particles and Landau levels

The energy spectrum of N independent bosons in a rotating axisymmetric trap ($A = 0$) can be obtained straightforwardly from expression (3.35), and it is given by

$$E = 2 \sum_{i=1}^N n_i + \sum_{i=1}^N |m_i| - \Omega L + N. \quad (3.36)$$

The dependence of the energy levels with Ω is completely different depending on whether the total angular momentum L is positive or negative. Assuming that a number k of bosons m_1, m_2, \dots, m_k have negative individual angular momentum while the rest of them m_{k+1}, \dots, m_N have positive angular momentum, the total

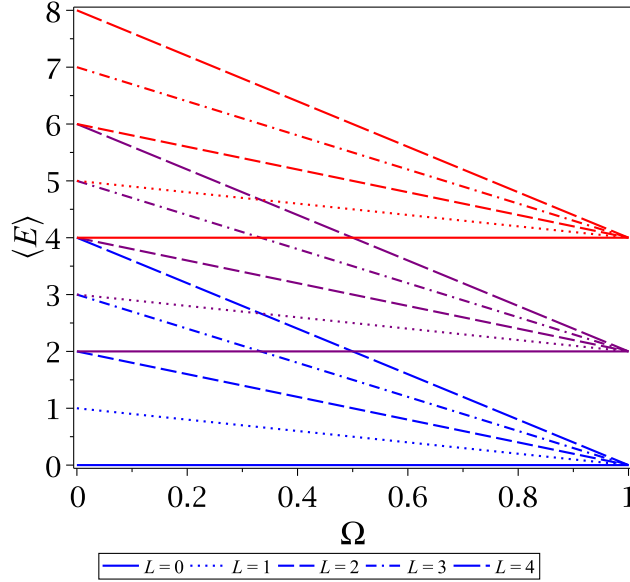


Figure 3.1: Energy spectrum of independent bosons in a rotating axisymmetric trap ($A = 0$) for positive total angular momentum $L \geq 0$. The energy levels are grouped in Landau levels which are energetically separated by $\sim 2\hbar\omega_{\perp}$ when $\Omega \approx \omega_{\perp}$. In this plot, the energy is given in units of $\hbar\omega_{\perp}$.

angular momentum of the N bosons can be expressed as

$$\begin{aligned}
 L = \sum_{i=1}^N m_i &= \sum_{i \leq k} m_i + \sum_{i > k} m_i \\
 &= -\sum_{i \leq k} |m_i| + \sum_{i > k} |m_i| \\
 &= -\sum_{i \leq k} |m_i| + \sum_{i > k} |m_i| + \left(-\sum_{i \leq k} |m_i| + \sum_{i \leq k} |m_i|\right) \\
 &= -2 \sum_{i \leq k} |m_i| + \sum_{i=1}^N |m_i|. \tag{3.37}
 \end{aligned}$$

Therefore, using Eq.(3.37) the energy spectrum for $L \geq 0$ can be written as

$$E = L(1 - \Omega) + 2 \left(\sum_{i \leq k} |m_i| + \sum_{i=1}^N n_i \right), \quad L \geq 0, \tag{3.38}$$

where we have omitted the zero point energy N for the sake of brevity. The energy spectrum given by Eq. (3.38) is shown in Fig. (3.1). The spectrum is structured in

groups called Landau levels. For the system to be in the lowest Landau level, none of the bosons must have radial excitations, i.e. all n_i are zero, nor possess negative angular momentum, i.e. all m_i are positive. Every Landau level comprises the states with all possible values of total angular momentum, where higher angular momentum corresponds to higher slope in the energy spectrum. In the limit of $\Omega = 1$, called the centrifugal limit, the energy of the ground state is infinitely degenerate and thus this case is singular. At this rotation frequency the trapping force is compensated by the centrifugal force, leaving only the Coriolis force.

When any particle has negative angular momentum or possesses radial excitations, the system is no longer in the lowest Landau level. In this case, the n_{LL} -th Landau level is defined as the manifold of energies given by the boson configuration satisfying the equation

$$n_{LL} = \sum_{i \leq k} |m_i| + \sum_{i=1}^N n_i + 1. \quad (3.39)$$

On the other hand, when the total angular momentum is negative, we use the expression in Eq. (3.37) again, and write $L = -|L|$ in Eq. (3.36) to express the energy as

$$E = |L|(\Omega - 1) + 2 \left(\sum_{i \leq k} |m_i| + \sum_{i=1}^N n_i \right), \quad L < 0. \quad (3.40)$$

We show the energy spectrum for this case in Fig. (3.2). Note that just like in the case of $L \geq 0$, the energy spectrum is still grouped in Landau levels; however, the spectrum looks completely different because the slope of the energy in each manifold is positive, as opposed to the previous case where it is negative. Also, since we have $\sum_{i > k} |m_i| \geq 0$, consequently

$$L \geq - \sum_{i \leq k} |m_i|. \quad (3.41)$$

Therefore, by virtue of this last expression and the fact that the level selector is given by Eq.(3.39), given a particular Landau level n_{LL} , there is a lower limit for the total angular momentum L that can appear in this level when $L < 0$, and

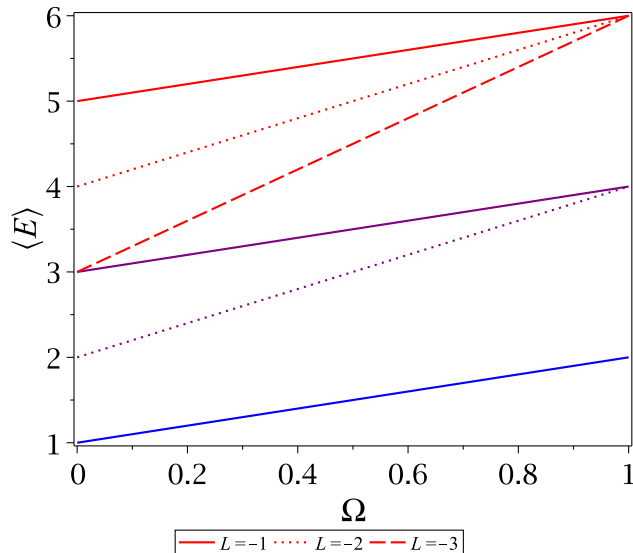


Figure 3.2: Energy spectrum of independent bosons in a rotating axisymmetric trap ($A = 0$) for negative total angular momentum $L < 0$. The energy levels are grouped in Landau levels which are energetically separated by $\sim 2\hbar\omega_{\perp}$ when $\Omega \approx \omega_{\perp}$. In this plot, the energy is given in units of $\hbar\omega_{\perp}$.

it is given by

$$L_{\min} \geq -\max \left\{ \sum_{i \leq k} |m_i| \right\} = -(n_{LL} - 1). \quad (3.42)$$

Consequently, the lowest Landau level does not contain negative total angular momentum states and these are only present for higher levels $n_{LL} > 1$.

The lowest Landau level bears a particular importance in the study of fast rotating Bose–Einstein condensates. For Ω close to the radial trap frequency, the energy levels are tightly packed, forming essentially horizontal rows called Landau levels, where the quantum number n determines the large splitting between these rows and the angular momentum quantum number m characterises the tightly packed states within the row. Thus, the ground state manifold corresponds to the lowest-lying of these rows, which is characterised by all the atoms having $m \geq 0$ and $n = 0$. When the interaction between particles is relatively weak, the energy spectrum remains grouped in Landau levels and thus for rotation

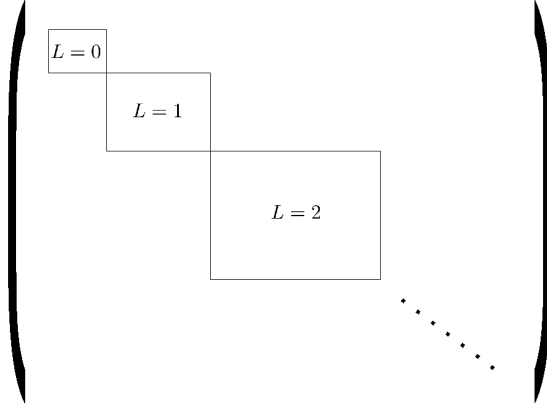


Figure 3.3: The many-body Hamiltonian is block diagonal in the basis of definite total angular momentum for a n_{LL} -th Landau level approximation when $A = 0$.

frequencies $\Omega \rightarrow 1$ the particles in the condensate occupy mostly the lowest Landau level states. This allows for a more tractable description of the system for both exact diagonalisation and mean-field studies because the single-particle states in Eq. (3.34) greatly simplify. We will introduce the lowest Landau level approximation in more detail for the exact diagonalisation of the many-body Hamiltonian in the next section after the quantisation of the theory.

3.2 Quantisation of the Hamiltonian

Following the usual prescription of second quantisation formalism with the help of the expressions in Eq.(3.4), the Hamiltonian can be expressed as

$$\begin{aligned} \hat{H} = & 2 \sum_{\mathbf{k}} n_{\mathbf{k}} \hat{N}_{\mathbf{k}} + \sum_{\mathbf{k}} |m_{\mathbf{k}}| \hat{N}_{\mathbf{k}} - \hbar \Omega \hat{L} + \hat{N} \\ & + \sum_{\mathbf{k}_1 \mathbf{k}_2} V_{\mathbf{k}_1 \mathbf{k}_2} \hat{a}_{\mathbf{k}_1}^\dagger \hat{a}_{\mathbf{k}_2} + \frac{1}{2} \sum_{\mathbf{k}_1 \mathbf{k}_2} \sum_{l_1 l_2} U_{\mathbf{k}_1 \mathbf{k}_2 l_1 l_2} \hat{a}_{\mathbf{k}_1}^\dagger \hat{a}_{\mathbf{k}_2}^\dagger \hat{a}_{l_1} \hat{a}_{l_2}. \end{aligned} \quad (3.43)$$

Here, $\hat{a}_{\mathbf{k}}^\dagger$ creates a boson in state $\mathbf{k} = (n_{\mathbf{k}}, m_{\mathbf{k}})$, $\hat{N}_{\mathbf{k}}$ is the occupation number operator of level \mathbf{k} and $\hat{L} = \sum_{\mathbf{k}} m_{\mathbf{k}} \hat{N}_{\mathbf{k}}$ is the total angular momentum operator of the system. The anisotropic and interaction term are given by Eqs.(A.7) and

3.2 Quantisation of the Hamiltonian

(A.13) found in Appendix A. These are

$$\begin{aligned} \hat{V} &= A\hbar\omega_{\perp} \sum_{\mathbf{k}_1\mathbf{k}_2} \sqrt{\frac{n_{\mathbf{k}_1}!n_{\mathbf{k}_2}!}{(n_{\mathbf{k}_1} + |m_{\mathbf{k}_1}|)!(n_{\mathbf{k}_2} + |m_{\mathbf{k}_2}|)!}} I_1(\mathbf{k}_1, \mathbf{k}_2) \\ &\quad \times \left(\delta_{m_{\mathbf{k}_2}, m_{\mathbf{k}_1} \pm 2} \right) a_{\mathbf{k}_1}^{\dagger} a_{\mathbf{k}_2}, \end{aligned} \quad (3.44)$$

and

$$\begin{aligned} \hat{U} &= \frac{g\hbar\omega_{\perp}}{2\pi} \sum_{\mathbf{k}_1\mathbf{k}_2\mathbf{l}_1\mathbf{l}_2} \frac{1}{2^{\frac{\sum |m_t|}{2}}} \sqrt{\prod_t \frac{n_t!}{(n_t + |m_t|)!}} I_2(\mathbf{k}_1, \mathbf{k}_2, \mathbf{l}_1, \mathbf{l}_2) \\ &\quad \times \left(\delta_{m_{\mathbf{k}_1} + m_{\mathbf{k}_2}, m_{\mathbf{l}_1} + m_{\mathbf{l}_2}} \right) \hat{a}_{\mathbf{k}_1}^{\dagger} \hat{a}_{\mathbf{k}_2}^{\dagger} \hat{a}_{\mathbf{l}_1} \hat{a}_{\mathbf{l}_2}. \end{aligned} \quad (3.45)$$

Having found the single-particle matrix elements for the quantised Hamiltonian, the next step consists in finding a suitable many-body basis for which the Hamiltonian can be diagonalised using numeric techniques. For this purpose, notice that due to the presence of $\delta_{m_{\mathbf{k}_1} + m_{\mathbf{k}_2}, m_{\mathbf{l}_1} + m_{\mathbf{l}_2}}$ in the interaction term \hat{U} , only states with the same total angular momentum are connected by this term. Furthermore, the first four terms appearing in the Hamiltonian in Eq.(3.43) conserve the total angular momentum. Thus, in the strict case of $A = 0$, the Hamiltonian has a block-diagonal form in a basis consisting of states with fixed number of particles and definite total angular momentum in Fock space which we write as

$$|\Phi_i\rangle = |N_{\mathbf{0}}(i), N_{\mathbf{1}}(i), \dots\rangle = \prod_{\mathbf{k}} \frac{(\hat{a}_{\mathbf{k}}^{\dagger})^{N_{\mathbf{k}}(i)}}{\sqrt{N_{\mathbf{k}}(i)}} |0\rangle, \quad (3.46)$$

where the index i defines a certain configuration for the occupation numbers $N_{\mathbf{k}}(i)$ which in turn specify the number of particles occupying each single-particle level labeled by the index \mathbf{k} introduced earlier. These states have definite angular momentum given by

$$\langle \hat{L} \rangle = \sum_{\mathbf{k}} m_{\mathbf{k}} N_{\mathbf{k}}. \quad (3.47)$$

In principle, this basis has an infinite number of states; thus, in order to find numeric solutions to the eigenvalue problem, we need to introduce approximations which truncate the basis in a sensible way. The first of these approximations is the standard recipe that consists of truncating the basis according to the number of

3.2 Quantisation of the Hamiltonian

Landau levels. The corresponding basis for a n_{LL} -th Landau level approximation consists of only those states satisfying the condition

$$\sum_{\mathbf{k}} \left[2n_{\mathbf{k}} + \frac{1}{2} (|m_{\mathbf{k}}| - m_{\mathbf{k}}) \right] N_{\mathbf{k}} \leq n_{\text{LL}} - 1. \quad (3.48)$$

This condition warrants that the maximum radial excitation or negative angular momentum that any particle can have is $n_{\text{LL}} - 1$ units.

Consequently, in the case of $A = 0$, the blocks of fixed L appearing in the Hamiltonian are of finite size and can be diagonalised separately in order to find the many-body ground state of the system. The structure of the Hamiltonian in this case is depicted in Fig. (3.3). Extensive numerical and analytical evidence (Jackson & Kavoulakis, 2000; Morris & Feder, 2006) show that for moderate rotation rates, only the states with $L \leq N$ are involved in the determination of the many-body ground state, whereas for rapidly rotating condensates with $\Omega \approx 0.999$, states with total angular momentum up to $N(N - 1)$ need to be considered.

When $A \neq 0$, the anisotropic term \hat{V} only connects subspaces of fixed L differing by ± 2 units of angular momentum because of the term $\delta_{m_{\mathbf{k}_2}, m_{\mathbf{k}_1} \pm 2}$. As a consequence, the blocks in the Hamiltonian can no longer be diagonalised separately and we are left again with an infinite-dimensional Hamiltonian; thus, another sensible truncation needs to be considered. In this thesis, the anisotropy $A \ll 1$ is considered small enough so it is expected that states with very high angular momentum do not contribute to the determination of the many-body ground state, and thus we can restrict the Hamiltonian matrix to the subspace of states with $L \leq L_{\text{max}}$, where the value of L_{max} is chosen to warrant a good convergence for the energies of the Hamiltonian (Dagnino *et al.*, 2009a). We address this approximation in more detail later on when presenting the results from the exact diagonalisation.

Now, we introduce the lowest Landau level approximation which is a central concept throughout the thesis.

3.2.1 The Lowest Landau Level approximation

We have seen that in the case of non-interacting particles, the many-body ground state belongs to the lowest Landau level manifold. Therefore, it is plausible to expect that in the case of weakly interacting bosons, the many-body ground state can be constructed using only states within this manifold. Restricting the single-particle solutions to the lowest Landau level, and the many-body basis states to configurations of bosons which only occupy these orbitals is known as the lowest Landau level (LLL) approximation .

In order to estimate how weak the interactions need to be so that the LLL approximation is still a good description of the system, we derive some of the standard conditions for the validity of this approximation as found in the literature. These standard conditions follow from a mean-field treatment of the rotating gas in a harmonic trap ($A = 0$). In such case, the energy of the condensate is given by the two-dimensional Gross-Pitaevskii energy functional (Pethick & Smith, 2008)

$$E[\psi(\vec{\mathbf{r}})] = \int \left[\frac{1}{2} |\nabla\psi(\vec{\mathbf{r}})|^2 + \frac{1}{2}\rho^2 |\psi(\vec{\mathbf{r}})|^2 - \Omega\psi^*(\vec{\mathbf{r}})L_z\psi(\vec{\mathbf{r}}) + g\frac{1}{2} |\psi(\vec{\mathbf{r}})|^4 \right] d^2\vec{\mathbf{r}}, \quad (3.49)$$

where $\psi(\vec{\mathbf{r}}) = N^{1/2}\phi(\vec{\mathbf{r}})$ is called the wave function of the condensate, ϕ is the single-particle wave function occupied by all the bosons in the fully condensed state, and we are using dimensionless units.

The energy functional in Eq.(3.49) can be considerably simplified by making use of the following relations for wave functions in the LLL (Aftalion *et al.*, 2005; Fetter, 2009),

$$\int |\vec{\nabla}\psi(\vec{\mathbf{r}})|^2 d^2\vec{\mathbf{r}} = \int \psi^*(\vec{\mathbf{r}})L_z\psi(\vec{\mathbf{r}})d^2\vec{\mathbf{r}} + N, \quad (3.50)$$

$$\int \psi^*(\vec{\mathbf{r}})L_z\psi(\vec{\mathbf{r}})d^2\vec{\mathbf{r}} = \int \rho^2 |\psi(\vec{\mathbf{r}})|^2 d^2\vec{\mathbf{r}} - N. \quad (3.51)$$

Thus, combining these two expressions with Eq.(3.49), the GP energy functional can be written as

$$E_{LLL}[\psi(\vec{\mathbf{r}})] = N\Omega + \int \left[(1 - \Omega)\rho^2 |\psi(\vec{\mathbf{r}})|^2 + \frac{1}{2}g |\psi(\vec{\mathbf{r}})|^4 \right] d^2\vec{\mathbf{r}}. \quad (3.52)$$

3.2 Quantisation of the Hamiltonian

Consequently, the ground state $\psi_{\min}(\vec{\mathbf{r}})$ that minimises the total energy E_{LLL} with the only constraint that it is normalised as $\int |\psi|^2 d^2\vec{\mathbf{r}} = N$, follows from the variational Euler–Lagrange equation

$$\frac{\partial}{\partial |\psi|^2} \left((1 - \Omega)\rho^2 |\psi(\vec{\mathbf{r}})|^2 + \frac{1}{2}g |\psi(\vec{\mathbf{r}})|^4 - \mu |\psi(\vec{\mathbf{r}})|^2 \right) = 0, \quad (3.53)$$

where the chemical potential μ is the Lagrange multiplier that ensures constancy of the particle number and takes care of the normalisation constraint in such a way that the variations of $|\psi|^2$ may thus be taken arbitrarily. As a result, Eq.(3.53) readily yields the density distribution

$$|\psi_{\min}(\rho)|^2 = n(0) \left(1 - \frac{\rho^2}{R_0^2} \right), \quad r < R_0, \quad (3.54)$$

where the central density is $n(0) = \mu/g$, $R_0^2 = \mu/(1 - \Omega)$, and the density vanishes for values of $\rho > R_0$. Finally, the chemical potential can be calculated in terms of the condensate parameters by inserting Eq.(3.54) in the normalisation condition, giving

$$\mu = \sqrt{\frac{2gN}{\pi}}(1 - \Omega). \quad (3.55)$$

Consequently, the central density and the condensate radius can also be expressed as

$$n(0) = \frac{2N}{\pi R_0^2}, \quad (3.56)$$

and

$$R_0^2 = \sqrt{\frac{2\pi gN}{1 - \Omega}}, \quad (3.57)$$

where the expression for the condensate radius explicitly shows the radial expansion of the condensate when $\Omega \rightarrow 1$; this is a consequence of the deconfinement of the condensate caused by the increasing centrifugal force.

Remarkably, the density distribution in Eq.(3.54) has the same functional form as that of the usual Thomas-Fermi approximation (Fetter, 2009) for a condensate at rest in a harmonic potential, i.e., an inverted parabola. However, one should be careful when pursuing this analogy further. In the usual Thomas-Fermi approximation, the kinetic energy is neglected and the density distribution that minimises the total energy is found as the consequence of a balance between potential and interaction energies. On the other hand, in the LLL approximation

3.2 Quantisation of the Hamiltonian

considered here, the kinetic and potential energies are actually equal, as can be seen from Eqs.(3.50) and (3.51).

In addition, notice that the function in Eq.(3.54) does not belong to the LLL since the only LLL function that depends solely on ρ is proportional to $\exp(-\rho^2/2\rho_0^2)$, as given by Eq.(3.34) with $n = 0$ and $m = 0$. This can be understood considering that during the minimisation process, we were free to choose the most suitable function that minimises the energy functional with the only restriction that it was normalised to N and that Eqs.(3.50) and (3.51) were satisfied. These two equations do not effectively restrict the wave function to the LLL manifold, they simply restrict the possible minimal density profile to those functions satisfying them, which includes those in the LLL manifold, as well as many others outside, such as the actual inverted parabola just found. Therefore, when a minimisation of the energy functional is performed restricted to only the LLL manifold, as it was first considered in (Ho, 2001), we are looking for a superposition of LLL wave functions which is the “closest” to Eq.(3.54) so that the corresponding energy is the closest to the minimal one calculated here.

Since the chemical potential μ determines the energy needed to add one boson in the condensate state ψ_{\min} , the lowest Landau level condition

$$\tilde{\mu} \ll 2\hbar\omega_{\perp}, \quad (3.58)$$

ensures that the LLL trial function gives a good description of the condensed state. This is the standard condition for the validity of the lowest Landau level approximation. Since $\mu = gn(0)$, the condition implies that the approximation is valid for weak interactions or small densities. Also, from Eq.(3.55), the standard condition $\mu \ll 2$ gives

$$gN \ll \frac{2\pi}{1 - \Omega}. \quad (3.59)$$

Therefore, even when the interactions are not weak, the LLL approximation is also valid for high rotation rates.

On the other hand, the validity of the lowest Landau level approximation has also been studied in the context of exact diagonalisation methods (Morris & Feder, 2006), giving consistent results in agreement with Eqs.(3.58) and (3.59) in the case of ground states with low angular momentum. However, when the

3.2 Quantisation of the Hamiltonian

N	Basis size for $n_{\text{LL}} = 1$	Basis size for $n_{\text{LL}} = 2$	Basis size for $n_{\text{LL}} = 3$
6	64	322	1282
8	136	728	3045
10	269	1506	6475
12	505	2934	12872

Table 3.1: A few different values of the many-body basis size for one, two and three Landau levels. Here, the truncation for total angular momentum states is $L = N + 2$, and only subspaces of even angular momentum are considered.

angular momentum of the ground state is comparable to $L \sim N^2$, the scaling of the condition in Eq.(3.59) drastically changes from $g \sim N^{-1}$ to $g \sim N^x$, where x is a positive number of order unity (Morris & Feder, 2006), and thus has important consequences in the study of the quantum Hall regime of strongly correlated states. In this thesis we are only concerned with ground states that have angular momentum $L \sim N$; therefore, in principle, the LLL approximation is valid in our case. As we shall see, the LLL approximation qualitatively describes all the relevant features of the system, and also many of its properties in a quantitative way. However, it fails to accurately describe some features relevant to quantum metrology. A deeper investigation of the system beyond the LLL approximation is presented in chapter 4. Here, we present results using only the LLL approximation for introduction and comparison purposes.

Therefore, in what follows, we restrict the many-body basis states to those in the lowest Landau level approximation; in other words, only those satisfying

$$\sum_{\mathbf{k}} \left[2n_{\mathbf{k}} + \frac{1}{2} (|m_{\mathbf{k}}| - m_{\mathbf{k}}) \right] N_{\mathbf{k}} = 0. \quad (3.60)$$

These consideration greatly reduces the many-body basis size, allowing for a more computationally tractable description of the system. We compare a few values of the many-body basis size for different numbers of particles and Landau levels in Table 3.1.

3.3 Diagonalisation of the Hamiltonian

3.3.1 The interacting case

Within the lowest Landau level approximation, the quantised Hamiltonian for $A = 0$ in Eq.(3.43) reduces to

$$\hat{H} = \hat{N} + (1 - \Omega)\hat{L} + \frac{g}{4\pi} \sum_{m_1, m_2} \sum_{n_1, n_2} \frac{\delta_{m_1+m_2, n_1+n_2}}{\sqrt{m_1! m_2! n_1! n_2!}} \frac{(m_1 + m_2)!}{2^{m_1+m_2}} a_{m_1}^\dagger a_{m_2}^\dagger a_{n_1} a_{n_2}, \quad (3.61)$$

where the operator \hat{a}_m^\dagger (\hat{a}_m) creates (annihilates) a boson with m units of angular momentum. Therefore, in a many-body basis of fixed total angular momentum, the first two terms on the RHS are diagonal and the ground state is completely determined by the interaction term.

As it was mentioned before, the interaction term only connects states with the same total angular momentum and thus we can diagonalise the Hamiltonian in these subspaces separately. The lowest lying state in energy for each of these subspaces is known as the yrast state, and its energy viewed as a function of L as the yrast line. For a given rotation frequency Ω , the yrast state with the absolute lowest energy gives the many-body ground state of the system at that particular rotation rate.

The yrast state and its energy for $L = 0$ and $L = 1$ are trivially obtained since these subspaces contain only one many-body basis state each; for N bosons, they are respectively

$$|N, 0, 0, \dots, 0\rangle, \quad (3.62)$$

and

$$|N - 1, 1, 0, \dots, 0\rangle. \quad (3.63)$$

Operating the Hamiltonian in Eq.(3.61) on these states gives their energies as

$$E_{L=0} = N + g \frac{N(N-1)}{4\pi}, \quad (3.64)$$

and

$$E_{L=1} = N + (1 - \Omega) + g \frac{N(N-1)}{4\pi}. \quad (3.65)$$

3.3 Diagonalisation of the Hamiltonian

For $L > 1$, finding the yrast line is not a trivial task. However, analytical expressions are known for $2 \leq L \leq N$ (Jackson & Kavoulakis, 2000; Wilkin & Gunn, 2000)

$$E_L = N + (1 - \Omega)L + gN \frac{2N - L - 2}{8\pi}, \quad (3.66)$$

where the $L = 1$ case does not have this form because it is a special case; it does not acquire angular momentum via the formation of a vortex but rather by the centre of mass motion (Parke *et al.*, 2008).

Analytical expressions of the yrast states for high values of L are also known, such as the one for the Laughlin state $L = N(N - 1)$.

On the other hand, extensive numerical research has been done to study the condensate in the axisymmetric trap (Bertsch & Papenbrock, 1999; Morris & Feder, 2006; Wilkin & Gunn, 2000). Here, we show numeric results obtained with our own codes, and review the most important results that have been discussed in the literature.

We show the many-body energy spectrum as a function of the rotation frequency Ω for two different values of the interaction strength in Fig. (3.4) The inclusion of interactions has the effect of lifting some of the degeneracy within subspaces of fixed total angular momentum. For small rotations, the ground state is the non-rotating $L = 0$ state of Eq.(3.62). As the rotation rate is increased, states with higher angular momentum experience a greater Doppler shift in energy (Morris & Feder, 2006). As a result, a sequence of energy crossings for the ground state occur at specific rotation frequencies $\Omega_1, \Omega_2, \dots$. Almost all these stable ground states can be described by the relationship $L = a(N - b)$, where a and b are integers. These values are very close to n -vortex states with $L = nN$ (Wilkin & Gunn, 2000). In this thesis, we focus on the $L = N$ state, commonly known as the single-vortex or one-vortex state. This state becomes stable at the rotation frequency

$$\Omega_1 = 1 - \frac{gN}{8\pi}. \quad (3.67)$$

In addition, all the other yrast states for $2 \leq L \leq N$ become metastable at Ω_1 , i.e. they are all degenerate in energy at this rotation frequency, as can be seen from Fig. (3.5).

3.3 Diagonalisation of the Hamiltonian

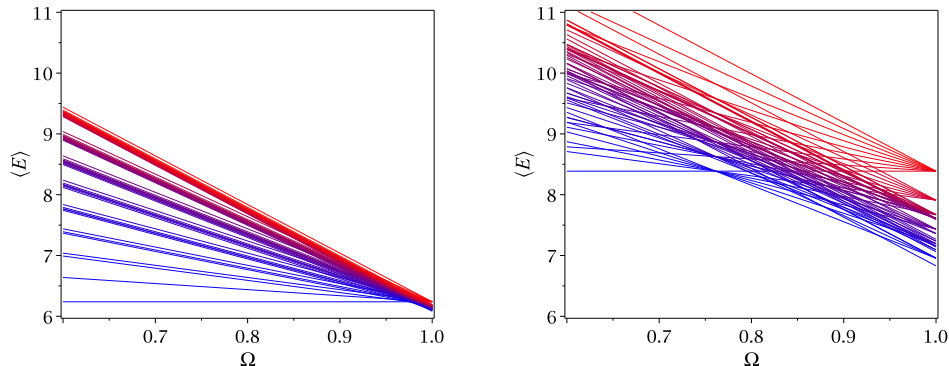


Figure 3.4: Energy spectrum for the case of $N = 6$ interacting particles in the isotropic case ($A = 0$) as a function of the rotation frequency. (Left) When the particles interact weakly with $g = 0.1$, the spectrum resembles the one for independent particles. (Right) As the interaction strength is increased, in this case $g = 1.0$, much of the degeneracy is lifted and a sequence of energy crossings are formed. The lowest Landau level approximation has been used for both panels, and the truncation of the basis is taken to be $L_{\max} = N + 2$; had we taken a larger L_{\max} , many more energy crossings would have appeared near the centrifugal limit $\Omega \sim 1$.

Thus, the ground state of the condensate at Ω_1 acquires angular momentum $L = N$ through the nucleation of the first vortex. In the current case of an axisymmetric trap, due to the rotational symmetry, the nucleation of the first vortex can only take place by means of a spontaneous symmetry breaking process. Within the standard mean-field framework, vortex nucleation is associated with thermodynamic instability, because the lowest lying states of the condensate around Ω_1 are quasi-degenerate and thus the system is very susceptible to perturbations; associated with this symmetry breaking process must be a gapless Nambu-Goldstone mode (Ueda & Nakajima, 2006).

The sharp transition of the ground state at Ω_1 is from the many-body non-rotating state $|N, 0, \dots, 0\rangle$ to the single-vortex state which is a linear combination of several different many-body states that pertain to the $L = N$ subspace. Interestingly, the vortex state $|0, N, 0, \dots, 0\rangle$ has the largest amplitude in this superposition, but it has less than half the probability (~ 0.49) of the complete

3.3 Diagonalisation of the Hamiltonian

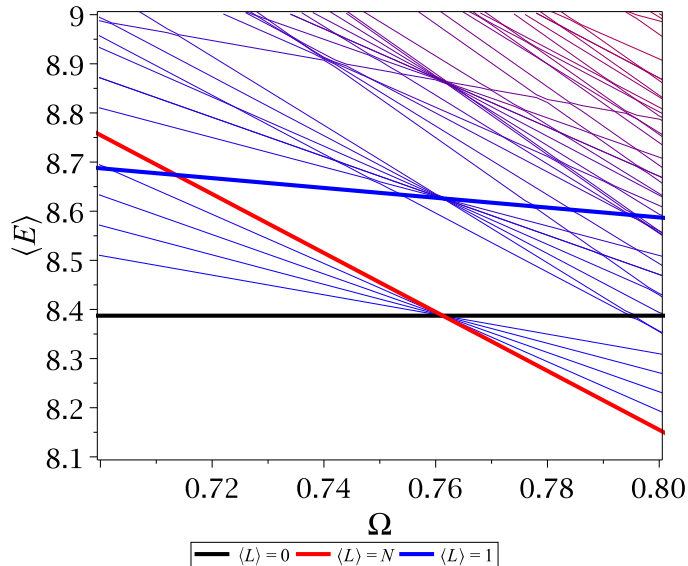


Figure 3.5: Energy spectrum for the case of $N = 6$ interacting particles in the isotropic case ($A = 0$) as a function of the rotation frequency. The first energy crossing corresponds to the nucleation of the first vortex in the ground state at the rotation frequency Ω_1 . All the yrast states with $0 < L \leq N$ except $L = 1$ are degenerate at this frequency. In this plot, we highlight the yrast line for the subspaces with $L = 0, 1$ and N . The lowest Landau level approximation has been used here, and the truncation of the basis is taken to be $L_{\max} = N + 2$.

many-body ground state. In fact, the single-vortex ground state for an even number of particles N is found to be well approximated by

$$|\Psi_0(\Omega_1)\rangle = \sum_{k=0}^{N/2} C_k |k, N - 2k, k, 0, \dots, 0\rangle, \quad (3.68)$$

where typically the states with up to $k = 4$ for $N \geq 4$ carry most of the probability. We show the amplitudes of the coefficients $|C_k|^2$ in Fig. (3.7). Moreover, an exact analytical expression for this state is known. The wave function of this single-vortex state is given by (Wilkin & Gunn, 2000)

$$\Psi_0(\Omega_1) = \prod_{i=1}^N (z_i - z_c) e^{-|z|^2/2}, \quad (3.69)$$

3.3 Diagonalisation of the Hamiltonian

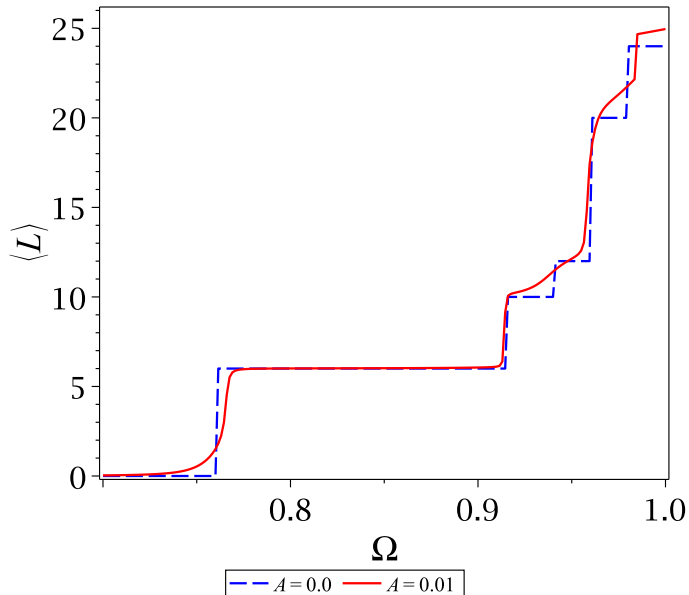


Figure 3.6: Average angular momentum profile of the ground state for $N = 6$ particles as a function of the rotation frequency and an interaction strength of $g = 1$. In the isotropic case ($A = 0$), it consists of a sequence of sharp jumps and plateaux corresponding to the energy crossings in the spectrum. On the other hand, when $A \neq 0$, the anisotropic term mixes a range of states having different values of the angular momentum; as a result the profile of the angular momentum becomes smooth. For this calculation, the lowest Landau level approximation was used, and the truncation of the basis is $L_{\max} = N + 10$. Had we taken a much larger cutoff for the angular momentum, more jumps would have been observed near the centrifugal limit ($\Omega \sim 1$), where the sequence of jumps and plateaux terminates at the maximum angular momentum $L = N(N - 2)$.

where $z_i = x_i + iy_i$, $z_c = \sum_{i=1}^N z_i/N$ and $|\mathbf{z}|^2 = \sum_{i=1}^N |z_i|^2$. The physical interpretation of this expression is that all the bosons are rotating around the center of mass (Wilkin *et al.*, 1998).

As it was mentioned before, as the rotation frequency increases, the ground state experiences a sequence of transitions to higher angular momentum states at critical values Ω_1, Ω_2 , etc. As a consequence, the angular momentum of the

3.3 Diagonalisation of the Hamiltonian

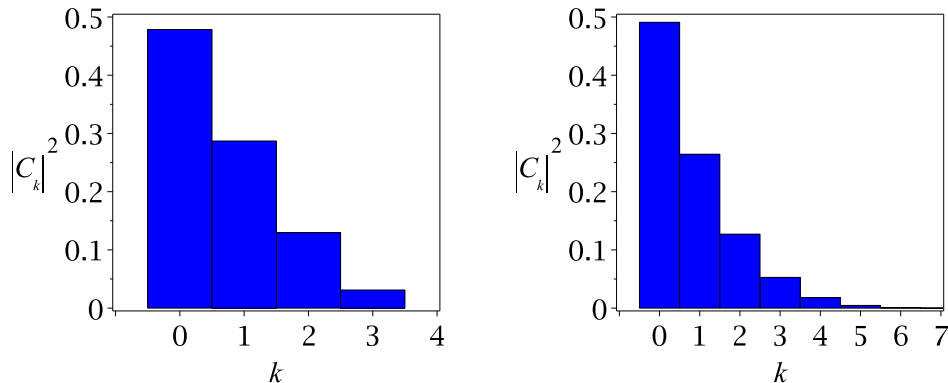


Figure 3.7: Analysis of the amplitudes of the coefficients $|C_k|^2$ for the single-vortex state at Ω_1 in the lowest Landau level approximation. The numbers of particles considered are $N = 6$ (left), and $N = 14$ (right). For both panels the truncation of the basis is $L_{\max} = N + 2$ and $g = 6/N$.

ground state shows sharp steps at these critical values, as can be seen in Fig. (3.6). Remarkably, this sequence of transitions terminates at the last possible value of $L = N(N - 1)$, corresponding to the Laughlin state, which has zero interaction energy and it is thus the lowest lying eigenstate of the many-body system at $\Omega \approx 1$.

We saw that the nucleation of the first vortex in an axisymmetric trap is a consequence of spontaneous symmetry breaking. Another different way of nucleating the vortex is by explicitly including a discrete parity symmetry breaking term $A \neq 0$ in the Hamiltonian. This approach has also been studied analytically (Fetter, 2010), numerically (Dagnino *et al.*, 2009a; Parke *et al.*, 2008) and experimentally (Chevy *et al.*, 2000; Gemelke & Chu, 2010). In the following section, we focus on the case $A \neq 0$ and give a review, as well as a presentation of the numeric results using our own codes.

3.3.2 The anisotropic case

In general terms, the inclusion of the anisotropic term $A \neq 0$ has the effect of lifting the remaining degeneracy and turning the energy crossings at $\Omega_1, \Omega_2, \dots$

3.3 Diagonalisation of the Hamiltonian

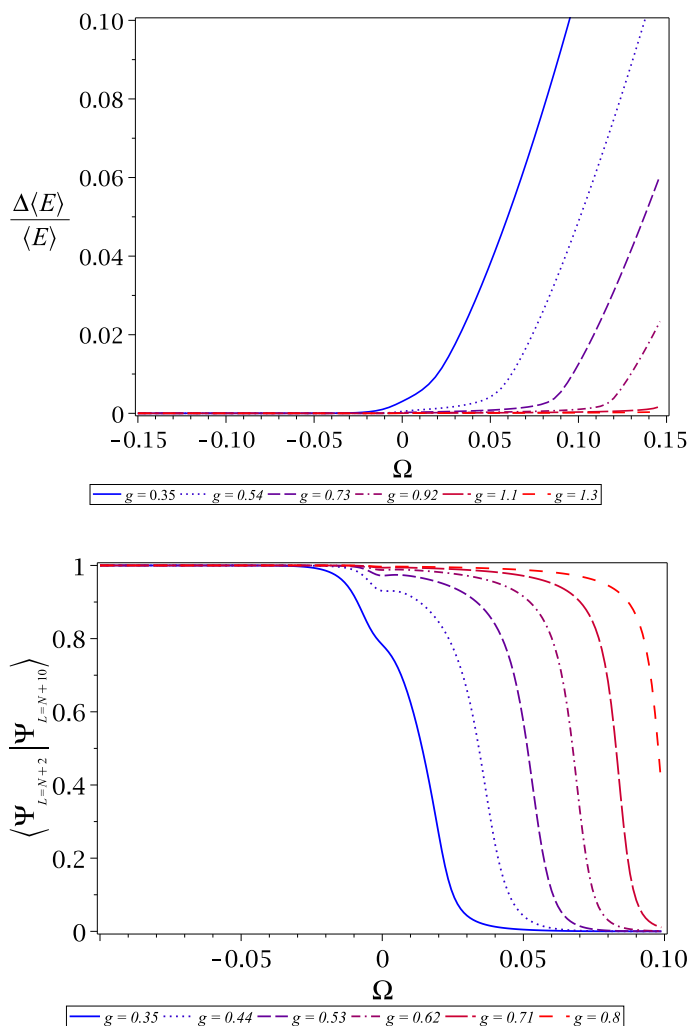


Figure 3.8: Analysis of the angular momentum basis truncation for $N = 6$ particles in the lowest Landau level approximation. (Top) The fractional error in the energy of the ground state as a function of the rotation rate centred at Ω_1 as calculated with a truncation of $L_{\max} = N + 10$. The fractional error is calculated as the difference in energy calculated with $L_{\max} = N + 10$ and $L_{\max} = N + 2$, divided by the energy of the ground state calculated with the largest basis. (Bottom) Overlap between the ground states calculated with the two different basis.

3.3 Diagonalisation of the Hamiltonian

into anticrossings at a slightly shifted rotation frequency. The rotation rate at which the first anticrossing occurs is referenced as Ω_{\min} . We discuss in this section the most important consequences of this degeneracy removal.

When $A \ll 1$, we can restrict the Hamiltonian to the subspaces of $L \leq L_{\max}$, choosing L_{\max} as the angular momentum cutoff for the basis truncation that ensures convergence of the energies and eigenstates. In what follows, we mostly consider a small fixed anisotropy of $A = 0.03$ throughout the calculations. This value allows for a relatively small cutoff of $L_{\max} = N + 2$, while providing accurate results for a wide range of values of the interaction strength. We show the fractional error in energy of the ground state as a function of Ω centred around the rotation frequency of the first avoided crossing in Fig. 3.8, as calculated with $L_{\max} = N + 2$ and $L_{\max} = N + 10$, for a range of values of the interaction strength. Also, the fidelity of the ground state in the $L_{\max} = N + 2$ basis with the $L_{\max} = N + 10$ basis is shown in the same figure. We find that the $L_{\max} = N + 2$ truncation gives accurate results for $gN \geq 6 \times 0.4$ for all the numbers of atoms that we were able to simulate. The decreasing fidelity when gN is less than this value is due to the fact that as g decreases, the first anticrossing occurs at rotation frequencies Ω_{\min} very close to 1 (the trap frequency), where the ground state is more sensitive to the inclusion of higher angular momentum states in a larger basis. Here, we have avoided values of $gN > 6$ because, as we shall see, we need to include higher Landau levels to correctly describe the ground state for these values of the interaction strength. Thus, we restrict ourselves to values of $A \leq 0.03$ and $6 > gN \geq 6 \times 0.4$ in order to use the $L_{\max} = N + 2$ basis.

As it was mentioned before, we shall be concerned about the first anticrossing at the threshold of the nucleation of the first vortex. Thus, we proceed to review the most important features of the condensate around this anticrossing.

First, a remark on the parity of the number of particles is in order. Since the ground state below and above Ω_1 for $A = 0$ has angular momentum $L = 0$ and $L = N$, respectively, we restrict ourselves to even numbers of particles; in that way, we can look for solutions to the eigenvalue problem in the basis consisting of only even angular momentum states. When N is odd, the single-vortex state has necessarily odd parity and thus a change of parity of the ground state occurs

3.3 Diagonalisation of the Hamiltonian

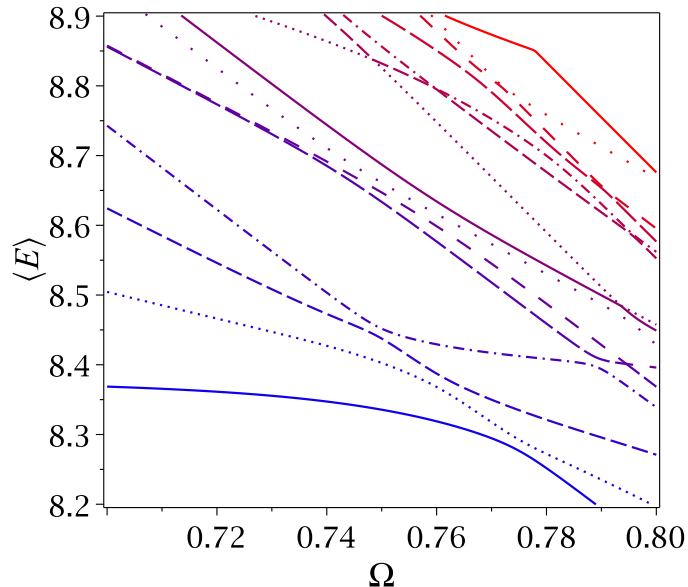


Figure 3.9: Energy spectrum for the case of $N = 6$ interacting particles in the anisotropic case ($A = 0.03$) as a function of the rotation frequency. The effect of the anisotropy is that of lifting the remaining degeneracy thereby creating energy anticrossings. The first anticrossing occurs at rotation frequency Ω_{\min} . The calculation is restricted to the lowest Landau level approximation, and the truncation of the basis is taken to be $L_{\max} = N + 2$.

from $L = 0$ to $L = N$ at Ω_1 . This is associated with a trivial residual first-order transition whose magnitude decreases as $N \rightarrow \infty$ (Parke *et al.*, 2008).

Exact calculation of the energy spectrum clearly shows the development of energy anticrossings in Fig. (3.9), particularly the first one at the threshold of the nucleation of the first vortex. Interestingly, the minimum energy gap between the ground state and the first excited state at Ω_{\min} is approximately constant for any value of the interaction strength in the range $0.44 \leq gN/6 \leq 1$, and it only depends on the magnitude of A . This feature can be observed in Fig. (3.10), where the size of the energy gap as a function of Ω centered around Ω_{\min} for a range of values of the interaction strength is plotted for $N = 6$ and $N = 12$.

The scaling of the minimum energy gap at Ω_{\min} with N is also remarkable.

3.3 Diagonalisation of the Hamiltonian

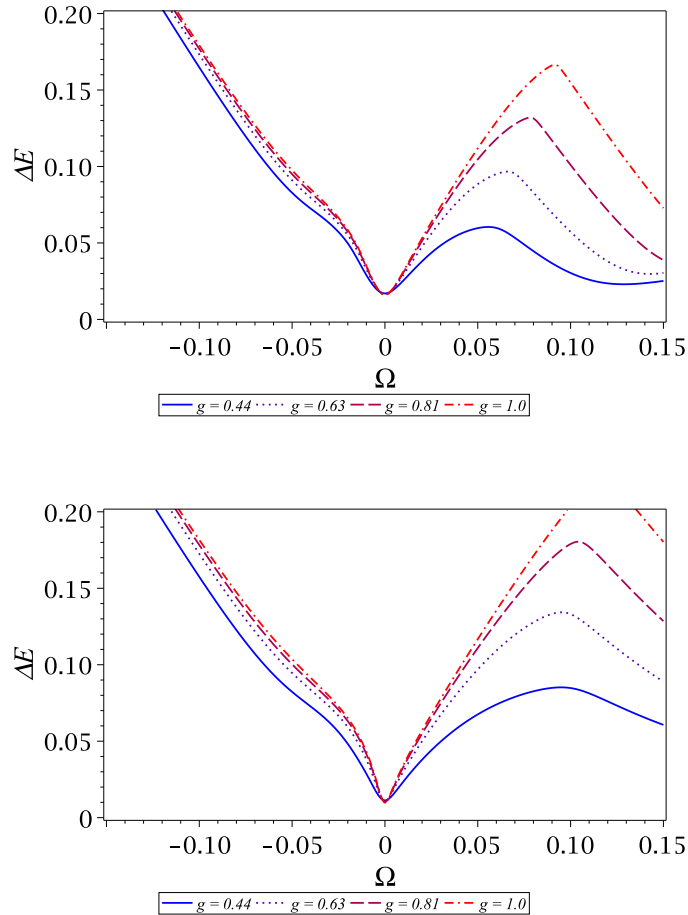


Figure 3.10: Energy gap between the ground state and the first excited state as a function of the rotation frequency for different values of the interaction strength for $N = 6$ (top) and $N = 12$ (bottom). For each particular value of g , the rotation frequency is measured from Ω_{\min} ; the plots have been shifted in order to emphasise this, and for better comparison purposes. The calculation is restricted to the lowest Landau level, and the basis truncation is $L_{\max} = N + 2$.

Although we have not been able to simulate systems with numbers of particles larger than $N > 16$, our results are in perfect agreement with those presented in (Dagnino *et al.*, 2009b), which show that ΔE tends to a small constant value $\Delta E \approx 0.7 \times 10^{-2}$ for large N as can be seen in Fig. (3.11). This is particularly

3.3 Diagonalisation of the Hamiltonian

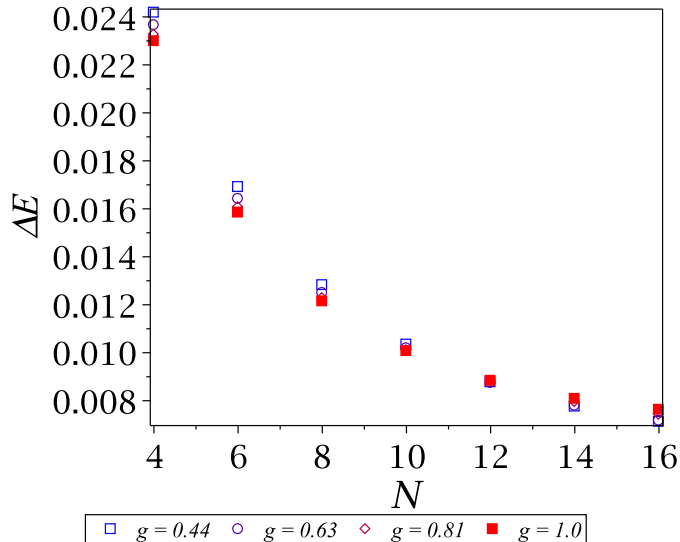


Figure 3.11: Minimal energy gap between the ground state and the first excited state at Ω_{\min} as a function of N for different values of the interaction strength. In all cases, the interaction strength was scaled for each value of N , and the scaled values of g shown in the plot are given by $gN/6$. The calculation is restricted to the lowest Landau level approximation, and the truncation of the basis is $L_{\max} = N + 6$ in order to have convergence for small values of g and large values of N .

promising for it allows the possibility of adiabatic nucleation of the first vortex even for large N . This adiabatic nucleation will be central in chapter 5, when we study an interferometric scheme that allows sub-shot noise precision using the rotating quantum gas. However, as (Dagnino *et al.*, 2009b) shows, if the system is not protected against parity breaking perturbations, which are perturbations connecting even and odd subspaces of angular momentum, the energy gap at the first avoided crossing vanishes for large numbers of particles, and thus limiting the adiabatic nucleation to numbers of atoms $N \approx 10$.

Due to the fact that, in the case of $A = 0$, all the yrast states for $2 \leq L \leq N$ are degenerate at Ω_1 , the inclusion of the anisotropic term has the effect of mixing these states according to their parity; as a result, the ground state at the avoided

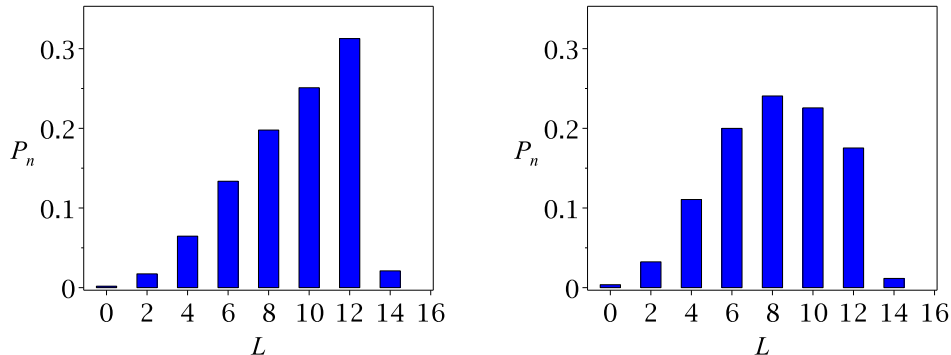


Figure 3.12: Weight of the angular momentum subspaces in the composition of the ground state for $N = 12$ particles and $g = 6/N$. (Left) Composition of the ground state at the rotation frequency Ω_{\min} . (Right) Composition of the ground state near the avoided crossing at rotation frequency $0.99\Omega_{\min}$. The calculation is restricted to the lowest Landau level approximation, and the truncation of the basis is $L_{\max} = N + 2$.

crossing Ω_{\min} has relatively large overlaps with even states of angular momentum up to $L = N$ as shown in Figs. (3.12) and (3.13). In fact, the largest overlap is the one with the single-vortex state of Eq. (3.68). Finally, the continuous character of the energy for the ground state is also reflected on the angular momentum profile which is shown in Fig. (3.6), where the sharp jumps and plateaux of the profile from the $A = 0$ case turn into a smooth curve.

Now, we follow (Dagnino *et al.*, 2009a) and introduce the single particle density matrix (SPDM). Calculation of this matrix and its eigenvalues is central to the determination of effects beyond mean-field theory, axisymmetry breaking (Ueda & Nakajima, 2006), off-diagonal long range order correlations (Yang, 1962), and the determination of the condensate wave function.

3.3.3 Single particle density matrix

In principle, the knowledge of the many-body density matrix allows one to calculate the mean value of any observable and encodes the maximum information available regarding the system. However, in practice only a limited number of

3.3 Diagonalisation of the Hamiltonian

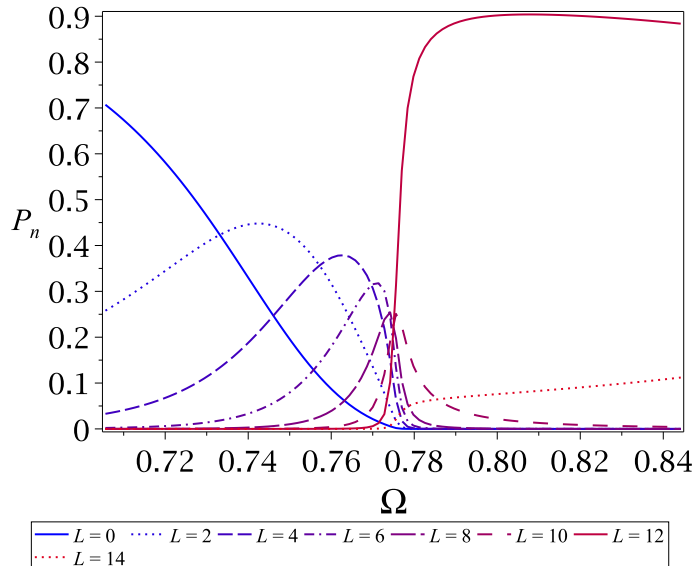


Figure 3.13: Weight of the angular momentum subspaces in the composition of the ground state for $N = 12$ particles and $g = 6/N$ as a function of the rotation frequency. The range of Ω is centred around the rotation frequency Ω_{\min} . The calculation is restricted to the lowest Landau level approximation, and the truncation of the basis is $L_{\max} = N + 2$.

observables are accessible during an experiment, such as spin of particles, kinetic energy, number of particles or interaction energy. The single particle density matrix (SPDM) has all the properties required to be considered a density matrix in single-particle space when normalised. Therefore, the sole knowledge of the SPDM suffices to predict the mean values of all the one-body observables, and hence its importance.

If ρ is the many-body density matrix of the system, the single-particle density matrix is defined as (Martin & Rothen, 2004)

$$\rho_{kl}^{(1)} = \langle k | \rho^{(1)} | l \rangle = \text{Tr} \left[\rho \hat{a}_k^\dagger \hat{a}_l \right], \quad (3.70)$$

where \hat{a}_k^\dagger and \hat{a}_l create and annihilate a boson in the single-particle level k and l , respectively. It can be shown that the SPDM is hermitian and its trace is equal

3.3 Diagonalisation of the Hamiltonian

to the mean number of bosons

$$\rho^{(1)} = (\rho^{(1)})^\dagger \quad \text{and} \quad \text{Tr} [\rho^{(1)}] = \langle \hat{N} \rangle, \quad (3.71)$$

where $\langle \hat{N} \rangle$ is given by the many-body mean value $\text{Tr} [\rho \hat{N}]$. The mean value of any one-body observable can be found using $\rho^{(1)}$

$$\langle \hat{A} \rangle = \text{Tr} \rho^{(1)} \hat{A}^{(1)}. \quad (3.72)$$

Here, $\hat{A}^{(1)}$ is a one-body observable operator in single-particle space. The diagonal elements of the SPDM $\rho_{kk}^{(1)}$ are, up to a factor of N , nothing but the probability of finding any of the particles in state k ; in other words

$$\rho_{kk}^{(1)} = \langle \hat{N}_k \rangle. \quad (3.73)$$

When the state of the many-body system is a pure state and thus the density matrix is given by $\rho = |\Psi\rangle\langle\Psi|$, the SPDM can be expressed as

$$\begin{aligned} \rho_{kl}^{(1)} &= \text{Tr} \left[|\Psi\rangle\langle\Psi| \hat{a}_l^\dagger \hat{a}_k \right] \\ &= \sum_i \langle \Psi_i | \Psi \rangle \langle \Psi | \hat{a}_l^\dagger \hat{a}_k | \Psi_i \rangle \\ &= \langle \Psi | \hat{a}_l^\dagger \hat{a}_k | \Psi \rangle. \end{aligned} \quad (3.74)$$

This last expression is very convenient for numeric calculations since it allows for a few different optimisations to reduce the number of its elements that need to be calculated. As an example of this, notice that due to the presence of \hat{a}_k , all the basis states that have no bosons occupying the single-particle orbital k have a vanishing contribution towards the SPDM. Likewise, due to the presence of \hat{a}_l^\dagger in the last expression, all the basis states having N bosons occupying the single-particle orbital l have a vanishing contribution to the SPDM when $k \neq l$. Also, since we work in a truncated basis in blocks of fixed total angular momentum, the restriction $0 \leq m_l + m_k \leq L_{\max}$ further reduces the number of calculations needed to determine the SPDM.

In coordinate representation, it can be shown (Martin & Rothen, 2004; Yang, 1962) that for non-interacting bosons in the limit of large volume

$$\langle \vec{\mathbf{x}}' | \rho^{(1)} | \vec{\mathbf{x}} \rangle \rightarrow \alpha N / \Delta V \quad \text{as} \quad |\vec{\mathbf{x}}' - \vec{\mathbf{x}}| \rightarrow \infty, \quad (3.75)$$

3.3 Diagonalisation of the Hamiltonian

where α is the finite fraction of the gas in the condensed state and ΔV is the volume occupied by the condensate. This is the off-diagonal long-range order which is a characteristic manifestation of the Bose–Einstein condensation. This long-range order in turn implies the existence of a large eigenvalue of the order of N for the SPDM, and vice versa. The notion of off-diagonal long-range order is not as relevant for trapped bosons, but the existence of a large eigenvalue is useful for defining the degree of condensation for interacting particles (for non-interacting particles the standard signature for Bose–Einstein condensation is the macroscopic population of the lowest single-particle level). Thus, the eigenfunction $\psi_1(\vec{\mathbf{x}})$ corresponding to the largest eigenvalue of the SPDM is the condensate wave function and its eigenvalue the condensed fraction (Penrose & Onsager, 1956).

In order to find the eigenvalues and eigenvectors of the SPDM, we need to diagonalise it. Since the SPDM is a hermitian matrix, it has real eigenvalues $\langle \hat{N}_k \rangle$ and orthogonal eigenvectors \mathbf{v}_k which satisfy

$$\rho^{(1)} \mathbf{v}_k = \langle \hat{N}_k \rangle \mathbf{v}_k. \quad (3.76)$$

If we write these orthonormal vectors as the columns of the matrix Q , then one can diagonalise the SPDM by means of a similarity transformation

$$\tilde{\rho}^{(1)} = Q^\dagger \rho^{(1)} Q, \quad (3.77)$$

where $[\tilde{\rho}^{(1)}]_{kl} = \langle \hat{N}_k \rangle \delta_{kl}$ is the diagonal SPDM after the transformation and the matrix Q is given by

$$[Q]_{kl} = [\mathbf{v}_l]_k. \quad (3.78)$$

Consequently, using (3.77), the SPDM can be written as

$$\begin{aligned} [\tilde{\rho}^{(1)}]_{\mu\nu} &= \sum_i [Q^\dagger]_{\mu i} \sum_j [\rho^{(1)}]_{ij} [Q]_{j\nu} \\ &= \sum_{ij} [Q^\dagger]_{\mu i} [Q]_{j\nu} \langle \Psi | \hat{a}_j^\dagger \hat{a}_i | \Psi \rangle \\ &= \langle \Psi | \left(\sum_j [Q]_{j\nu} \hat{a}_j^\dagger \right) \left(\sum_i [Q^\dagger]_{\mu i} \hat{a}_i \right) | \Psi \rangle. \end{aligned} \quad (3.79)$$

3.3 Diagonalisation of the Hamiltonian

As a result, a basis change for the creation and annihilation operators is induced. In fact, taking $[R]_{kl} = [Q]_{lk}$, this change of basis can be expressed as

$$\tilde{a}_\mu^\dagger = \sum_i [R]_{\mu i} \hat{a}_i^\dagger \quad \text{and} \quad \tilde{a}_\mu = \sum_i [R]_{\mu i}^* \hat{a}_i. \quad (3.80)$$

These expressions in turn imply the induced change of the single-particle angular momentum basis to the so-called natural orbitals basis

$$|\tilde{\psi}_l\rangle = \sum_k [R]_{lk} |\psi_k\rangle. \quad (3.81)$$

We have diagonalised the SPDM and plotted the three largest normalised eigenvalues of the SPDM as a function of Ω around the first avoided crossing in Fig. (3.14). These results indicate that most of the population of the SPDM around the first anticrossing is concentrated in the first two modes $\tilde{\psi}_1$ and $\tilde{\psi}_2$ in the natural basis, and they equalise at a critical frequency Ω_c . Below Ω_c , the most populated state $\tilde{\psi}_1$ is approximately a coherent superposition of two off-centred vortices with even parity corresponding to the superposition of the states with $m = 0$ and $m = 2$. On the other hand, $\tilde{\psi}_2$ is approximately given by a well-centred vortex single-particle state with odd parity corresponding to the state with $m = 1$. When $gN/6 = 1$, the actual composition of these states in the angular momentum basis for $N = 12$ is

$$\begin{aligned} \tilde{\psi}_1 &\approx -0.851\psi_{m=0} + 0.523\psi_{m=2}, \\ \tilde{\psi}_2 &\approx 0.999\psi_{m=1}. \end{aligned} \quad (3.82)$$

As g is decreased, a very tiny component of the states $\psi_{m=4}$ and $\psi_{m=3}$ appear in the composition of ψ_1 and ψ_2 , respectively, with equal probabilities of ~ 0.012 for $gN/6 = 0.4$. This is due to the increasing proximity of higher angular momentum states to the ground state when g decreases. Nevertheless, the parity of the two most populated states is conserved by the addition of these small components.

Above Ω_c , the two most populated states of the SPDM with opposite parities abruptly swap places resulting in an equally abrupt change in the macroscopic observable density, and thus heralds a quantum phase transition at the critical frequency as was first found by (Dagnino *et al.*, 2009a). One further consequence

3.3 Diagonalisation of the Hamiltonian

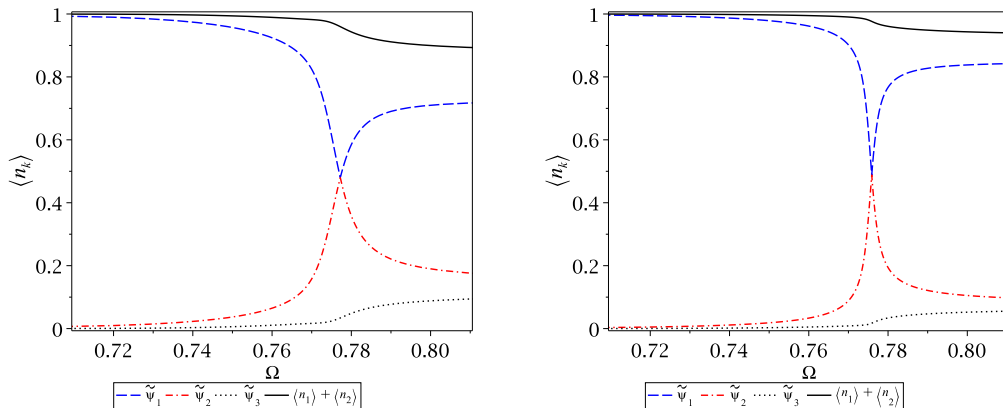


Figure 3.14: Normalised occupations for the three most populated single-particle states of the SPDM as a function of Ω near the critical frequency. (Left) Calculation for $N = 6$. (Right) Calculation for $N = 12$. The calculation is restricted to the lowest Landau level approximation, and the truncation of the basis is $L_{\max} = N + 2$.

of this abrupt change is the fact that the state of the system at the critical frequency cannot be described by a mean-field theory since $\tilde{\psi}_1$ and $\tilde{\psi}_2$ have equal populations at this rotation frequency, whereas the mean-field prescription requires the SPDM to have a single large eigenvalue close to N .

Although the actual value of the critical frequency Ω_c depends on the magnitude of the interaction strength, we have verified that for fixed N , the eigenvalues and eigenvectors of the SPDM are approximately the same near criticality for values of the interaction strength in the range $0.4 \leq gN/6 \leq 1.0$. As N increases, the condensation above Ω_c increases, and the populations of the two most populated states at Ω_c get closer to 0.5. These results have important consequences for the actual form of the ground state at the critical rotation. In the following section, we study the ground state and its correlations in more detail.

3.4 The many-body ground state at criticality

The fact that the SPDM has two large eigenvalues which account for most of the population near Ω_c , suggests that the many-body ground state can be approximated by a superposition of two-mode states in which only the single-particle orbitals $\tilde{\psi}_1$ and $\tilde{\psi}_2$ are occupied. In order to prove this, we define a two-mode many-body state as

$$|N_1, N_2\rangle = \frac{\left(\tilde{a}_1^\dagger(\Omega)\right)^{N_1}}{\sqrt{N_1!}} \frac{\left(\tilde{a}_2^\dagger(\Omega)\right)^{N_2}}{\sqrt{N_2!}} |0\rangle, \quad (3.83)$$

where $\tilde{a}_1^\dagger(\Omega)$ ($\tilde{a}_2^\dagger(\Omega)$) creates a boson in the orbital corresponding to the most (second most) populated single-particle state at Ω , given by the eigenvectors of the SPDM. These creation operators can be expressed in terms of the ones in the angular momentum basis using the transformations in Eq.(3.80), giving

$$|N_1, N_2\rangle = \frac{\left(\sum Q_{m1} a_m^\dagger\right)^{N_1}}{\sqrt{N_1!}} \frac{\left(\sum Q_{m2} a_m^\dagger\right)^{N_2}}{\sqrt{N_2!}} |0\rangle, \quad (3.84)$$

where we have dropped the Ω functional dependence for brevity purposes.

Consequently, the two-mode components of the ground state are given by

$$\begin{aligned} \langle N_1, N_2 | \Psi_0 \rangle &= \langle N_1, N_2 | \sum_l \langle \Phi_l | \Psi_0 \rangle | \Phi_l \rangle \\ &= \sum_l \langle \Phi_l | \Psi_0 \rangle \langle N_1, N_2 | \Phi_l \rangle, \end{aligned} \quad (3.85)$$

where $\langle N_1, N_2 | \Phi_l \rangle$ can be numerically evaluated using Eq.(3.84). Since right below Ω_c , the most populated state is a coherent superposition of states with $m = 0$ and $m = 2$, so will be its corresponding creation operator. Likewise, the second most populated state is the state with $m = 1$ and its corresponding creation operator has the effect of creating a boson in the single-particle state $m = 1$. As a consequence, the overlap $\langle N_1, N_2 | \Phi_l \rangle$ vanishes when N_1 and N_2 are odd numbers since the resulting state of Eq.(3.84) in the angular momentum basis has odd angular momentum and thus it is outside the basis we are using (even angular momentum states). The same argument applies right above Ω_c .

3.4 The many-body ground state at criticality

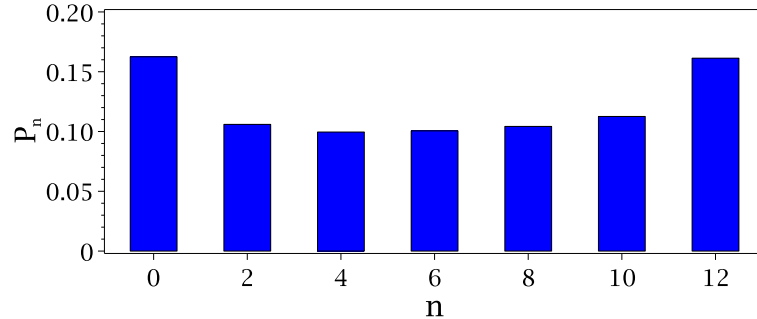


Figure 3.15: The coefficients $P_n = |\langle N - 2n, 2n | \Psi_0(\Omega_c) \rangle|^2$ for the two-mode approximation at the critical frequency. The fidelity of the two-mode approximation is found to be $|\langle \Psi_0(\Omega_c) | \Psi_{\text{TM}} \rangle|^2 = 0.83$. The calculation is restricted to the lowest Landau level approximation, and the truncation of the basis is $L_{\text{max}} = N + 2$. (Taken from (Rico-Gutierrez *et al.*, 2013))

Numerical calculations of the two-mode components of the ground state show that it is well approximated by a two-mode superposition at the critical frequency given by

$$|\Psi_0(\Omega_c)\rangle \approx |\Psi_{\text{TM}}\rangle = \sum_n C_n |N - 2n, 2n\rangle. \quad (3.86)$$

We found that the fidelity of the two-mode approximation is typically ~ 0.8 for all $N \leq 20$ in the lowest Landau level approximation. The actual values of $P_n = |C_n|^2$ for $N = 12$ are plotted in Fig. (3.15). Interestingly, the state has a bat-like structure much like the bat states that we introduced in chapter 2; therefore, we expect this ground state to perform well in quantum metrology schemes because of its entanglement and the natural robustness against losses that it possesses. That the ground state at Ω_c is actually highly entangled can be shown using Zanardi's concept of mode entanglement (Zanardi, 2001); tracing the two-mode state over one of the modes gives a von Neumann entropy of the reduced density matrix that nearly reaches the maximal value $S \sim \log(N)$ (Dagnino *et al.*, 2009a).

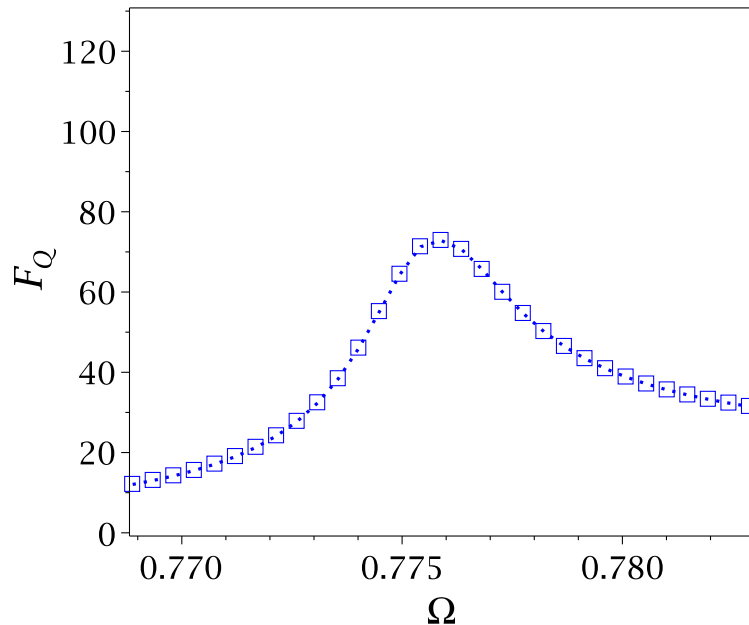


Figure 3.16: Fisher information for the ground state as a function of the rotation rate for $N = 12$ particles, calculated for the most populated mode of the SPDM at each value of Ω . The interaction strength is $g = 6/N$ and $A = 0.03$, which results in a critical frequency of $\Omega_c \approx 0.776$. Also, the calculation was restricted to the LLL approximation and $L_{\max} = N + 2$. (Taken from (Rico-Gutierrez *et al.*, 2013))

3.4.1 Fisher information of the ground state

Now, we proceed to calculate the quantum Fisher information for the entangled state at Ω_c in order to quantify how well the state performs in linear interferometric schemes.

Since we are dealing with a pure state of the condensate at $T = 0$, the Fisher information can be calculated using

$$F_Q[|\Psi(\phi)\rangle] = 4 \left[\langle \Psi'(\phi) | \Psi'(\phi) \rangle - |\langle \Psi'(\phi) | \Psi(\phi) \rangle|^2 \right], \quad (3.87)$$

where $|\Psi'(\phi)\rangle = \partial|\Psi(\phi)\rangle/\partial\phi$.

Suppose that the entangled ground state at Ω_c picks up an undetermined linear phase as a result of some dynamical evolution corresponding to a unitary

3.4 The many-body ground state at criticality

operation $U(\phi)$ being applied to the first mode, corresponding to the most populated eigenstate of the SPDM. Therefore, the resulting state in the two-mode approximation is

$$U(\phi)|\Psi_{\text{TM}}\rangle = \sum_{n=0}^{N/2} C_n e^{i\phi(N-2n)} |N-2n, 2n\rangle. \quad (3.88)$$

The best precision, $\Delta\phi$, with which the phase can be measured using this state in a single shot experiment, independent of the measurement scheme is given by the quantum Cramér-Rao bound

$$\Delta\phi \geq \frac{1}{\sqrt{F_Q}}. \quad (3.89)$$

Since the fidelity of the two-mode state is ~ 0.8 , we rather consider a multi-mode expansion of the ground state in order to obtain accurate results for the Fisher information. In doing this, we define a d -mode state as

$$|\tilde{\Psi}_l\rangle = |\tilde{N}_1(l), \tilde{N}_2(l), \dots, \tilde{N}_d(l)\rangle, \quad (3.90)$$

where $\tilde{N}_k(l)$ corresponds to the number of atoms occupying the k -th most populated eigenstate of the SPDM, and l is a special index that labels the multi-mode state and uniquely determines the distribution of the N bosons over the d modes. Consequently, we can generalise Eq.(3.88) as

$$|\Psi_0(\phi)\rangle = U(\phi)|\Psi_0(\Omega_c)\rangle = \sum_l C_l e^{i\tilde{N}_1(l)\phi} |\tilde{\Psi}_l\rangle. \quad (3.91)$$

Calculation of the derivative of this state readily gives

$$|\Psi'_0(\phi)\rangle = \sum_l iC_l \tilde{N}_1(l) e^{i\tilde{N}_1(l)\phi} |\tilde{\Psi}_l\rangle. \quad (3.92)$$

Therefore, we have

$$\begin{aligned} \langle\Psi'_0(\phi)|\Psi'_0(\phi)\rangle &= \sum_{s,l} \left[-iC_s^* \tilde{N}_1(s) e^{-i\tilde{N}_1(s)\phi} \right] \left[iC_l \tilde{N}_1(l) e^{i\tilde{N}_1(l)\phi} \right] \langle\tilde{\Psi}_s|\tilde{\Psi}_l\rangle \\ &= \sum_l |C_l|^2 \tilde{N}_1^2(l) \\ &= \langle\Psi_0(\phi)|\hat{N}_1^2|\Psi_0(\phi)\rangle, \end{aligned} \quad (3.93)$$

3.4 The many-body ground state at criticality

where \hat{N}_k^2 is the number operator corresponding to the k -th most populated mode, and we have used the fact that $\langle \tilde{\Psi}_s | \tilde{\Psi}_l \rangle = \delta_{s,l}$, since the eigenstates of the SPDM are orthogonal and so are the multimode many-body states constructed from them. Likewise, the second term of the Fisher information in Eq.(3.87) can be expressed as

$$|\langle \Psi'_0(\phi) | \Psi_0(\phi) \rangle|^2 = \left(\langle \Psi_0(\phi) | \hat{N}_1 | \Psi_0(\phi) \rangle \right)^2. \quad (3.94)$$

Therefore, the quantum Fisher information for the entangled state after a linear phase has been applied to the first mode is given by

$$F_Q [|\Psi_0(\phi)\rangle] = 4 \left[\langle \hat{N}_1^2 \rangle - \langle \hat{N}_1 \rangle^2 \right]. \quad (3.95)$$

In numeric calculations, we evaluate the last expression expanding the number operator in the angular momentum basis as

$$\hat{N}_1 = \hat{a}_1^\dagger \hat{a}_1 = \sum_m Q_{m1} \hat{a}_m^\dagger \sum_{m'} Q_{m'1} \hat{a}_{m'}. \quad (3.96)$$

The number of modes taken into account in the Q matrix is determined by the numeric convergence of the Fisher information.

We show the numeric results of the Fisher information for the ground state near criticality in Fig. (3.16) using Eq.(3.95). Remarkably, the maximum value of F_Q and the width of the curve do not change when the interaction strength varies, under the LLL approximation. This suggests that the resulting entanglement is mostly due to the anisotropy of the trap alone, which differs in nature with other entanglement creation schemes using BECs, where the interactions are responsible for the creation of a $N00N$ state (Nunnenkamp *et al.*, 2008).

These results are promising for experimental implementations since the margin of error in Ω when trying to prepare the initial entangled state is comparable to the typical control precision in rotating traps of $\sim 1\%$ (Chevy *et al.*, 2000).

Finally, we saw in chapter 2 that the phase precision for a pure bat state scales with the number of atoms as $\sqrt{2}/\sqrt{N(N+2)}$. Comparatively, our bat-like state nearly saturates this precision, as can be seen in Fig. (3.17). Also, since the Fisher information at the critical frequency is independent of the interaction strength, the same is true for its scaling with N .

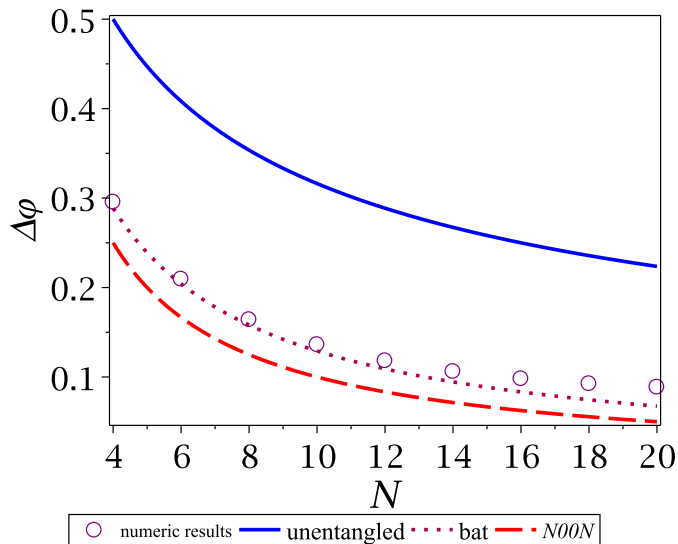


Figure 3.17: Phase precision for the entangled ground state at Ω_c as a function of N . The interaction strength is $g = 6/N$ and $A = 0.03$ for all cases. We plot the phase precision for the $N00N$ state $1/N$, bat state $\sqrt{2}/\sqrt{N(N+2)}$, and unentangled particles $1/\sqrt{N}$ for comparison purposes. All the calculations were restricted to the LLL approximation and $L_{\max} = N + 2$.

3.5 Conclusions

We have studied and reviewed the physics of a two-dimensional Bose–Einstein condensate in a rotating anisotropic quadratic trap whose strength is measured by the coefficient A , and contact interactions for which the strength is measured by the constant g . When the rotating trap has no anisotropy, the ground state of the system for small rotation frequencies $\Omega \sim 0$ is the non-rotating many-body state having all bosons in the single-particle state with angular momentum $m = 0$. As the rotation frequency is increased, the ground state remains in this non-rotating state with $L = 0$, up to a frequency Ω_1 where the stationary ground state makes a sharp transition to the single-vortex state, acquiring angular momentum $L = N$. This transition occurs at a rotation frequency for which all the lowest lying states with angular momentum $0 < L \leq N$ with $L \neq 1$ are degenerate. The inclusion of a small anisotropic term $A \neq 0$ has the effect of lifting

the degeneracy at this rotation frequency, thereby creating an avoided energy crossing. As a result, a critical frequency Ω_c exists near the avoided crossing for which the single particle density matrix (SPDM) has two large eigenvalues with equal populations $\langle n_1 \rangle = \langle n_2 \rangle$ and $\langle n_1 \rangle + \langle n_2 \rangle \approx 1$. These eigenvalues correspond to eigenfunctions of opposite angular momentum parities, having off-centred and well-centred vortices respectively. The two eigenfunctions abruptly swap places above the critical frequency, heralding a failure of the mean-field theory. In addition, since the system always remains in the ground state as Ω is increased, the gas must experience a sudden macroscopic symmetry change which is a signature of a quantum phase transition at the critical rotation frequency.

The ground state at criticality can be very well approximated by a two-mode state whose two modes correspond to the above-mentioned most populated states of the SPDM at Ω_c . This approximation shows that the ground state is highly entangled and has a bat-like form which is independent of the interaction strength between the atoms in the lowest Landau level approximation. Therefore, as we saw in chapter 2, this entangled state could be used in interferometric schemes to perform measurements with precision that scales better than the shot-noise, particularly for the current case of determining angular rotation rates, and also have the added feature of robustness against particle losses (Dubetsky & Kasevich, 2006; Dunningham & Hallwood, 2006). In order to assess the suitability of this state for quantum metrology, we calculated the quantum Fisher information for a linear phase accumulation in one of the modes (Rico-Gutierrez *et al.*, 2013). The results show that the Fisher information is nearly equal to the value obtained with a conventional bat state $F_Q \approx N(N + 2)/2$, even when the fidelity of the two-mode approximation is ~ 0.8 . In addition, the Fisher information remains much larger than N (sub-shot noise behavior) for a broad range of rotation frequencies centred around Ω_c . This is very promising for practical implementations since it means that experimentalists would have a sizable margin of error in order to nucleate the entangled state.

Chapter 4

Engineering entanglement with rotating matter waves

We saw in the previous chapter that a lowest Landau level (LLL) calculation predicts the existence of a critical rotation frequency Ω_c at the threshold of the nucleation of the first vortex for which the many-body ground state exhibits strong correlations as well as entanglement, and it is well described by an effective two-mode model; this constitutes an example of symmetry breaking in quantum many-body systems, first considered by (Dagnino *et al.*, 2009a). The LLL approximation allows for a simplified and more computationally tractable description of the system but it is only valid in the weakly interacting regime for which the particle density is low, the interaction strength is small or the rotation frequency is very close to the harmonic trap frequency. In fact, the LLL approximation has been very successful in describing the interesting case of fast rotating Bose gases, where typically $\Omega \sim 0.99$, and the angular momentum is $L \sim N^2$. In this regime of very fast rotation, the system is a strongly correlated quantum liquid such as the Pfaffian or Laughlin state, analogous to those appearing in the fractional quantum Hall effect. In our case of moderate rotation frequencies, we find that the LLL approximation predicts the critical frequency with great accuracy of the order of a few percent; this could give the wrong impression that the LLL approximation correctly describes all the features of the system. However, we have performed a more detailed investigation which has revealed that this is not true in general (Rico-Gutierrez *et al.*, 2013). When the interaction

4.1 Tuning entanglement in the rotating trap

strength is of the order of $gN \sim 6$, for example, the exact many-body ground state at Ω_c and the quantum Fisher information F_Q are significantly different for an approximation that goes beyond the LLL one, which is in principle more accurate.

Therefore, while the LLL approximation gives a good description of the system for the study of symmetry breaking (Dagnino *et al.*, 2009a) accurately predicts the rotation frequency at which the first vortex penetrates the condensate, a larger many-body basis must be considered when one is interested in the precise details of the entangled state. This issues a warning about the validity of the LLL approximation, particularly as a guide for designing experiments. In this chapter, we consider a more detailed study of the rotating anisotropic trap using a two and three Landau level calculation as it appears in (Rico-Gutierrez *et al.*, 2013), revealing a rich system that offers the possibility of engineering different entangled states. In particular, we are able to identify a parameter regime for generating bat-like states like the ones predicted by the LLL calculation, but also, we find another regime for generating $N00N$ -like states, a feature that the LLL approximation is unable to capture. Also, we assess the validity of the LLL for a different number of relevant physical magnitudes such as the critical frequency, the populations of the single-particle orbitals, and the energy gap between the many-body ground state and the first excited state, among others.

4.1 Tuning entanglement in the rotating trap

We saw in chapter 3 that, within the lowest Landau level (LLL) approximation, the stirring of a BEC with an anisotropic potential up to a critical rotation near the first energy anticrossing has the effect of nucleating a highly entangled bat-like ground state which is very well approximated by a two-mode state

$$|\Psi_0(\Omega_c)\rangle = \sum_{k=0}^{N/2} |N - 2k, 2k\rangle. \quad (4.1)$$

Although Eq.(4.1) can achieve nearly Heisenberg-limited precision for a linear phase accumulation, it does not fully saturate the Heisenberg limit, as the celebrated “cat” state does. Therefore, it is interesting to investigate the possibility

4.1 Tuning entanglement in the rotating trap

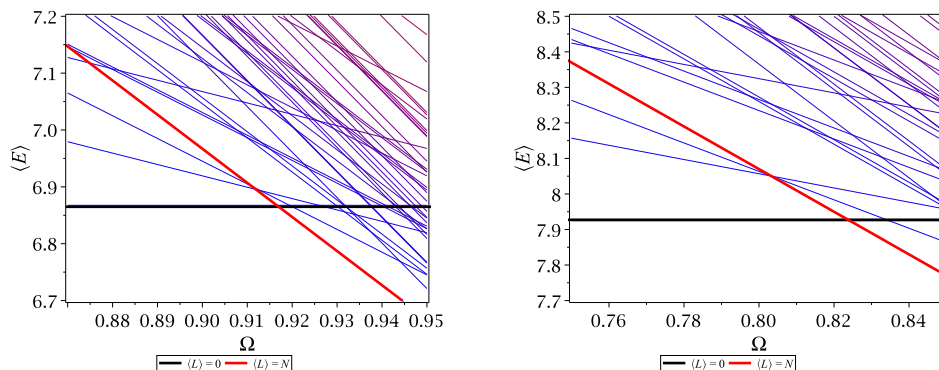


Figure 4.1: Energy spectrum as a function of the rotation frequency for $N = 6$ particles as calculated with a two Landau level approximation. (Left) weak interacting system where the interaction strength is given by $gN/6 = 0.4$. (Right) stronger interacting system with $gN/6 = 1$. The anisotropy is $A = 0.03$ and $L_{\max} = N + 2$ for both panels. The highlighted horizontal line corresponds to $\langle L \rangle = 0$ and the diagonal one to $\langle L \rangle = N$.

of creating a cat state, since this state is closely related to the state in Eq.(4.1). In fact, when $C_k = 0$ for $k = 1 \dots (N + 2)/2$, the bat-like state becomes a cat state. Therefore, if we find a mechanism to decouple the states $|N - 2k, 2k\rangle$ with $k = 1 \dots (N + 2)/2$ from the ground state, we might be able to create a $N00N$ state. The situation resembles that of an array of Bose-Einstein condensates trapped in optical potentials coupled to one another to form a ring (Hallwood *et al.*, 2006), where the ground state of non-interacting particles in this ring configuration has multiple crossings at a particular rotation rate. The degenerate states at the crossing include the $|N, 0\rangle$ and $|0, N\rangle$ states, where the two modes correspond to zero flow and one unit of clockwise flow, respectively, but multiple flow states (states having particles spread out in different flow modes) are also present at the crossing. Then, inclusion of interactions between the atoms leads to different energy shifts for all these states, where the multiple flow states acquire larger shifts than the single flow ones. As a result, the multiple flow states decouple from the ground state, leaving only a crossing of the states $|N, 0\rangle$ and $|0, N\rangle$. Then, a perturbation is added in order to create an anticrossing, for which the resulting ground state is a coherent $N00N$ superposition of the single flow

4.1 Tuning entanglement in the rotating trap

states. This suggests that we could increase the interaction strength between atoms in our system in order to decouple the “multiple parity” states in Eq.(4.1).

Recall that when $A = 0$, the first energy crossing is $(N/2 + 1)$ -fold degenerate at $\Omega_1 = 1 - gN/(8\pi)$, where all the yrast states for $0 \leq L \leq N$ with $L \neq 1$, have the same energy, and the addition of a small anisotropic perturbation $A \neq 0$ lifts the degeneracy and couples all of these states to the ground state at Ω_c . Therefore, in order to produce a cat state, we need to lift the degeneracy of these states in such a way that we obtain $C_k = 0$ for $k = 1 \dots (N + 2)/2$. However, the degeneracy of the ground state at Ω_1 remains exactly the same no matter how large g is. This is an artifact of the LLL approximation, for which the entire energy spectrum is invariant up to an overall scale factor under changes in the interaction strength (Morris & Feder, 2006). The LLL approximation is simply unable to capture any decoupling of the lowest angular momentum yrast states at Ω_1 due to the strengthening of interactions. Nevertheless, this is not a fundamental limitation of the system. In fact, it is known that when more Landau levels are taken into account in calculations, for fixed g and Ω , the energy shift of low-angular-momentum yrast states due to the inclusion of more Landau levels scales as $\propto L^{-|a|}$, where $|a|$ is a constant of order unity for small numbers of particles, which increases with N (Morris & Feder, 2006). This means that we necessarily need to go beyond the lowest Landau level approximation if we want to decouple the “multiple parity” states from the ground state by varying the interaction strength.

We show the energy spectrum near Ω_1 for $A = 0$ and $N = 6$ particles using two Landau levels in Fig. (4.1), where the differential energy shift for the low-angular-momentum yrast states is observed. The differential shift is even more noticeable as N increases for the same gN , as can be seen in Fig. (4.2).

When two Landau levels are considered, we observe striking differences in the way that the low-angular-momentum yrast states couple to the ground state, even for values of $gN \approx 6$, which according to Eq.(3.59) pertains to the LLL approximation at $\Omega_1 \approx 0.7$. As an example of this, the weights of the subspaces of fixed angular momentum for that participate in the GS at Ω_c when $A = 0.03$ are plotted in Fig. (4.3). Notice how the two Landau level calculation for $gN = 6$ is in sharp contrast with that obtained with the LLL approximation in Fig. (3.12).

4.1 Tuning entanglement in the rotating trap

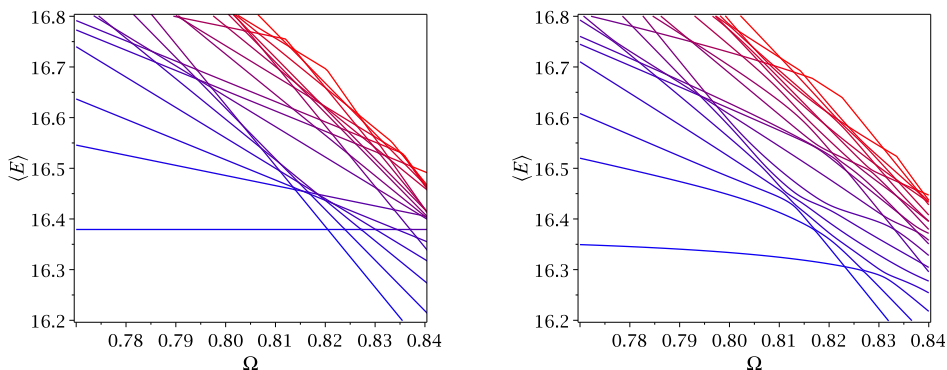


Figure 4.2: Energy spectrum as a function of the rotation frequency for $N = 12$ particles as calculated with a two Landau level approximation. (Left) Energy spectrum for the axisymmetric case ($A = 0$). (Right) The strength of the anisotropy is $A = 0.03$. The interaction strength is given by $gN/6 = 1$ for both panels, and $L_{\max} = N + 2$.

Equally striking is the behavior of the most populated eigenvalues of the single particle density matrix (SPDM) as a function of the rotation frequency shown in Fig. (4.4), when compared to Fig. (3.14). Although the behavior is qualitatively the same, i.e. that of two large modes dominating the composition of the ground state near the first anticrossing which equalise at the critical frequency Ω_c , the transition is extremely more abrupt for $gN \approx 6$. This is a general feature for all the numbers of atoms $N \leq 14$ that we were able to check. The actual composition of the two most populated states also shows some differences. For $N = 12$ and $gN = 6$, the composition of these states right below Ω_c is

$$\begin{aligned}\tilde{\psi}_1 &\approx 0.948\psi_{(0,0)} - 0.293\psi_{(0,2)} - 0.104\psi_{(1,1)}, \\ \tilde{\psi}_2 &\approx 0.995\psi_{(0,1)},\end{aligned}\tag{4.2}$$

where the notation (n, m) specifies the radial quantum number and the angular momentum one.

When we calculate the two-mode approximation for the ground state using two Landau levels, we obtain the results plotted in the bottom panel of Fig. (4.6). It is clear that going beyond the LLL approximation allows for the “multiple

4.1 Tuning entanglement in the rotating trap

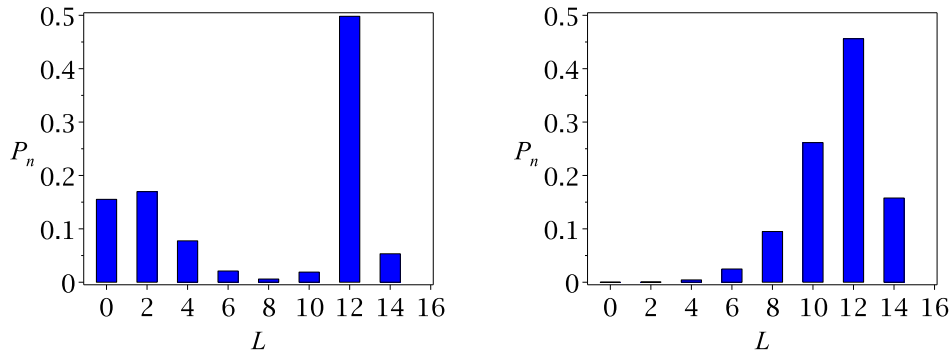


Figure 4.3: Weight of the angular momentum subspaces in the composition of the ground state at Ω_c for $N = 12$ using a two Landau level approximation and $A = 0.03$. (Left) Composition of the ground state for $gN/6 = 1$. (Right) Composition of the ground state for $gN/6 = 0.4$. The truncation of the basis is $L_{\max} = N + 2$ for both panels.

parity” states to drift away from the ground state, resulting in the production of a cat-like state, just as in the case of the rotating ring geometry discussed above.

The fact that the increase of the interaction strength has lifted the degeneracy at Ω_1 , thereby weakening the coupling of “multiple parity” states via the anisotropic term, suggests that the converse procedure should allow to couple these states back into the ground state. In fact, this is true. We show the two-mode approximation for the ground state and the eigenvalue decomposition of the SPDM for a reduced interaction strength of $gN/6 = 0.4$ for $N = 12$ particles in the top panel of Fig. (4.6). Notably, for a fixed value of $A = 0.03$, if we decrease g much below $gN = 6$, we recover the LLL regime, obtaining similar results as those presented in chapter 3, i.e. a bat-like state, and a less sudden quantum phase transition.

These findings are very promising for quantum metrology, since they mean that we can use this rotating condensate to create entangled states which can be tuned from $N00N$ -like states to bat-like ones by only changing the interaction strength, which in experiments is achieved through the use of Feshbach resonances (Cornish *et al.*, 2000). Alternatively, following the same line of thought, for fixed g , we could vary the strength of the anisotropy A in order to reduce or increase

4.1 Tuning entanglement in the rotating trap

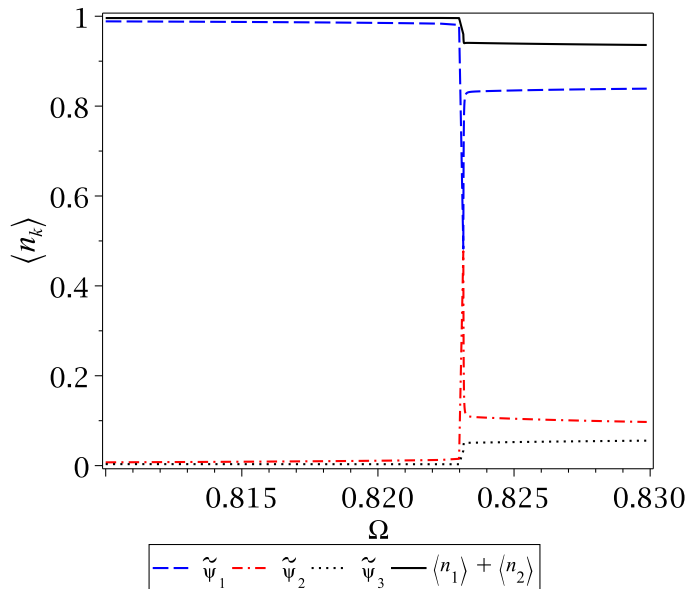


Figure 4.4: Normalised occupations for the three most populated single-particle states of the SPDM as a function of Ω near the critical frequency using two Landau levels for $N = 12$. The interaction strength is given by $gN/6 = 1$, the anisotropy strength is $A = 0.03$, and the truncation of the basis is $L_{\max} = N + 2$.

the coupling of the “multiple parity” states to the ground state. We plot the form of the entangled ground state produced for an increased $A = 0.05$ when $gN/6 = 1$, and the ground state form for a decreased $A = 0.005$ when $gN/6 = 0.4$ in Fig. (4.7). We have effectively swapped the shapes of the ground state shown in Fig. (4.6) for the same values of g by only changing A . In actuality, we can see that the coefficients for the “multiple parity” states are slightly different in both cases, resulting in the bat state from Fig. (4.7) resembling more closely the pure bat state that we introduced in chapter 2. These results show that it is in fact also possible to further tune entanglement in this system by varying the shape of the rotating trap. In this thesis, however, we focus on the case of tuning entanglement by only changing the interaction strength between atoms. This is partly due to the fact that proper accounting of large A needs a larger L_{\max} cutoff, thereby requiring more computational power to analyse the system.

4.1 Tuning entanglement in the rotating trap

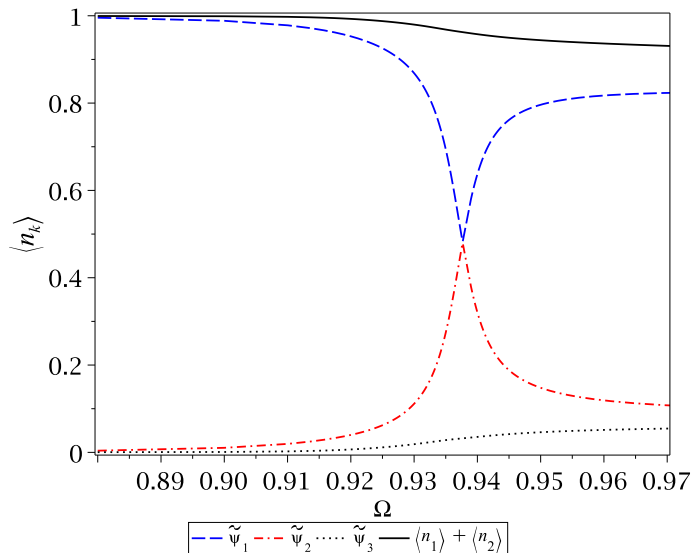


Figure 4.5: Normalised occupations for the three most populated single-particle states of the SPDM as a function of Ω near the critical frequency using two Landau levels for $N = 12$ particles. The interaction strength is given by $gN/6 = 0.4$, the anisotropy strength is $A = 0.03$, and the truncation of the basis is $L_{\max} = N + 2$.

One fundamental consequence of these results is that within the two Landau level framework, even for very small values of $gN \ll 6$, which in principle should be very well described by the LLL approximation, we can decrease A to the point of obtaining a cat-like state which is in remarkable disagreement with the bat-like state that invariably results using the LLL approximation. In practice, however, there is a limit on how small A can be reduced, due to the fact that a real trap always has a residual anisotropy of order $A \sim 1 \times 10^{-3}$ (Bretin *et al.*, 2004; Chevy *et al.*, 2000).

Finally, another physical quantity that experiences major changes when two Landau levels are considered is the minimal energy gap between the ground state and the first excited state at the first anticrossing. As might be suspected, the energy gap is no longer independent of the interaction strength, and it is in general larger for smaller values of the interaction strength g . However, even for

4.1 Tuning entanglement in the rotating trap

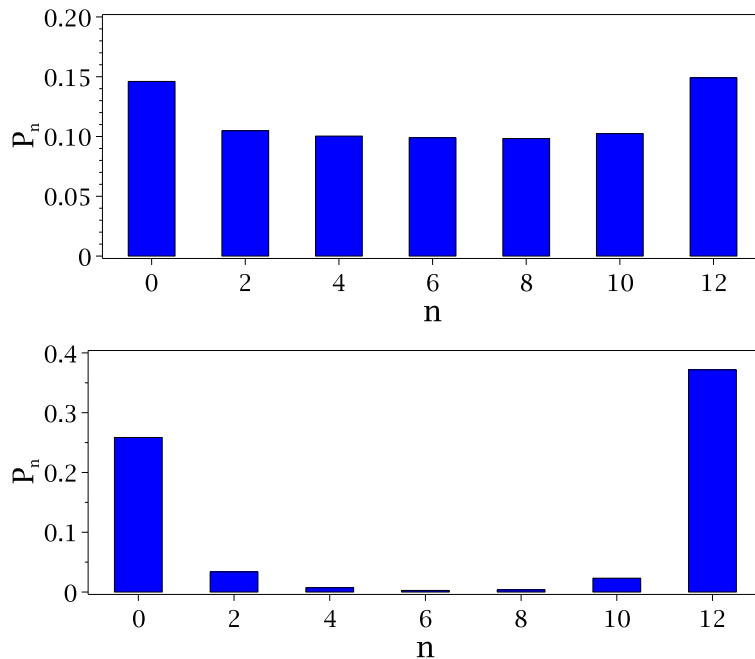


Figure 4.6: The coefficients $P_n = |\langle N - 2n, 2n | \Psi_0(\Omega_c) \rangle|^2$ for the two-mode approximation at the critical frequency using two Landau levels for $N = 12$ particles. (Top) For this bat-like state the interaction strength is given by $gN/6 = 0.4$, and the fidelity of the two-mode approximation is $|\langle \Psi_0(\Omega_c) | \Psi_{\text{TM}} \rangle|^2 = 0.80$. Also, the calculated critical frequency is $\Omega_c \approx 0.938$. (Bottom) For the cat-like state, the interaction strength is $gN/6 = 1$, and the fidelity of the two-mode approximation is $|\langle \Psi_0(\Omega_c) | \Psi_{\text{TM}} \rangle|^2 = 0.70$. The critical frequency in this case is $\Omega_c \approx 0.823$. The strength of the anisotropy is $A = 0.03$, and the truncation of the basis is $L_{\text{max}} = N + 2$ for both panels. (Taken from (Rico-Gutierrez *et al.*, 2013))

$gN/6 = 0.4$, the gap is substantially smaller than the value obtained with the LLL approximation as can be seen in Fig. (4.8). This plot also suggests that the energy gap asymptotically tends to a constant value, albeit very small, as N increases, just as in the case of a LLL calculation.

Now, we move to the analysis of the quantum Fisher information in order to assess the performance of these entangled states in quantum metrology schemes, as we did with the bat-like state obtained with a LLL approximation.

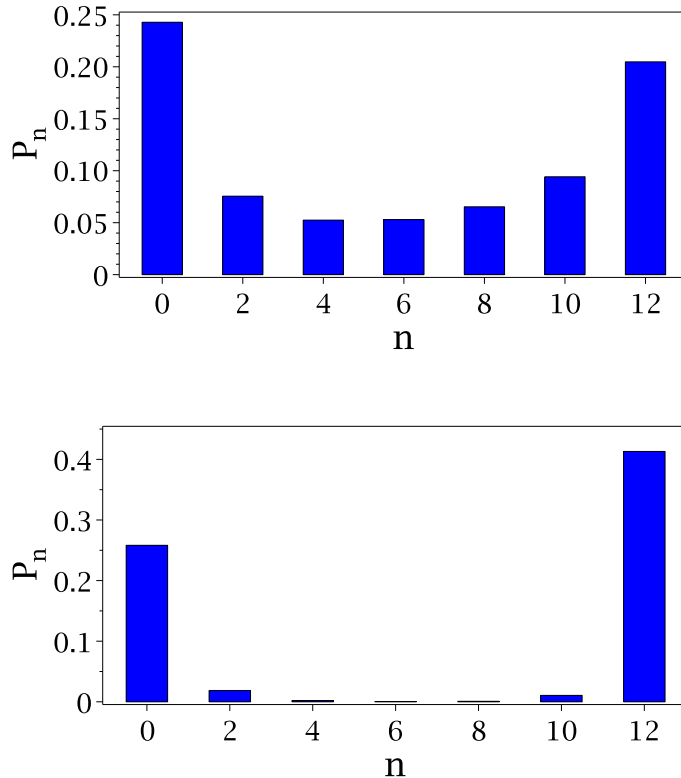


Figure 4.7: The coefficients $P_n = |\langle N - 2n, 2n | \Psi_0(\Omega_c) \rangle|^2$ for the two-mode approximation at the critical frequency using two Landau levels for $N = 12$ particles and two different anisotropy strength. (Top) For this bat-like state the interaction strength is given by $gN/6 = 1$, the anisotropy is $A = 0.05$, and the fidelity of the two-mode approximation is $|\langle \Psi_0(\Omega_c) | \Psi_{\text{TM}} \rangle|^2 = 0.79$. (Bottom) For the cat-like state, the interaction strength is $gN/6 = 0.4$, the anisotropy $A = 0.005$, and the fidelity of the two-mode approximation is $|\langle \Psi_0(\Omega_c) | \Psi_{\text{TM}} \rangle|^2 = 0.70$. The truncation of the basis is $L_{\text{max}} = N + 2$ for both panels.

4.1.1 Quantum Fisher information of the entangled ground states

Since the ground state has a $N00N$ -like shape at Ω_c for $Ng = 6$ as calculated with a two Landau level approximation, we expect the Fisher information to increase

4.1 Tuning entanglement in the rotating trap

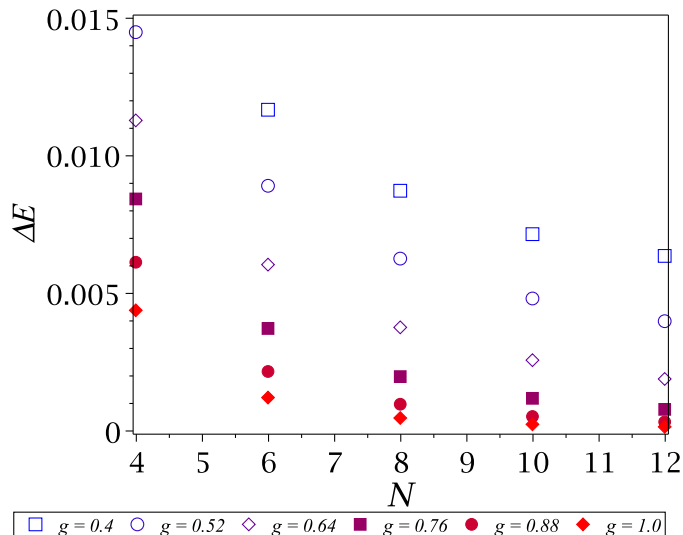


Figure 4.8: Minimal energy gap between the ground state and the first excited state at Ω_{\min} as a function of N for different values of the interaction strength. In all cases, the interaction strength was scaled for each value of N , and the scaled values of g shown in the plot are given by $gN/6$. The calculation was obtained with two Landau levels, and the truncation of the basis is $L_{\max} = N + 6$ in order to have convergence for small values of g and large values of N .

with respect to the bat-like one obtained using the LLL approximation. Although this is actually the case, the most surprising feature of the calculated Fisher information as a function of Ω is its width, which shows a very dramatic change, as can be seen in Fig. (4.9). Here, the Fisher information has been calculated in the same exact way as it was done with the LLL approximation. Whereas the critical frequency has been shifted by roughly 5%, the Fisher information curve has become a very sharp resonance whose width is about two orders of magnitude smaller compared to the one calculated with the LLL approximation. This sharp resonance means that it might be very challenging to create a $N00N$ -like state in experiments because high control of the rotation rate Ω is needed in order to exactly pinpoint the critical frequency.

On the other hand, when the interaction strength is reduced to $gN/6 = 0.4$, we recover the qualitative aspect of the results obtained with the LLL approximation,

4.2 Assessing the validity of the LLL approximation

that is, a broad Fisher information curve for the bat-like state and higher fidelity of the ground state with the two-mode approximation. In addition, the shift in the critical frequency is less than 0.5%, and the two most populated states of the SPDM have the same composition in the angular momentum basis as those found using the LLL approximation, which are given by

$$\begin{aligned}\tilde{\psi}_1 &\approx 0.785\psi_{(0,0)} - 0.607\psi_{(0,2)}, \\ \tilde{\psi}_2 &\approx 0.995\psi_{(0,1)} + 0.116\psi_{(0,3)}.\end{aligned}\tag{4.3}$$

The resulting phase precision calculated with the bat-like and $N00N$ -like states is shown in Fig. (4.10). The performance of the bat-like state is essentially identical to the bat-like state obtained with a LLL calculation, whereas the $N00N$ -like state outperforms the pure bat state and has nearly Heisenberg limited precision as N gets larger. These are remarkable results.

Here, it is worth mentioning that similar qualitative results were found for all the numbers of atoms considered in the simulations for $N \leq 14$. Also, the striking results calculated with two Landau levels do not change significantly when another level is considered for all $N \leq 12$; the case of $N = 14$ and three Landau levels was impractical to simulate due to computational constraints. Furthermore, we were able to simulate the systems with $N = 4$ and $N = 6$ particles up to four Landau levels, and again, we did not see any significant change in the results obtained with two Landau levels. A more detailed discussion about this point is presented in the next section.

Due to the contrasting results obtained by including higher Landau levels, we focus on quantifying the observed differences in the next section. Particularly, we give modified LLL approximation validity criteria based on our numeric results, which have to be taken just as a gross guideline to the validity of the LLL approximation due to the modest number of atoms that we were able to simulate.

4.2 Assessing the validity of the LLL approximation

Thorough assessment of the LLL approximation as it was carried out by (Morris & Feder, 2006), requires more powerful computational facilities than a simple

4.2 Assessing the validity of the LLL approximation

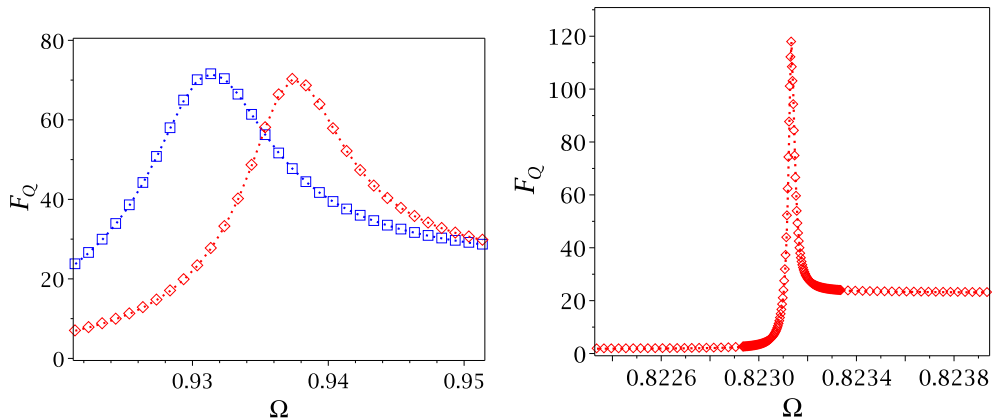


Figure 4.9: The quantum Fisher information as a function of the rotation rate Ω for $N = 12$ particles and an anisotropy strength of $A = 0.03$. (Left) The interaction strength is given by $gN/6 = 0.4$, and the Fisher information as calculated with the LLL approximation (blue empty box) and two Landau levels (red empty box) is shown. (Right) The interaction strength is $gN/6 = 1$, and the horizontal scale is roughly ten times smaller than that of the left panel. (Taken from (Rico-Gutierrez *et al.*, 2013))

personal computer like the one which was used in our calculations. However, our study clearly identifies the relevant parameters and scales involved in establishing a validity regime for the LLL approximation in general, as well as detailed results for small numbers of atoms $N \leq 12$ up to three Landau levels.

First, recall that important differences in the form of the entangled ground state and its Fisher information between a LLL calculation and a two Level one were found for a fixed value of $A \ll 1$ and an interaction strength of $gN/6 = 1$. For this magnitude of the interactions, the typical rotation frequency for the nucleation of the first vortex is $\Omega_1 \approx 0.77$, and thus the standard validity criterion of Eq.(3.59) gives $Ng \ll 28$, hence the $Ng/6 = 1$ scaling should be consistent with the LLL approximation. More importantly, it is also consistent with the power law scaling of $g_{\max} \approx 6.92N^{-1.046}$ for numbers of particles $N \leq 20$, which describes the crossover from the weakly interacting regime pertaining to the LLL approximation to the strongly one where more Landau levels are required to describe the system, as found by (Morris & Feder, 2006). Therefore, it is evident

4.2 Assessing the validity of the LLL approximation

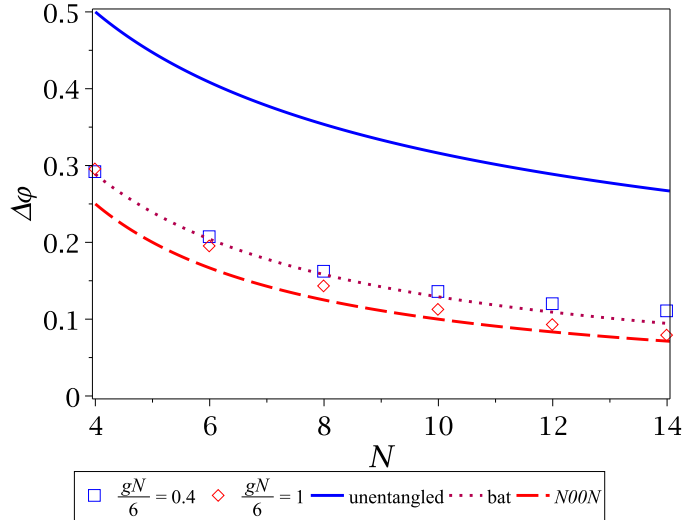


Figure 4.10: Phase precision for the entangled ground state at Ω_c as a function of N using two Landau levels. We plot the phase precision for the $N00N$ state $1/N$, bat state $\sqrt{2}/\sqrt{N(N+2)}$, and unentangled particles $1/\sqrt{N}$ for comparison purposes. All the calculations used $A = 0.03$ and a basis truncation of $L_{\max} = N + 2$.

that neither of these criteria apply for our results regarding the exact form of the ground state or the Fisher information.

However, the estimation of the critical frequency at which the entangled ground state is nucleated is consistent with the standard criteria for the validity of the LLL approximation. As can be seen in Fig. (4.11), for an interaction strength $gN/6 \leq 1$, the relative error of calculating the critical frequency with the LLL approximation is less than 6% for $N = 12$. This tolerance is actually smaller than the 10% considered in the calculation of Ω_1 in (Morris & Feder, 2006), where disagreements larger than ten percent are considered to indicate that more than one Landau level are needed to describe the exact location of Ω_1 . Although we only show results for $N = 12$, we found that the 6% tolerance holds for all numbers of particles that we studied.

Additionally, we show only the calculated critical frequency for values of the interaction strength of $gN/6 \geq 0.4$ because for smaller values than this, when

4.2 Assessing the validity of the LLL approximation

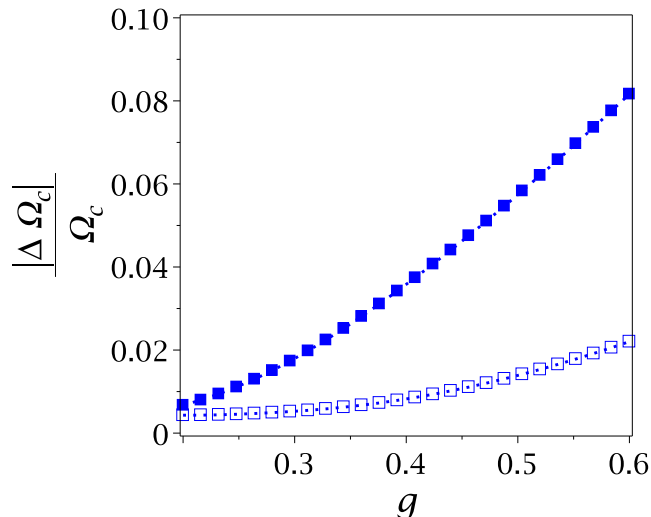


Figure 4.11: The fractional change in the position of the critical rotation frequency Ω_c as a function of the interaction strength for $N = 12$ particles, calculated using two different approximations differing by one Landau level. In each case, the fractional change is calculated at the critical frequency obtained using the lower number of Landau levels. One level approximation (LLL) compared against the two level approximation (solid box) where $\Delta\Omega_c/\Omega_c = |\Omega_c(g)_{2LL} - \Omega_c(g)_{LLL}|/\Omega_c(g)_{LLL}$. Two level approximation compared against the three level approximation (empty box) where $\Delta\Omega_c/\Omega_c = |\Omega_c(g)_{3LL} - \Omega_c(g)_{2LL}|/\Omega_c(g)_{2LL}$. (Taken from (Rico-Gutierrez *et al.*, 2013))

$A = 0$, the ground state crossings begin to be tightly confined to a small rotation frequency window near the centrifugal limit $\Omega = 1$. Thus, the addition of the anisotropy with strength $A = 0.03$ no longer results in a well localised anticrossing for each respective crossing, and a proper account for the way the anisotropic term lifts the degeneracy requires a larger angular momentum basis truncation since the ground state becomes more sensitive to the injection of higher angular momentum states near the centrifugal limit. Without proper account for higher angular momentum states, the SPDM shows an increasing participation of a third mode as the interaction strength is decreased, drastically deteriorating the

4.2 Assessing the validity of the LLL approximation

two-mode approximation. Furthermore, as g decreases, the critical frequency is located increasingly closer to the centrifugal limit, eventually entering a region where the condensate is known to experience dynamical instabilities that make the condensate fly apart (Rosenbusch *et al.*, 2002; Sinha & Castin, 2001). In the case of an anisotropy strength of $A = 0.03$, this region starts at rotation frequencies of $\Omega \sim \sqrt{1 - 4A} = 0.969$. Therefore, we focus on values of $gN/6 \geq 0.4$ since these give rise to critical frequencies sufficiently far from the instability region and do not require a basis truncation larger than $L_{\max} = N + 2$.

Next, we quantify the difference in the magnitude of the Fisher information as calculated with different numbers of Landau levels. But first, let us explain the two general methods that we chose to compare different calculations of the Fisher information. The first one consists in comparing values of the Fisher information of the ground state at rotation frequencies measured from the critical frequency of each respective approximation. This method is motivated by the very sharp resonance-like form of the Fisher information which together with the fact that the critical frequency converges slowly with respect to the addition of Landau levels, results in an extremely slow convergence of the Fisher information at absolute values of the rotation frequency. Thus, this method allows us to estimate the converged value of the Fisher information at the exact critical frequency which would result from a full quantum calculation. Let us call this method the “relative comparison” method, or method I in short. The second method consists in comparing the calculated Fisher information at rotation frequencies measured from the critical frequency obtained with the lower number of Landau levels involved in the calculation. This method allows us to estimate the actual difference in Fisher information that would be observed in an experiment if we were being guided by the approximation with the lower number of Landau levels. Let us call this method the “absolute comparison” method, or method II in short.

We plot the calculated Fisher information of the entangled ground state for different values of the interaction strength g and different Landau level approximations using method I in Fig. (4.12). Even though we have not been able to calculate the Fisher information using four Landau levels for $N > 6$, these results suggest that the Fisher information converges monotonically with the number of Landau levels if one excludes the lowest Landau level approximation from the

4.2 Assessing the validity of the LLL approximation

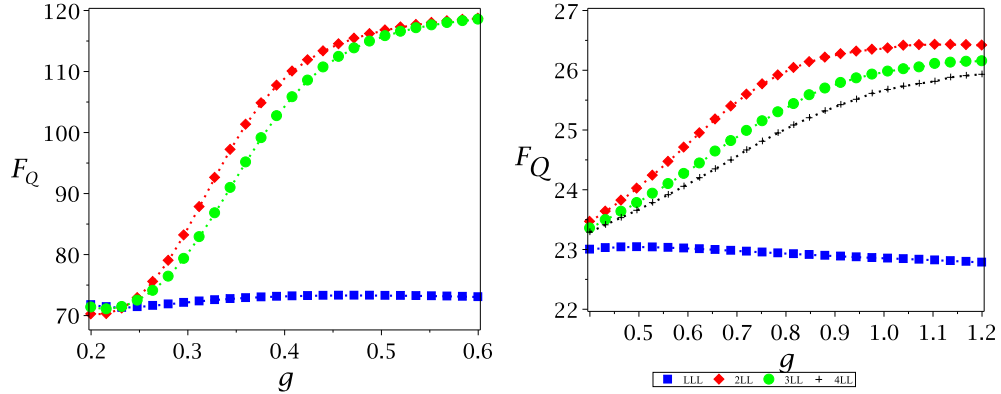


Figure 4.12: The quantum Fisher information of the ground state for various basis truncations as a function of the interaction strength at the critical frequency Ω_c calculated with the respective truncated basis (Method I). (Left) Calculation for $N = 12$ particles. The labels are the same as those shown in the right panel. (Right) Calculation for $N = 6$ particles. The anisotropy strength is $A = 0.03$ for both panels. (Taken from (Rico-Gutierrez *et al.*, 2013))

series. With the addition of each subsequent Landau level, the correction to the critical frequency gets smaller and the calculated Fisher information gets closer to the true value that would result from a full quantum calculation at Ω_c . The fractional change in the Fisher information as calculated using two Landau levels with respect to a lowest Landau level calculation is plotted in Fig. (4.13). If we consider a tolerance of 10% as our criterion for the validity of the lowest Landau level in this context, we see that these results give a maximum interaction strength compatible with the LLL approximation equal to $Ng_{\max}/6 \approx 0.5$.

On the other hand, when the comparison method II is used, we obtain results like the example for $N = 12$ in Fig. (4.14). In this case, even for very small values of the interaction strength $gN/6 \approx 0.4$, the fractional error between the LLL approximation and two Landau levels is $\sim 160\%$, and similarly for the case of two Landau levels and three Landau levels. This means that using the LLL approximation or even a two Landau level one to predict the critical frequency in experiments is likely to lead to the nucleation of a sub-optimal state that has low fidelity with the true entangled state at the true critical frequency. As

4.2 Assessing the validity of the LLL approximation

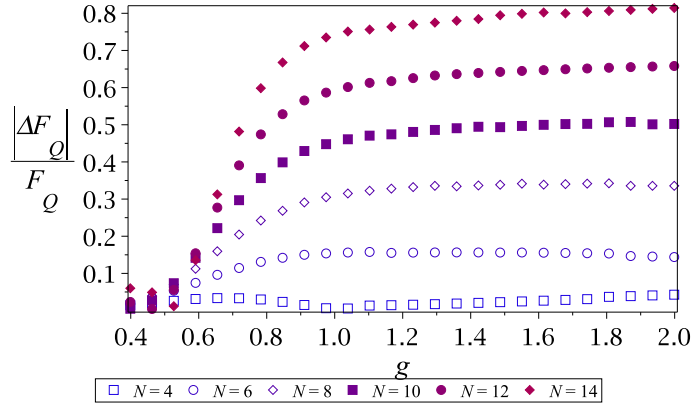


Figure 4.13: The fractional change in the quantum Fisher information F_Q as a function of the interaction strength, using the LLL approximation and two Landau levels. The Fisher information is calculated at the critical frequency obtained with the respective truncated basis (Method I), and the fractional change is calculated as $\Delta F_Q/F_Q = |F_Q(g)_{2LL} - F_Q(g)_{LLL}|/F_Q(g)_{2LL}$. The anisotropy strength is $A = 0.03$ for all cases and the horizontal axis is shown for a scaled g by a factor of $N/6$.

was mentioned before, this is a consequence of a slow convergence of the Fisher information at absolute values of the rotation frequency: with each subsequent addition of an extra Landau level, the magnitude of the correction for the critical frequency is barely comparable or much larger than the width of the Fisher information, thus resulting in a large fractional error. Nevertheless, we saw that when the Fisher information is calculated at rotation frequencies relative to the critical frequency as calculated with each respective approximation, the two Landau level approximation seems to give a very accurate value of the Fisher information that has nearly converged to the value that would result from a full quantum calculation. This is also true for the width of the fisher information curve, as can be seen in Fig. (4.15), where we define Γ_Q to be given by the length of the left half of the width at half maximum. Again, the LLL approximation gives a poor prediction of the Fisher information width even for small values of g for all

4.2 Assessing the validity of the LLL approximation

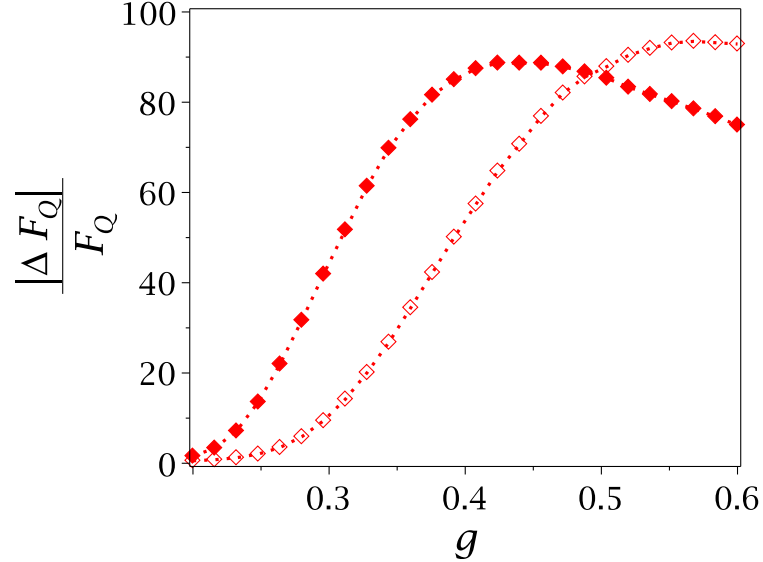


Figure 4.14: The fractional change in the quantum Fisher information F_Q as a function of the interaction strength, calculated using two different approximations differing by one Landau level. In each case, the fractional change is calculated at the critical frequency obtained using the lower number of Landau levels (Method II). One level approximation (LLL) compared against the two level approximation (solid diamond) where $\Delta F_Q/F_Q = |F_Q(g)_{2LL} - F_Q(g)_{LLL}|/F_Q(g)_{2LL}$. Two level approximation compared against the three level approximation (empty box) where $\Delta F_Q/F_Q = |F_Q(g)_{3LL} - F_Q(g)_{2LL}|/F_Q(g)_{3LL}$. (Taken from (Rico-Gutierrez *et al.*, 2013))

numbers of particles, predicting a width which is roughly twice the value obtained with two Landau levels for $gN/6 \approx 0.4$. As the interaction strength is increased, the LLL approximation gives extremely inaccurate predictions for the width of the Fisher information which are even more inexact than the predictions for the Fisher information as assessed with both methods I and II. This time, it seems necessary to go up to three Landau levels in order to obtain accurate predictions for the width of the Fisher information as the interaction strength gets much larger than $gN/6 = 0.4$, as suggested by the right panel in Fig. (4.15)

In conclusion, while the LLL approximation can provide accurate predictions

4.2 Assessing the validity of the LLL approximation

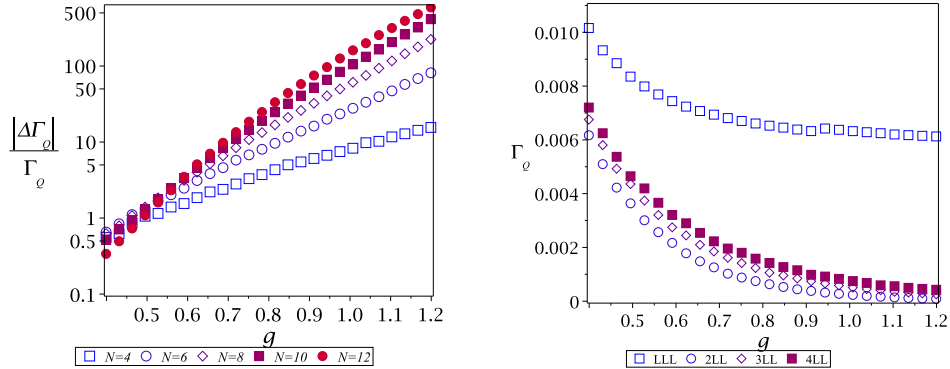


Figure 4.15: Analysis of the Fisher information width with different Landau levels. (Left) Fractional error of the Fisher information width as a function of the interaction strength calculated as $|\Delta\Gamma_Q|/\Gamma_Q = |\Gamma_Q(g)_{2LL} - \Gamma_Q(g)_{LLL}|/\Gamma_Q(g)_{2LL}$. $\Gamma_Q(g)$ is defined as the left width of the Fisher information at half maximum. (Right) Fisher information width as a function of the interaction strength for $N = 6$ particles and different numbers of Landau levels. The anisotropy is $A = 0.03$ and $L_{\max} = N + 2$ for both panels.

of the Fisher information of the entangled state at the true critical frequency obtained from a full quantum calculation for values of the interaction strength $gN/6 \leq 0.5$, it gives inaccurate estimations for the width of the Fisher information for all values of the interaction strength $gN/6 \geq 0.4$; particularly, it gives very poor predictions for values of the interaction strength which are commonly regarded as pertaining to the LLL approximation regime. Therefore, in order to obtain accurate estimates of the Fisher information width, one needs to consider at least three Landau levels in order to cover all possible values of the interaction strength up to $gN/6 = 1$. More importantly, if one is to use these numerical predictions in order to guide experiments, a very precise calculation of the critical frequency is needed that requires at least four or five Landau levels, particularly for values of the interaction strength $gN/6 \approx 1$, such that the actual ground state and Fisher information obtained in the experiment is close to the one predicted here. Ideally, the calculation of the critical frequency with up to four or five Landau levels could be used to extrapolate the results to predict the many-level result. This, however, requires powerful computational resources and alternative

ways of finding a very accurate location of the critical frequency would be highly desirable.

4.3 Conclusions

We found that the LLL approximation predicts a $(N/2+1)$ -fold degeneracy at the first ground state crossing when $A = 0$, regardless of the value of the interaction strength g . Then, the inclusion of a small anisotropy $A \ll 1$ lifts the degeneracy in the same way for all values of g , resulting in the nucleation of a bat-like state at the critical frequency. No matter how strong or weak the interactions are, we always obtain a bat-like state due to the fact that the energy spectrum is the same up to a scaling constant for any value of the interaction strength g .

On the other hand, when another Landau level is added to the approximation, the first ground state crossing is no longer $(N/2 + 1)$ -fold degenerate (in fact, it is only doubly degenerate), and differences in the relative values of g and A lead to different ways in which the anisotropic term couples higher angular momentum states to the ground state. As a result, careful tuning of g and A can produce bat-like states, as well as $N00N$ -like ones. Particularly, the $N00N$ -like states can be obtained for $A = 0.03$ and $gN/6 \approx 1$, which is a weak interaction strength commonly regarded as compatible with the LLL approximation. Evidently, in view of our results, this is not the case when a small anisotropy is present in the system. Whereas the correction to the critical frequency is roughly about 5% when two Landau levels are considered, the Fisher information and the width of the Fisher information curve as a function of the rotation frequency show drastic differences with respect to the same values calculated with a LLL calculation. Then, we saw that in order to accurately make an estimation of the Fisher information at the true critical frequency and its width, at least two Landau levels need to be considered in general. However, due to the very small width of the Fisher information, a three or four Landau level calculation is needed in order to extrapolate the many-level result for the critical frequency, so that in experiments, the entangled ground state generated at this extrapolated critical frequency has a high fidelity with the bat or $N00N$ -like states predicted by our numeric results.

4.3 Conclusions

Thus, the rotating anisotropic condensate constitutes a simple system that has already been demonstrated experimentally, and which offers the creation and tuning of entanglement via an equally simple mechanism, i.e. that of increasing or decreasing the interaction strength, which can be achieved with Feshbach resonances in experiments.

Chapter 5

Interferometric scheme for rotation measurements

Very precise measurement of rotation frequencies plays an important role in many areas of science and technology including, among others, inertial navigation systems, detection of fluctuations in the rotation of the Earth and in tests of general relativity. Currently, the state-of-the-art devices used to perform rotation measurements in these areas use unentangled states as their initial resource; therefore their precision cannot surpass the standard quantum limit. As was mentioned before, Bose–Einstein condensates are very promising systems to implement quantum metrology due to their many unrivaled features such as highly accurate control over their dynamics in experiments, high level of quantum coherence, and the fact that they provide a conceptually simple way of generating many-body entanglement, particularly by setting them in rotation. Consequently, these many-body entangled states have the prospect of leading to the development of ultra-precise gyroscopes which can overcome the standard quantum limit. In this Chapter, we present an interferometric scheme to measure rotation frequencies with sub-shot noise precision. The scheme is capable of using a range of different entangled states from bat-like to $N00N$ -like ones and as a result different degrees of robustness against particle losses can be attained. Also, we demonstrate that the scheme is amenable to an experimental proof-of-principle implementation, and give a feeling of some of the possible improvements that can enhance the performance of the scheme and its precision.

5.1 General overview

Our interferometric scheme is based on the operation of the two-mode Mach–Zehnder interferometer reviewed in chapter 2, which in general terms consists of the creation of a two-mode entangled state, phase accumulation, recombination of the two paths, and the read-out stage. Similarly, in our case the scheme can be divided into four major stages representing the operation of a Mach–Zehnder interferometer with the exception of the read-out stage. The first one consists in preparing the entangled ground state by adiabatically bringing the condensate from the non-rotating regime to a rotating BEC at the critical frequency Ω_c . Once the entangled state has been nucleated, the second stage consists in rapidly shifting away from the critical frequency to a nearby rotation frequency of $\Omega_c \pm \Delta\Omega$. This step simulates the coupling of our condensate “probe” to the system whose rotational motion we want to measure. The conceptual idea of the interferometric scheme depends on this step being performed fast enough so that the ground state and first excited state at $\Omega_c \pm \Delta\Omega$ get populated, but slow enough so that higher excited states have negligible population. Fortunately, our results show that a very broad range of frequency shift speeds satisfies this requirement for a certain window of rotation frequencies near Ω_c . Furthermore, as we shall see, the system offers the possibility of going beyond this two-mode concept increasing the range of frequency shifts that can be measured with sub-shot noise precision.

After accomplishing the population of the ground state and first excited state at $\Omega_c \pm \Delta\Omega$, the third stage comprises the phase imprinting step. This step consists of a simple free evolution during a time τ which imprints a phase $\exp(i\Delta E_{10}\tau)$ between the ground state and the first excited state at $\Omega_c \pm \Delta\Omega$. Here, ΔE_{10} is the energy gap between the ground state and the first excited state at $\Omega_c \pm \Delta\Omega$, and τ is the waiting time for the free evolution. The information about $\Delta\Omega$ is encoded into the state of the condensate through ΔE_{10} , and therefore, measuring this phase enables us to estimate the difference in rotation rate $\Delta\Omega$ between the condensate and the test system. Finally, once the phase has been imprinted into the condensate, we take the BEC back to the non-rotating regime by reversing the sequence of steps. This means, very quickly switching back to Ω_c from $\Omega_c \pm \Delta\Omega$, and then adiabatically reducing the rotation frequency until the

5.2 Adiabatic nucleation of the entangled state

condensate reaches a very slow rotating regime where performing measurements is more convenient due to the expectation of interference fringes between the rotating and non-rotating components of the condensate in this regime. Currently, the final step of reversing the sequence and bringing the condensate to the non-rotating regime is subject of ongoing research, and as such it is not considered in this thesis.

In order to simulate the sequence of steps described above, we follow (Dagnino *et al.*, 2009a) and solve the time-dependent Schrödinger equation

$$i\frac{\partial}{\partial t}|\Psi(t)\rangle = \hat{H}(t)|\Psi(t)\rangle \quad (5.1)$$

for the initial solution $|\Psi(t=0)\rangle$ at Ψ_0 . By expanding $|\Psi(t)\rangle$ in the many-body angular momentum basis as $|\Psi(t)\rangle = \sum_i c_i(t)|\Phi_i\rangle$, and projecting Eq.(5.1) on the state $|\Phi_j\rangle$, we obtain a set of first order differential equations for the coefficients $c_i(t)$,

$$i\frac{\partial}{\partial t}c_j(t) = \sum_i c_i(t)\langle\Phi_j|\hat{H}(t)|\Phi_i\rangle, \quad (5.2)$$

which is solved numerically using a Fehlberg fourth-fifth order Runge-Kutta method with degree four interpolant implemented in *Maple*. In all cases where the rotation frequency Ω is varied, we have assumed linear dependence in time as,

$$\Omega(t) = \Omega_0 + \gamma t, \quad (5.3)$$

where γ is the constant rate of change for the rotation frequency and Ω_0 is a particular initial frequency. This linear dependence is the most simple way to model the dynamics of the system and yet, it is very demanding in computational terms, particularly when studying adiabatic passages with higher Landau levels. The adiabaticity criterion will be easier to fulfil, both in experiments and simulations, by taking a more general and optimised time dependence. However, this is the subject of future work.

5.2 Adiabatic nucleation of the entangled state

The stationary ground state contour provides an adiabatic pathway into the entangled state at Ω_c . In this section we study the feasibility of this approach.

5.2 Adiabatic nucleation of the entangled state

We consider the case $N = 6$ in detail and later on, we discuss the results and implications for larger numbers of particles. The idea behind this analysis is to start with a slowly rotating condensate at some $\Omega(t) = \Omega_0$, which in principle can be taken to be zero, and then slowly ramp up the rotation frequency until Ω_c is reached. The equilibrium state at $\Omega_0 \ll \Omega_c$ can be achieved after relaxation once the system is suddenly put in rotation at this initial frequency (Madison *et al.*, 2000b). In our study, the only control parameter is the rotation frequency Ω , while the other parameters such as g and A remain fixed. The size of the energy gap between the ground state and the first excited state determines the maximum speed of this evolution at any given point so that the transition rate to higher states remain negligible. The instantaneous probability for a non-adiabatic transition from the ground state to the first excited state after a time evolution of t_f is given by (Messiah, 1965)

$$p_{0 \rightarrow 1} \approx \left| \int_0^{t_f} \alpha_{10}(t) \exp \left(i \int_0^t \Delta E_{10}(\tau) d\tau \right) dt \right|^2, \quad (5.4)$$

where α_{10} can be thought as a measure of the speed of rotation of the ground state along the direction of the first excited state given by

$$\alpha_{10} = \langle \Psi_1(t) | \frac{d|\Psi_0(t)\rangle}{dt} \rangle, \quad (5.5)$$

and $\Delta E_{10}(t)$ is the instantaneous energy gap between the two states. If α_{10} and ΔE_{10} are time-independent, Eq.(5.4) is readily integrated to give

$$p_{0 \rightarrow 1} \approx \left| \frac{\alpha_{10}}{\Delta E_{10}} \right|^2 2(1 - \cos \Delta E_{10} t_f). \quad (5.6)$$

Therefore, $p_{0 \rightarrow 1}$ is a quantity of the order of $|\alpha_{10}/\Delta E_{10}|^2$. This means that during a time evolution where α_{10} and ΔE_{10} exhibit a sufficiently smooth variation, $p_{0 \rightarrow 1}$ will at most be of the order of magnitude of the maximum value attained by the ratio $|\alpha_{10}/\Delta E_{10}|^2$ in the interval $(0, t_f)$:

$$p_{0 \rightarrow 1} \lesssim \max \left(\left| \frac{\alpha_{10}}{\Delta E_{10}} \right| \right)^2. \quad (5.7)$$

We can use these results to estimate the order of magnitude of γ in Eq.(5.3) that gives the fastest time evolution compatible with adiabaticity, as a guide for

5.2 Adiabatic nucleation of the entangled state

our numeric calculations . We start by differentiating the eigenvalue equation $\hat{H}|\Psi_0\rangle = E_0|\Psi_0\rangle$ with respect to the rotation frequency Ω which appears as a parameter in the Hamiltonian and the eigenvectors:

$$\frac{d\hat{H}}{d\Omega}|\Psi_0(\Omega)\rangle + \hat{H}(\Omega)\frac{d|\Psi_0\rangle}{d\Omega} = \frac{dE_0}{d\Omega}|\Psi_0(\Omega)\rangle + E_0(\Omega)\frac{d|\Psi_0\rangle}{d\Omega}. \quad (5.8)$$

Taking the scalar product with $\langle\Psi_1|$ and using $d\hat{H}/d\Omega = -\hat{L}_z$ which is a consequence of Eq.(3.1), we obtain

$$\alpha_{10} = \langle\Psi_1|\frac{d|\Psi_0\rangle}{dt} = \frac{d\Omega}{dt} \frac{\langle\Psi_1|\hat{L}_z|\Psi_0\rangle}{\Delta E_{10}(\Omega)}, \quad (5.9)$$

where we have also used the chain rule $d|\Psi_0\rangle/dt = (d\Omega/dt)(d|\Psi_0\rangle/d\Omega)$. Therefore, we have

$$\left| \frac{\alpha_{10}}{\Delta E_{10}} \right| = \left| \gamma \frac{\langle\Psi_1|\hat{L}_z|\Psi_0\rangle}{\Delta E_{10}^2(\Omega)} \right|. \quad (5.10)$$

The matrix element $\langle\Psi_1|\hat{L}_z|\Psi_0\rangle$ in the last expression is approximately zero near the non-rotating regime since the ground state and the first excited state are nearly eigenvectors of the total angular momentum \hat{L}_z when $\Omega \approx 0$ with eigenvalues of 0 and 2 respectively. Also, the same matrix element is at most of order N in the vicinity of the avoided crossing where the ground state is transiting from a non-rotating state with $\langle L \rangle \approx 0$ to the one vortex state with $\langle L \rangle \approx N$. Hence, the following expression holds for $\Omega < \Omega_c$:

$$\left| \frac{\alpha_{10}}{\Delta E_{10}} \right| \leq \left| \frac{\gamma N}{\Delta E_{10}^2(\Omega)} \right|, \quad (5.11)$$

and consequently, the maximum value of $|\alpha_{10}/\Delta E_{10}|$ in Eq.(5.7) is attained at the avoided crossing where the energy gap is a minimum. In summary, the transition rate from the ground state to higher excited states for an arbitrary linear ramping of the rotation frequency Ω anywhere in the interval $(0, \Omega_c)$ is bounded by

$$p_{0 \rightarrow 1} \lesssim \left| \frac{\gamma N}{\Delta E_{10}^2(\Omega_{\min})} \right|^2, \quad (5.12)$$

where $\Delta E_{10}(\Omega_{\min})$ is the energy gap at the avoided crossing point. Hence, the condition $p_{0 \rightarrow 1} \ll 1$ for an evolution from Ω_0 to Ω_c which ensures that the system

5.2 Adiabatic nucleation of the entangled state

follows adiabatically the ground state determines the maximum rate of change of Ω as

$$\gamma_{\max} \approx \frac{\Delta E_{10}^2(\Omega_{\min})}{N} \xi, \quad (5.13)$$

where $\xi (\ll 1)$ is a constant determined by the numeric simulations that ensures the adiabatic condition.

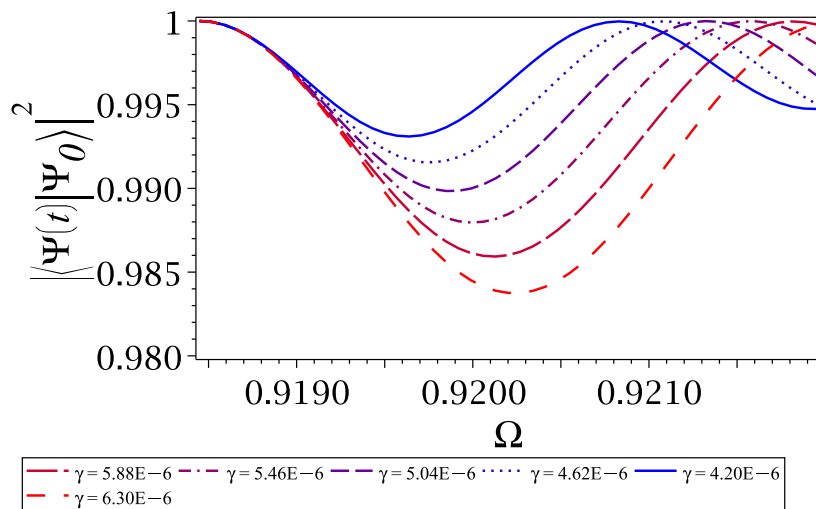


Figure 5.1: Numeric results for the overlap between $|\Psi(t)\rangle$ and the stationary GS for $N = 6$ bosons, $A = 0.03$ and $g = 0.44$. The initial rotation frequency $\Omega_0 = 0.918$ is well below the critical frequency $\Omega_c = 0.922$ and the avoided crossing rotation frequency $\Omega_{\min} = 0.920$. The different values of γ correspond to values of ξ in the range $[0.2, 0.3]$ obtained with Eq.(5.13).

In order to determine whether the time evolution of the quantum state has adiabatically followed the stationary profile in our simulations, we use a slightly stronger criterion than that of (Dagnino *et al.*, 2009a), and consider that one gets adiabaticity when the overlap between $|\Psi(t)\rangle$ and the exact GS at any point during the evolution is larger than 0.99 for an initial rotation frequency $\Omega_0 < \Omega_{\min}$. This modified criteria ensures that if we start the evolution from a different initial rotation frequency Ω_0 , the system will still reach the critical frequency Ω_c with an overlap larger than 0.99. In Fig. (5.1) we show the numeric results for the fidelity of the evolved state with the stationary ground state for a typical set-up in the “bat” regime. We found that a value of $\xi = 0.2$ ensures the adiabaticity of

5.2 Adiabatic nucleation of the entangled state

the time evolution for a wide range of the interaction strength of $0.3 \leq g \leq 1.0$ for $N = 6$ and $A = 0.03$. Unfortunately, we have not been able to corroborate whether this feature holds for $N > 6$ due to computational constraints; however, we have checked that it is still valid for small values of $g \approx (6/N) \times 0.4$ when $N = 8$. Also, we have compared the profiles of the total average angular momentum \hat{L}_z as a function of Ω with respect to the stationary one. We show this comparison in Fig. (5.2) for the same particular case as that of Fig. (5.1). The difference between the stationary curve and the one obtained with adiabatic evolution depends on the particular value of g , but it is always of the order of ~ 0.1 in the range $g = 0.3 \dots 1.0$.

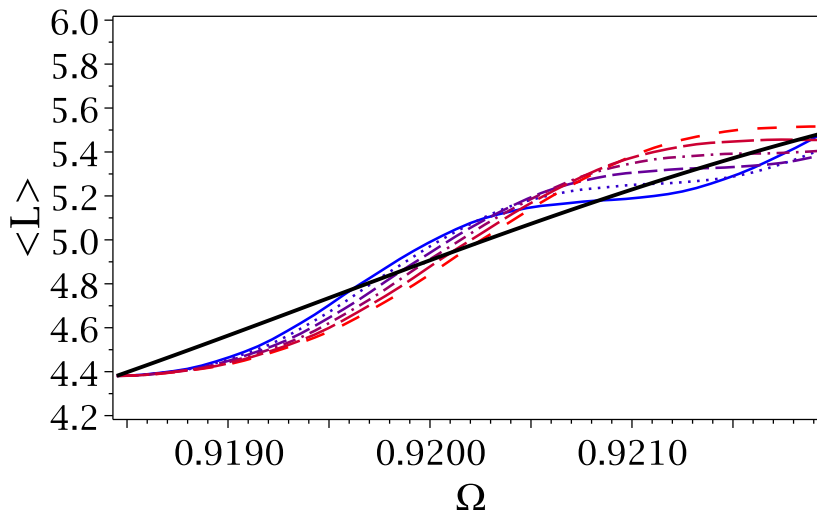


Figure 5.2: Average total angular momentum of the resulting dynamic state as a function of the rotation frequency for $N = 6$ bosons, $A = 0.03$ and $g = 0.44$. All the parameters and labels are identical to those in Fig. (5.1). The black thick solid line profile corresponds to the average total angular momentum of the stationary GS.

We now present numeric predictions of the estimated real time needed for an adiabatic nucleation of the entangled state. As we have seen in chapter 4, the energy gap at the avoided crossing decreases as the interaction strength increases, as well as the number of particles is increased. Therefore, as a consequence of Eq.(5.13), we expect that the nucleation time for a $N00N$ state will be consid-

5.2 Adiabatic nucleation of the entangled state

erably larger than that of a bat state, and that both times will be even larger as N is increased. The total amount of time spent in the adiabatic passage $\Delta\tilde{t}_{\text{adiab}}$ is given by

$$\Delta\tilde{t}_{\text{adiab}} = \Delta\Omega/\gamma_{\text{max}}, \quad (5.14)$$

where $\Delta\tilde{t}_{\text{adiab}}$ is a dimensionless quantity in our choice of units, and the respective time in seconds is given by $\Delta\tilde{t}_{\text{adiab}}/\omega_{\perp}$. Using this expression, the predicted nucleation time in seconds as a function of g for a few different numbers of particles is shown in Fig. (5.3), where we have taken $\omega_{\perp} = 2\pi \times 210$ Hz as a typical value for the harmonic trap frequency found in experiments (Chevy *et al.*, 2000).

These results suggest that the proposed adiabatic nucleation scheme, as it stands, might be impractical even for bat states of small numbers of particles due to the long nucleation times, which are very large compared to the typical condensate lifetime of ~ 16 s (Soding *et al.*, 1999). However, in practice one usually performs a piecewise adiabatic evolution with different optimised values of $\gamma = d\Omega/dt$ and A for different segments. Here, we give evidence that nucleation times can be vastly improved even with a simple two-segment evolution with fixed trap anisotropy A . We have analyzed an adiabatic evolution from $\Omega_0 = 0.4$ to Ω_c by dividing it in two linear ramps of the rotation frequency; the first one corresponds to the interval $(\Omega_0, \Omega_c - 0.01)$ with $\gamma = 0.1 \times N/\Delta E^2(\Omega_c - 0.01)$, and the second one corresponds to $(\Omega_c - 0.01, \Omega_c)$ with $\gamma = 0.1 \times N/\Delta E^2(\Omega_{\text{min}})$; where the considered length of the second segment is 0.01 in order to reflect the fact that typical experimental uncertainty for rotation frequencies is of the order of 1% (Bretin *et al.*, 2004) and any further optimisation of the adiabatic nucleation within 1% of the critical frequency would be unattainable. The much improved times for $N = 6$ and $N = 10$ are shown in Fig. (5.4) and Fig. (5.5) respectively.

To summarise this section, we have presented numeric results for the adiabatic nucleation of the entangled state for small numbers of particles and studied its practical feasibility. We have found that although a straight linear ramping of the rotation frequency from the non-rotating regime to the critical frequency might pose a problem, an optimised ramp sequence consisting in different piecewise linear portions connecting points in the $\Omega - A$ space can vastly reduce nucleation times and make the scheme experimentally feasible. Furthermore, since

5.2 Adiabatic nucleation of the entangled state

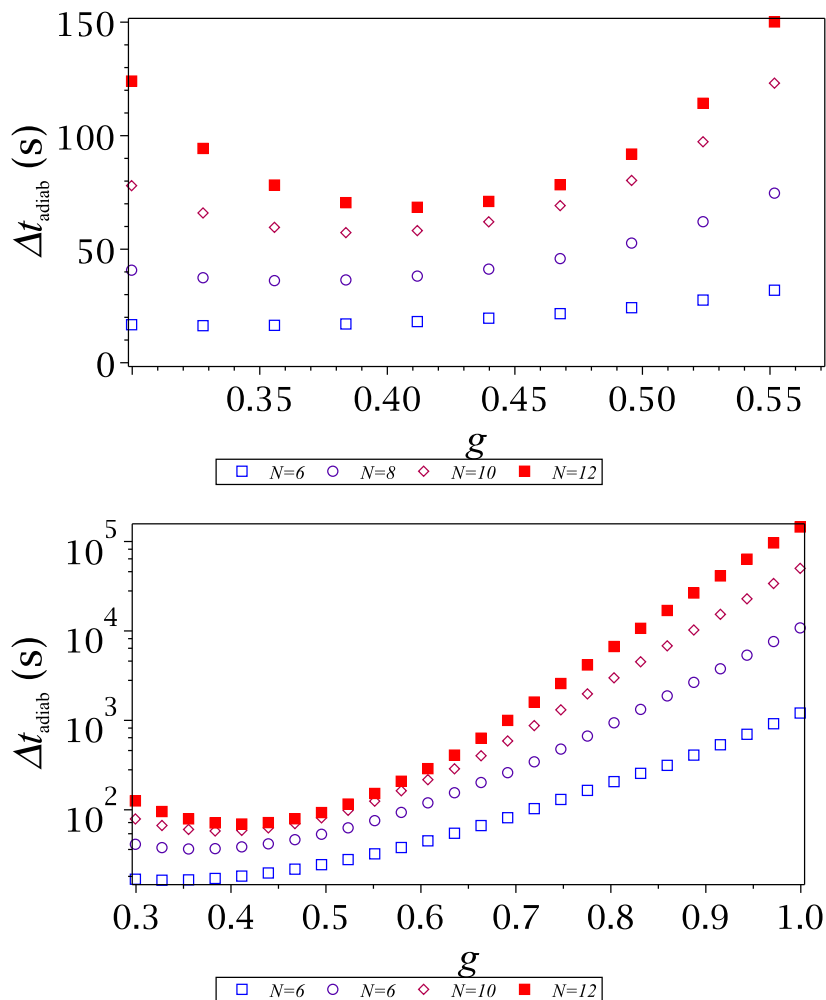


Figure 5.3: Predicted adiabatic evolution time as a function of the interaction strength for $N = 6, 8, 10$ and 12 particles. The evolution for all cases is taken from $\Omega_0 = 0.4$ to $\Omega_f = \Omega_c$, using a value of γ prescribed by Eq.(5.13) with $\xi = 0.1$ and $A = 0.03$. In these plots, we have assumed a typical harmonic trap frequency of $2\pi \times 210$ Hz and the interaction strength g has been scaled by a factor of $(6/N)$.

the actual ramp time is inversely proportional to ω_{\perp} , the use of a much tighter trap can further reduce the time spent in the adiabatic passage. Here, we have used $\omega_{\perp} = 2\pi \times 210$ Hz which is a typical trap frequency found in experiments by Dalibard *et al* (Bretin *et al.*, 2004); however, (Gemelke & Chu, 2010) report the implementation of a confining trap with ω_{\perp} up to 6 kHz which dramatically

5.2 Adiabatic nucleation of the entangled state

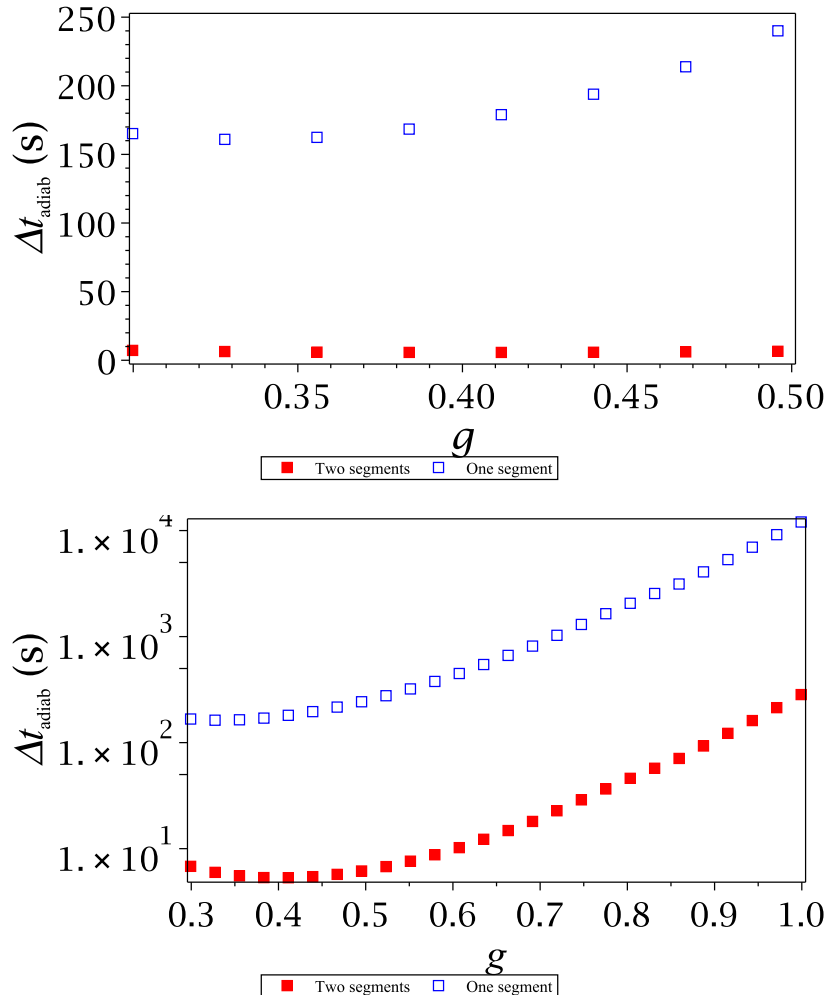


Figure 5.4: Comparison of the predicted adiabatic evolution time as a function of the interaction strength for $N = 6$ using one and two different linear ramps of the rotation frequency. The evolution with only one segment corresponds to the data presented in Fig. (5.3). On the other hand, the two-segment evolution corresponds to a ramping of Ω in the interval $(0.4, \Omega_c - 0.01)$ with $\gamma = 0.1 \times N/\Delta E^2(\Omega_c - 0.01)$, followed by a second ramping of Ω in the interval $(\Omega_c - 0.01, \Omega_c)$ with $\gamma = 0.1 \times N/\Delta E^2(\Omega_{\text{min}})$. We have assumed a typical harmonic trap frequency of $2\pi \times 210$ Hz and the interaction strength g has been scaled by a factor of $(6/N)$.

reduces the nucleation time. In fact, Gemelke *et al* have experimentally demonstrated an adiabatic ramp sequence that brings the condensate to higher rotation

5.2 Adiabatic nucleation of the entangled state

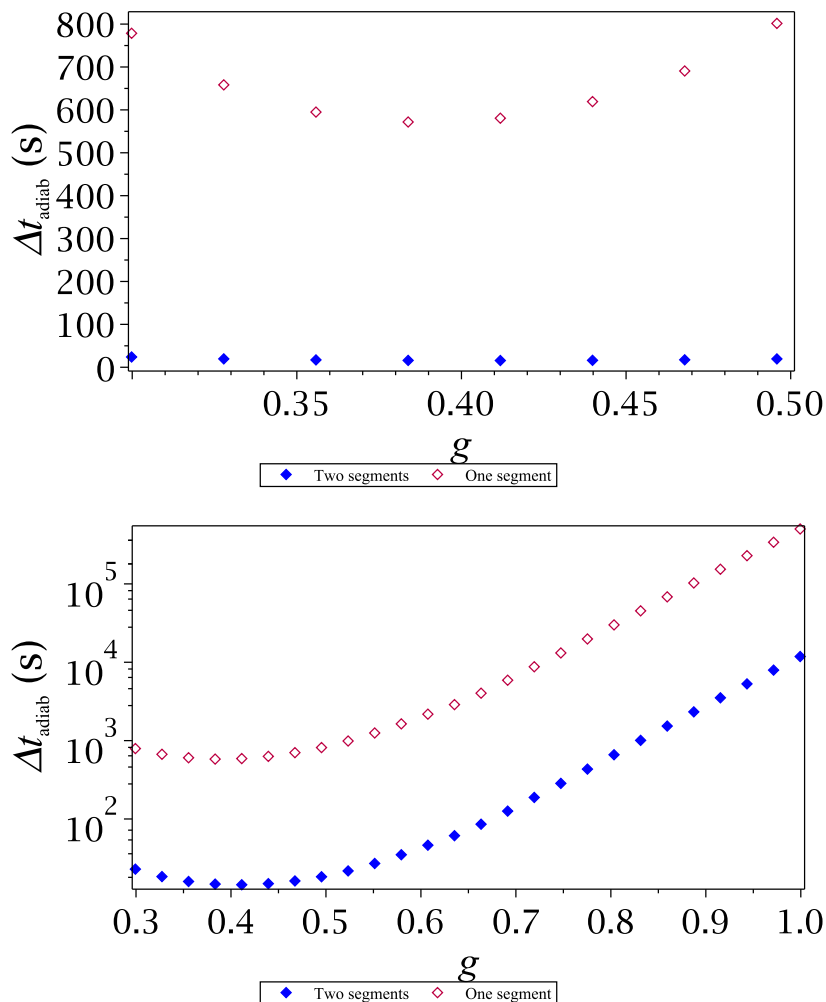


Figure 5.5: Comparison of the predicted adiabatic evolution time as a function of the interaction strength for $N = 10$ using one and two different linear ramps of the rotation frequency. The evolution with only one segment corresponds to the data presented in Fig. (5.3). On the other hand, the two-segment evolution corresponds to a ramping of Ω in the interval $(0.4, \Omega_c - 0.01)$ with $\gamma = 0.1 \times N/\Delta E^2(\Omega_c - 0.01)$, followed by a second ramping of Ω in the interval $(\Omega_c - 0.01, \Omega_c)$ with $\gamma = 0.1 \times N/\Delta E^2(\Omega_{\text{min}})$. We have assumed a typical harmonic trap frequency of $2\pi \times 210$ Hz and the interaction strength g has been scaled by a factor of $(6/N)$.

frequencies $\Omega_{FQH} > \Omega_c$ where the ground state is closely analogous to topological states of electronic systems exhibiting fractional quantum Hall effects, and they

5.3 Non-adiabatic rotation frequency shift and Phase accumulation

report total ramp times of the order of milliseconds for small numbers of atoms $N \sim 5$. Moreover, the interferometric scheme can be modified in order to account for non-perfect adiabaticity by including an additional waiting time at the critical frequency, thereby reducing the overall time that the interferometric scheme takes to be performed. This modification is currently being researched and it will be a central subject of future research.

5.3 Non-adiabatic rotation frequency shift and Phase accumulation

After having nucleated the entangled state at the critical frequency, the next step is to couple our BEC “probe” to the “test” system whose rotation rate Ω_T we want to measure. In order to do this, we would need to have a first good estimate of the “test” system’s rotation frequency; thus, making our quantum strategy to measure Ω_T a refinement over the already known precision $\delta\Omega_T$. Before we nucleate the entangled state, we begin by tuning the harmonic trap frequency ω_\perp so that the resulting critical frequency Ω_c is as close as possible to the estimate Ω_T . After this frequency matching, the condensate is adiabatically brought to the critical frequency in order to generate the entangled state. Next, we transfer the condensate onto the “test” system which possesses its own identical anisotropic trap (same value of A) rotating with the “test” system at frequency Ω_T . Alternatively, we can think of the mechanism that rotates the anisotropic trap as being switched off as the condensate plus the trap get transferred to the “test” system, where the anisotropic trap couples to the rotating system and acquires the same rotation rate Ω_T . In either case, the net effect is that of the condensate now being trapped in an anisotropic potential which is rotating at frequency Ω_T instead of Ω_c . Any small mismatch between Ω_T and Ω_c due to the initial uncertainty $\delta\Omega_T$ produces a very fast (non-adiabatic) change of the condensate’s rotation frequency from Ω_c to Ω_T . Consequently, the quantum state of the system right after transferring the condensate to the “test” system is

$$|\Psi(\Omega_c)\rangle \longrightarrow a(\Omega_T)|\Psi_0(\Omega_T)\rangle + b(\Omega_T)|\Psi_1(\Omega_T)\rangle, \quad (5.15)$$

5.3 Non-adiabatic rotation frequency shift and Phase accumulation

where $|\Psi_0(\Omega_T)\rangle$ and $|\Psi_1(\Omega_T)\rangle$ are the two lowest eigenstates of \hat{H} at Ω_T . We assume that the mismatch between Ω_T and Ω_c is always small enough so that the quick shift in rotation frequency produces a negligible population of higher excited states and allows us to describe the many-body wave function as a two-level system. This two-level requirement is an integral assumption of our proposed interferometric scheme, and we made sure that in simulations we always operate in a regime where it is satisfied. Once the condensate has been transferred to the “test” system, we allow it to undergo a free time evolution in order to accumulate a phase between the two eigenstates. After a waiting time τ , the quantum state of the system is

$$|\Psi(\Omega_T)\rangle = a(\Omega_T)e^{-iE_0(\Omega_T)\tau}|\Psi_0(\Omega_T)\rangle + b(\Omega_T)e^{-iE_1(\Omega_T)\tau}|\Psi_1(\Omega_T)\rangle, \quad (5.16)$$

where $E_0(\Omega_T)$ and $E_1(\Omega_T)$ are respectively the ground state and first excited state energy at Ω_T . We can see from this expression that the rotation frequency Ω_T has been intricately “encoded” into the final state $|\Psi(\Omega_T)\rangle$, as opposed to conventional interferometric schemes where the parameter to be estimated is usually encoded only in the phase between the basis states appearing in the superposition and not in the coefficients or the basis states themselves. Hence, we might expect some of the usual intuition not to apply in our case. From here, we need to devise a measurement scheme that allows us to extract the information about Ω_T contained in the quantum state represented by Eq.(5.16). Therefore, it is important to find out the best precision possible with which Ω_T can be estimated from Eq.(5.16), regardless of the measurement scheme. As customary, we proceed to calculate the quantum Fisher information F_Q from Eq.(5.16).

In order to simplify the calculation and analysis of F_Q , we rewrite Eq.(5.16) in terms of a fixed basis $\{|\Psi_0(\Omega_0)\rangle, |\Psi_1(\Omega_0)\rangle\}$, which consists of the two lowest eigenstates of \hat{H} at the arbitrary rotation frequency Ω_0 . These eigenvectors do not depend on Ω_T by definition, and we assume that Ω_0 is such that we can write $|\Psi_0(\Omega_T)\rangle$ and $|\Psi_1(\Omega_T)\rangle$ in terms of these two levels only; this is always possible as long as $|\Psi(\Omega_T)\rangle$ is also a two-level state. In this fixed basis, the state in Eq.(5.16) can be expressed as

$$|\Psi(\Omega)\rangle = e^{-iE_0(\Omega)\tau} [a_0(\Omega)|\Psi_0(\Omega_0)\rangle + b_0(\Omega)|\Psi_1(\Omega_0)\rangle] + e^{-iE_1(\Omega)\tau} [a_1(\Omega)|\Psi_0(\Omega_0)\rangle + b_1(\Omega)|\Psi_1(\Omega_0)\rangle], \quad (5.17)$$

5.3 Non-adiabatic rotation frequency shift and Phase accumulation

where we wrote Ω instead of Ω_T for notational convenience. We now use this expression to calculate the quantum Fisher information evaluated at the particular rotation frequency Ω_0 . First we obtain the derivative of Eq.(5.17) with respect to Ω

$$\begin{aligned} \left. \frac{\partial |\Psi(\Omega)\rangle}{\partial \Omega} \right|_{\Omega_0} &= \left[(-i\tau \dot{E}_0 a_0 + \dot{a}_0) e^{-iE_0\tau} + \dot{b}_0 e^{-iE_1\tau} \right] |\Psi_0(\Omega_0)\rangle \\ &+ \left[(-i\tau \dot{E}_1 b_1 + \dot{b}_1) e^{-iE_1\tau} + \dot{a}_1 e^{-iE_0\tau} \right] |\Psi_1(\Omega_0)\rangle, \end{aligned} \quad (5.18)$$

where we have dropped the functional dependence with Ω for further clarity, and we have used the fact that $b_0(\Omega_0) = a_1(\Omega_0) = 0$. Therefore, we have

$$\langle \Psi'(\Omega_0) | \Psi'(\Omega_0) \rangle = \left| -i\tau \dot{E}_0 a_0 + \dot{a}_0 + \dot{b}_0 e^{-i\Delta E_{10}\tau} \right|^2 + \left| -i\tau \dot{E}_1 b_1 + \dot{b}_1 + \dot{a}_1 e^{i\Delta E_{10}\tau} \right|^2, \quad (5.19)$$

where $\Delta E_{10} = E_1 - E_0$. Now, using Eq.(5.18), we obtain

$$\begin{aligned} |\langle \Psi'(\Omega_0) | \Psi(\Omega_0) \rangle|^2 &= \left| (-i\tau \dot{E}_0 a_0 + \dot{a}_0) a_0^* + (-i\tau \dot{E}_1 b_1 + \dot{b}_1) b_1^* \right. \\ &\quad \left. + a_0^* \dot{b}_0 e^{-i\Delta E_{10}\tau} + b_1^* \dot{a}_1 e^{i\Delta E_{10}\tau} \right|^2. \end{aligned} \quad (5.20)$$

Finally, combining Eq.(5.19) and Eq.(5.20), the quantum Fisher information is given by

$$\begin{aligned} \frac{1}{4} F_Q [|\Psi(\Omega_0)\rangle] &= \left| -i\tau \dot{E}_0 a_0 + \dot{a}_0 \right|^2 |b_1|^2 + \left| -i\tau \dot{E}_1 b_1 + \dot{b}_1 \right|^2 |a_0|^2 \\ &\quad - \left| a_0^* \dot{b}_0 e^{-i\Delta E_{10}\tau} + b_1^* \dot{a}_1 e^{i\Delta E_{10}\tau} \right|^2 \\ &\quad + |\dot{a}_1|^2 + |\dot{b}_0|^2 + Q(\Omega_0; \tau), \end{aligned} \quad (5.21)$$

where

$$\begin{aligned} Q(\Omega_0; \tau) &= 2\text{Re} \left\{ \left(-i\tau \dot{E}_0 a_0 + \dot{a}_0 \right) \dot{b}_0^* e^{i\Delta E_{10}\tau} + \left(-i\tau \dot{E}_1 b_1 + \dot{b}_1 \right)^* \dot{a}_1 e^{i\Delta E_{10}\tau} \right. \\ &\quad - \left(a_0 \dot{b}_0^* e^{i\Delta E_{10}\tau} + b_1 \dot{a}_1^* e^{-i\Delta E_{10}\tau} \right) \left(-i\tau \dot{E}_0 a_0 + \dot{a}_0 \right) a_0^* \\ &\quad - \left(a_0 \dot{b}_0^* e^{i\Delta E_{10}\tau} + b_1 \dot{a}_1^* e^{-i\Delta E_{10}\tau} \right) \left(-i\tau \dot{E}_1 b_1 + \dot{b}_1 \right) b_1^* \\ &\quad \left. - \left(\dot{a}_0^* + i\tau \dot{E}_0 a_0^* \right) \left(-i\tau \dot{E}_1 b_1 + \dot{b}_1 \right) a_0 b_1^* \right\}. \end{aligned} \quad (5.22)$$

Ideally, we would like to numerically study the coefficients a_0, a_1, b_0, b_1 and their derivatives in order to find the optimal set of parameters of the system such

5.3 Non-adiabatic rotation frequency shift and Phase accumulation

as g , A or γ , that maximise F_Q in Eq.(5.21). However, this task is quite involved and very demanding in computational terms, thus it was impractical to pursue it with our current computational facilities. Nevertheless, we heuristically studied the Fisher information in Eq.(5.21) for an educated selection of parameters for which we expected to observe sub-shot-noise signature in our proposed interferometric scheme, guided by the theoretical and numerical evidence we previously gathered. The heuristic approach starts with studying the functional dependence of the Fisher information in Eq.(5.21) with the waiting time τ . This expression is of the form

$$\tilde{A}\tau^2 + \tilde{B}\tau + \tilde{C} + (\tilde{D}\tau + \tilde{E}) \sin(\Delta E_{10}\tau) + (\tilde{F}\tau + \tilde{G}) \cos(\Delta E_{10}\tau), \quad (5.23)$$

where the set of coefficients $\{\tilde{A}, \tilde{B}, \dots, \tilde{G}\}$ depends in general on N, g, A, γ and Ω_0 . This expression is a parabola in τ with oscillations superimposed on it, coming from the sine and cosine terms, and the amplitude of the oscillations increases with τ . This functional dependence lends itself to consider two different regimes for its study; the regime of long waiting times where the quadratic term in Eq.(5.23) is the leading term and the oscillations become less relevant for the determination of the Fisher information, and the regime of short waiting times, for which the oscillations play an important role in the exact determination of the Fisher information and its scaling with N . We study these two regimes in the following sections.

5.3.1 Long waiting time regime

We now focus on the regime of long waiting times where the expression for F_Q greatly simplifies. For large τ , determined by the relative magnitude of \tilde{A} compared to those of \tilde{D} and \tilde{F} , the order of magnitude of F_Q in Eq.(5.21) is given by the leading term $a\tau^2$, which after some algebra can be shown to be

$$F_Q [|\Psi(\Omega_0)\rangle; \tau \gg 1] = 4 (|b_1(\Omega_0)|^2 - |b_1(\Omega_0)|^4) \left(\left. \frac{\partial(\Delta E_{10}(\Omega))}{\partial\Omega} \right|_{\Omega_0} \right)^2 \tau^2. \quad (5.24)$$

This expression is very handy since it allows us to approximately calculate F_Q for large τ without actually needing to simulate a time evolution, which can take

5.3 Non-adiabatic rotation frequency shift and Phase accumulation

up to 26 hours per simulated second for $N = 10$ and two Landau levels using a standard double-core PC. We only need to simulate the diabatic frequency shift in order to obtain $|b_1(\Omega_0)|^2$, which is the probability amplitude of the condensate being in the first excited state at frequency Ω_0 . The simulation time for the diabatic jump is typically of the order of minutes for $N \leq 14$. We now present results using Eq.(5.24) for large τ . In the next section, we present results for the other regime of small waiting times where a full numerical calculation was used to obtain F_Q .

We have numerically calculated the final many-body state of the system right after a different number of values of the diabatic frequency shift for $N = 6, 8, \dots, 14$. Since it is necessary to remain in a two-level approximation for Eq.(5.24) to be valid, we have estimated the largest frequency shift Ω_{\max} compatible with this requirement simultaneously for all $N \leq 14$, using the same rotation frequency gradient $\gamma = 0.46 \times 10^2$. Thus, all calculations were done for frequency shifts below Ω_{\max} . This maximum value for the frequency shift depends on g , but it is of the order of 3×10^{-3} for all cases considered here. Also, we have checked that the resulting $F_Q[|\Psi(\Omega)\rangle; \tau \gg 1]$ has approximately the same value for all rotation frequency rates $\gamma \geq 0.46 \times 10^{-2}$. Below this value, the dynamics of the system enters the adiabatic regime, greatly reducing $|b_1(\Omega)|^2$ and consequently the Fisher information as calculated from Eq.(5.24). Additionally, instead of diabatically shifting away from the critical frequency Ω_c , we do it from the rotation frequency corresponding to the avoided crossing Ω_{\min} . This is due to the fact that $\partial(\Delta E_{10}(\Omega_{\min}))/\partial\Omega = 0$, meaning that shifting away from Ω_c to a rotation frequency which is very close to Ω_{\min} results in a rotation frequency precision that increases without bound as the frequency shift is closer to Ω_{\min} . The resulting discontinuity in $1/\sqrt{F_Q}$ at Ω_{\min} also means that $\tilde{A}\tau^2$ is no longer the leading term in Eq.(5.21) for nearby frequencies, except for extremely long waiting times. Nevertheless, since Ω_{\min} is extremely close to Ω_c , the entangled states at these two rotation frequencies are almost identical; as a result, the Fisher information has the same values for all the considered frequency shifts, except near the discontinuity, where shifting away from Ω_{\min} produces a larger value of the Fisher information and consequently a smaller lower bound for the precision of the rotation frequency.

5.3 Non-adiabatic rotation frequency shift and Phase accumulation

Before presenting the numerical results, it is convenient to make a remark about the Heisenberg and Standard Quantum limits in this context. Since the parameter we want to estimate is not a dimensionless phase, but rather a rotation rate which has units that can be scaled, benchmarking against a perfect $N00N$ state does not necessarily mean comparing the rotation rate precision to $1/N$ as it would be done for phase precision. In order to establish the benchmark for the best possible precision using a perfect $N00N$ state, we compare against the state obtained as

$$|N, 0\rangle \rightarrow QBS \rightarrow \text{Free Time Evolution } \tau \rightarrow \frac{1}{\sqrt{2}} \left(|N, 0\rangle + e^{-iN\Delta E^{(\text{sp})}(\Omega)\tau} |0, N\rangle \right), \quad (5.25)$$

where the two modes correspond to the two lowest single-particle energy levels $\psi_{m=0}$ and $\psi_{m=1}$, $\Delta E^{(\text{sp})}(\Omega)$ is the corresponding energy gap between these two levels, QBS is a quantum beam splitter operation described in chapter 2, which transforms $|N, 0\rangle$ into a $N00N$ state superposition, and the free time evolution is done taking $g = 0$ so that $|N, 0\rangle$ and $|0, N\rangle$ are eigenstates of the Hamiltonian with energies $NE_{m=0}$ and $NE_{m=1}$ respectively. Therefore, the rotation frequency precision for Eq.(5.25) is given by

$$\Delta\Omega \geq \frac{1}{\tau N \left| \frac{\partial(\Delta E^{(\text{sp})})}{\partial\Omega} \right|} = \frac{1}{\tau N}, \quad (5.26)$$

since $|\partial(\Delta E^{(\text{sp})})/\partial\Omega| = 1$ for all $\Omega \leq 1$, as readily obtained from Eq.(3.35). This is our benchmark for Heisenberg-limited precision. In the same way, if we think of N independent particles in mode $\psi_{m=0}$ passing through a normal beam splitter and then picking up a phase as a result of a free time evolution with $g = 0$, the resulting precision for these unentangled particles can be shown to be

$$\Delta\Omega \geq \frac{1}{\tau\sqrt{N}}. \quad (5.27)$$

This is the standard quantum limit for a measurement of Ω in our case. For comparison purposes, we have taken $\tau = 1$ in Eqs.(5.27),(5.25) and (5.24) for all cases.

We first present results for the case $g = (6/N) \times 1.0$. As we saw in chapter 4, this regime corresponds to $N00N$ -like entangled states at the critical frequency.

5.3 Non-adiabatic rotation frequency shift and Phase accumulation

The interferometric scheme was designed in such a way that we expected to observe sub-shot noise behavior for this regime at the very least. We show the obtained lower bound for the rotation frequency precision and the relevant quantities that determine the Fisher information from Eq.(5.24) in Figs.(5.6) and (5.7). We found that the best possible rotation frequency precision for any frequency shift in the range $[-3.9 \times 10^{-3}, -8.0 \times 10^{-4}]$ nearly saturates the Heisenberg limit for all $N \leq 14$. This means that any initial rotation frequency mismatch between the “test” system and the condensate “probe” in this interval can be measured with sub-shot noise precision for any number of atoms $N \leq 14$. For smaller diabatic frequency jumps than $\times 10^{-5}$, we progressively lose sub-shot noise sensitivity, the smaller number of atoms being the first to lose it.

In contrast, the bat-like regime with $g = (6/N) \times 0.4$ does not show any sub-shot noise behavior at all as can be seen in Fig. (5.9). These results are not promising for quantum enhanced metrology using this scheme. Nevertheless, it will be shown in the next section that sub-shot noise behavior is achieved in the opposite regime of small waiting times under certain circumstances. In view of these results, it is natural to consider the case which is halfway between the bat-like state and the $N00N$ -like one. We show the numeric results for this case with $g = (6/N) \times 0.7$ in Figs.(5.10) and (5.11). This time we recover sub-shot noise behavior for all $N \leq 14$ in a smaller frequency window $[-2 \times 10^{-3}, -1.2 \times 10^{-3}]$. Again, above -1.2×10^{-3} , the sub-shot noise behavior progressively disappears and it is completely lost for all $N \leq 14$ when the frequency shift is smaller than -1.6×10^{-4} . Even though the resulting precision is not as close to the Heisenberg limit as in the $N00N$ -like case, we have the added feature of the entangled state having some bat-like character that makes it more robust to particle loss.

Finally, we consider the relevant case of fixing the interaction strength to the same value for all numbers of atoms $N \leq 14$. In this case, the actual form of the entangled state varies with N . We chose a value of $g = 0.42$ which produces a bat-like state for $N = 6$ and a $N00N$ -like for $N = 14$. A smaller value than $g = 0.42$ degrades the overall rotation frequency precision, whereas for a much larger value we need more than two Landau levels in order to correctly describe the condensates with larger numbers of particles. Although we are not comparing like with like when it comes to the scaling of Fisher information, we still observe

5.3 Non-adiabatic rotation frequency shift and Phase accumulation

sub-shot noise behavior as shown in Fig. (5.13). This parameter regime of g fixed can be of interest in experiments because we do not need to know the exact number of atoms in the condensate in order to tune the interaction strength to obtain sub-shot noise behavior.

In the following section, we study the opposite regime of short waiting times which exhibits striking differences with the case that we have just analysed in this section.

5.3 Non-adiabatic rotation frequency shift and Phase accumulation

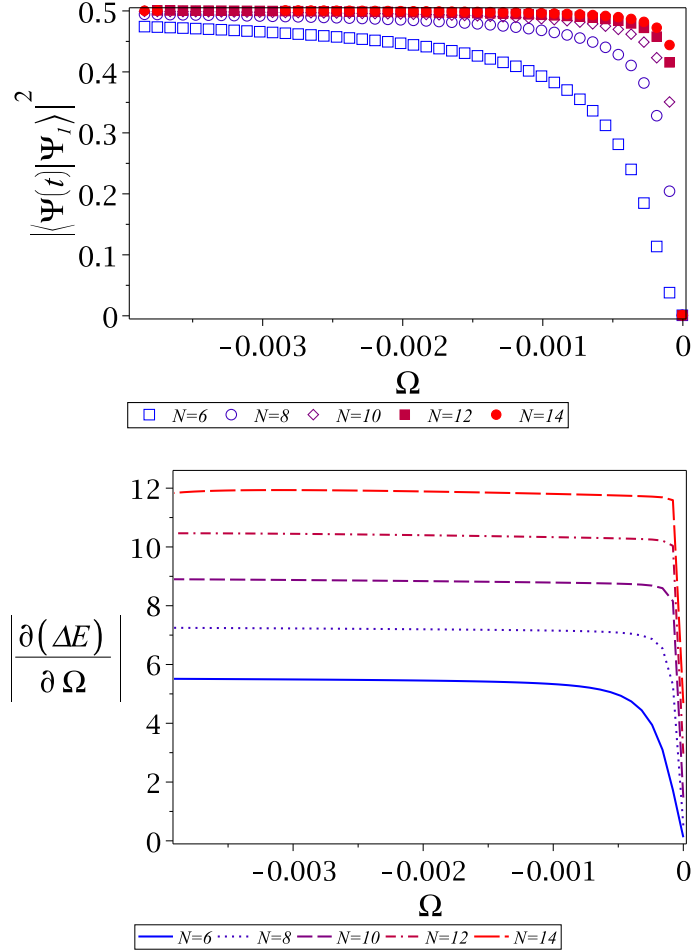


Figure 5.6: Analysis of the factors determining the Fisher information in the regime of $\tau \gg 1$ using two Landau levels for $g = (6/N) \times 1.0$ and $\gamma = 0.46 \times 10^2$ for all cases. (Top) Magnitude of the coefficient $|b_1(\Omega)|^2$ in function of Ω , the frequency shift measured from Ω_{\min} , as obtained from projecting the evolved state $|\Psi(t)\rangle$ onto the static first excited state after the diabatic frequency jump. (Bottom) Gradient of the energy gap between the GS and the first excited state as a function of the frequency shift. In both cases, the range of the frequency shift has been calculated to be the maximum value of Ω for which the population in the two lowest eigenstates of the many-body system remains larger than 0.99 for all $N \leq 14$.

5.3 Non-adiabatic rotation frequency shift and Phase accumulation

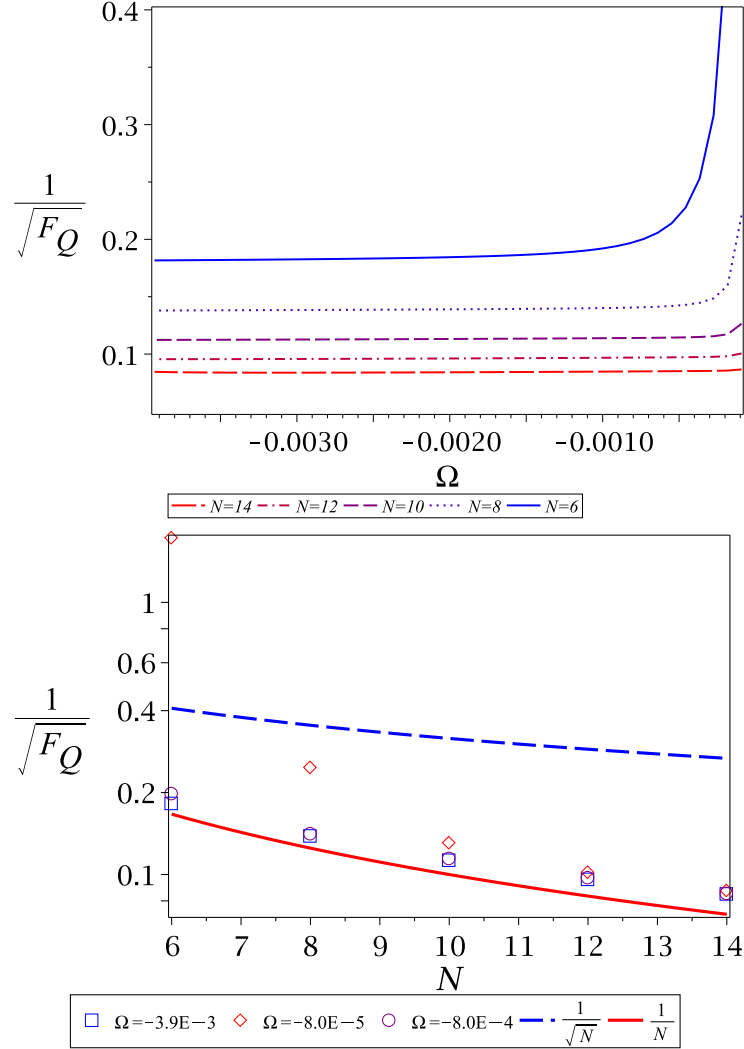


Figure 5.7: Analysis of the quantum Fisher information in the regime of $\tau \gg 1$ using two Landau levels for $g = (6/N) \times 1.0$ and $\gamma = 0.46 \times 10^2$ for all cases. (Top) Lower bound for the precision of the frequency shift as a function of Ω , given by the Crámer-Rao inequality. (Bottom) Scaling of the lower bound for the precision of the frequency shift with number of atoms N for three different values of the frequency shift across the considered range. The blue empty box data corresponds to the maximum possible value of the frequency shift compatible with a two-level approximation for all $N \leq 14$. Notice the logarithmic scale for this plot.

5.3 Non-adiabatic rotation frequency shift and Phase accumulation

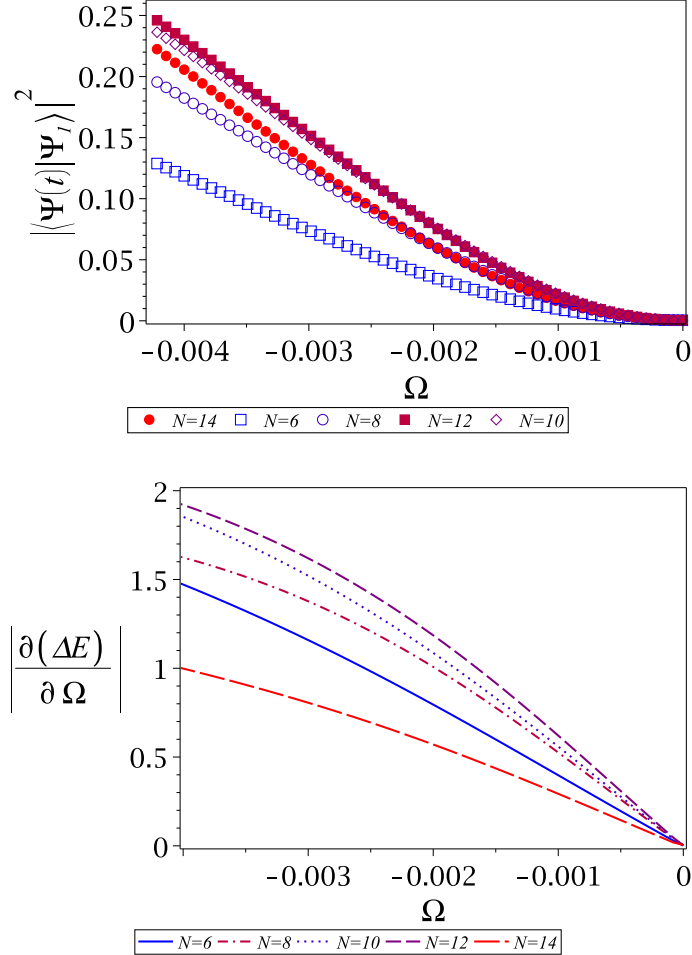


Figure 5.8: Analysis of the factors determining the Fisher information in the regime of $\tau \gg 1$ using two Landau levels for $g = (6/N) \times 0.4$ and $\gamma = 0.46 \times 10^2$ for all cases. (Top) Magnitude of the coefficient $|b_1(\Omega)|^2$ in function of Ω , the frequency shift measured from Ω_{\min} , as obtained from projecting the evolved state $|\Psi(t)\rangle$ onto the static first excited state after the diabatic frequency jump. (Bottom) Gradient of the energy gap between the GS and the first excited state as a function of the frequency shift. In both cases, the range of the frequency shift has been calculated to be the maximum value of Ω for which the population in the two lowest eigenstates of the many-body system remains larger than 0.99 for all $N \leq 14$.

5.3 Non-adiabatic rotation frequency shift and Phase accumulation

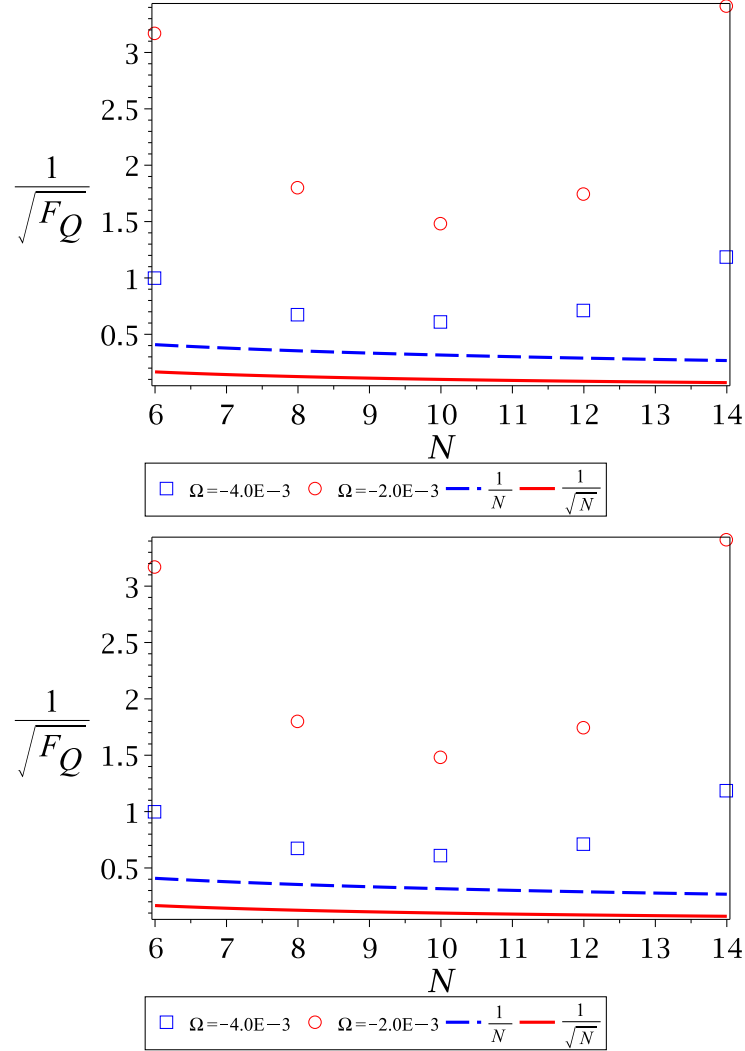


Figure 5.9: Analysis of the quantum Fisher information in the regime of $\tau \gg 1$ using two Landau levels for $g = (6/N) \times 0.4$ and $\gamma = 0.46 \times 10^2$ for all cases. (Top) Lower bound for the precision of the frequency shift as a function of Ω , given by the Crámer-Rao inequality. (Bottom) Scaling of the lower bound for the precision of the frequency shift with number of atoms N for two different values of the frequency shift across the considered range. The blue empty box data corresponds to the maximum possible value of the frequency shift compatible with a two-level approximation for all $N \leq 14$.

5.3 Non-adiabatic rotation frequency shift and Phase accumulation

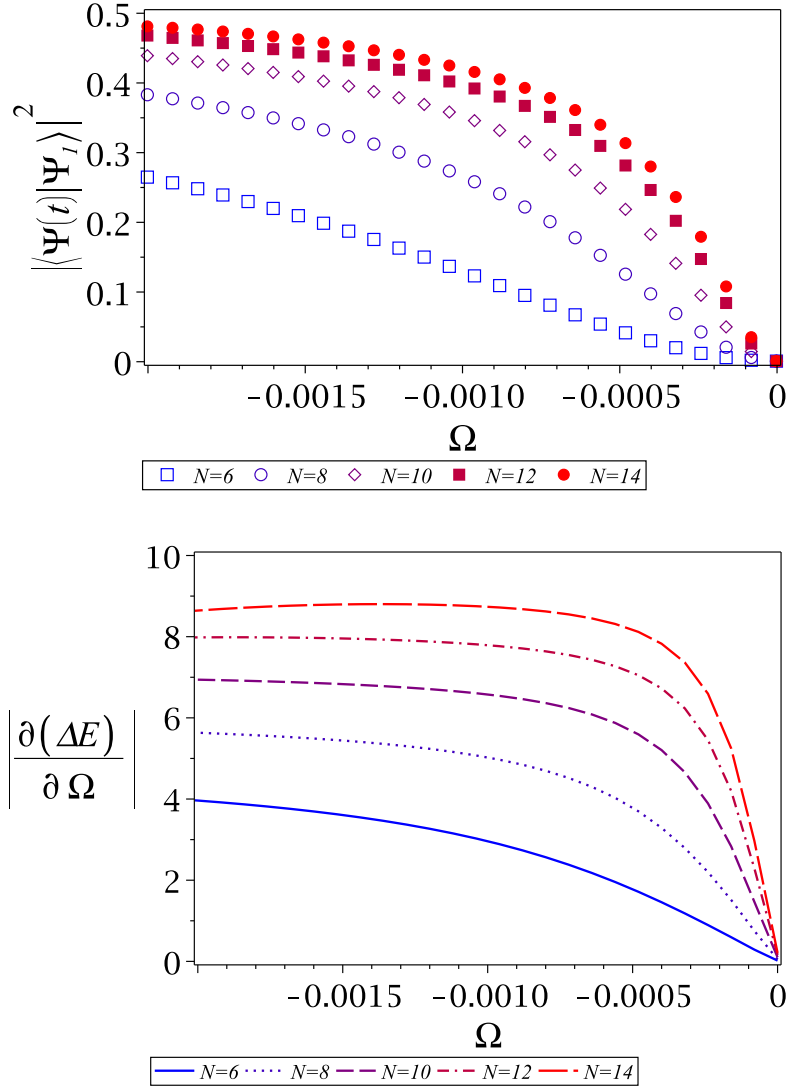


Figure 5.10: Analysis of the factors determining the Fisher information in the regime of $\tau \gg 1$ using two Landau levels for $g = (6/N) \times 0.7$ and $\gamma = 0.46 \times 10^2$ for all cases. (Top) Magnitude of the coefficient $|b_1(\Omega)|^2$ in function of Ω , the frequency shift measured from Ω_{\min} , as obtained from projecting the evolved state $|\Psi(t)\rangle$ onto the static first excited state after the diabatic frequency jump. (Bottom) Gradient of the energy gap between the GS and the first excited state as a function of the frequency shift. In both cases, the range of the frequency shift has been calculated to be the maximum value of Ω for which the population in the two lowest eigenstates of the many-body system remains larger than 0.99 for all $N \leq 14$.

5.3 Non-adiabatic rotation frequency shift and Phase accumulation

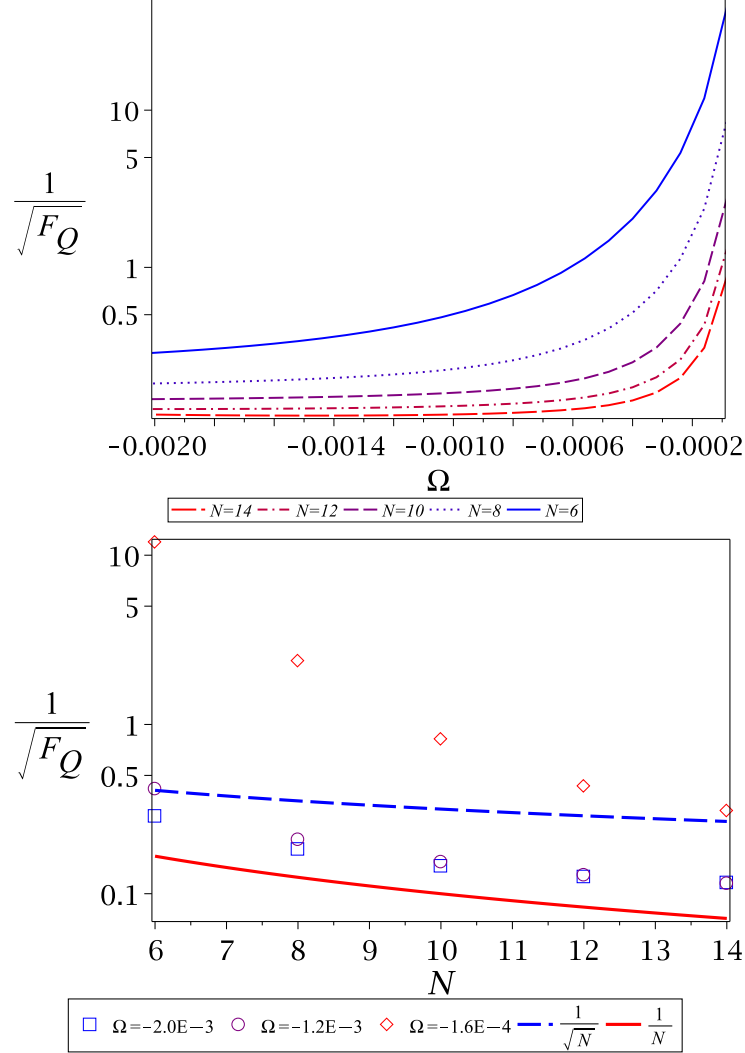


Figure 5.11: Analysis of the quantum Fisher information in the regime of $\tau \gg 1$ using two Landau levels for $g = (6/N) \times 0.7$ and $\gamma = 0.46 \times 10^2$ for all cases. (Top) Lower bound for the precision of the frequency shift as a function of Ω , given by the Crámer-Rao inequality. (Bottom) Scaling of the lower bound for the precision of the frequency shift with number of atoms N for three different values of the frequency shift across the considered range. The blue empty box data corresponds to the maximum possible value of the frequency shift compatible with a two-level approximation for all $N \leq 14$. Notice the logarithmic scale in both plots.

5.3 Non-adiabatic rotation frequency shift and Phase accumulation

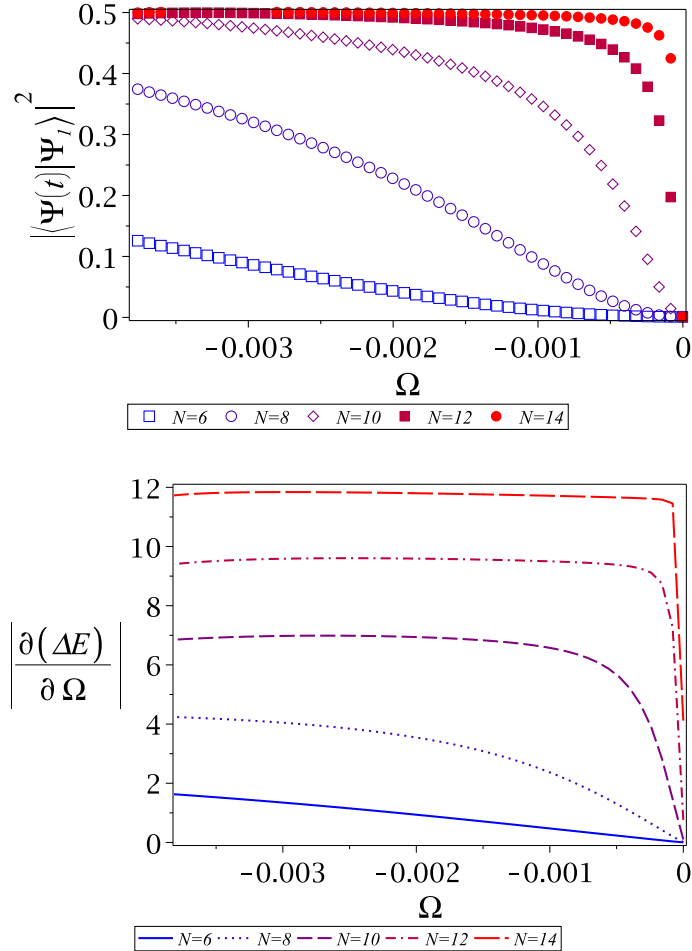


Figure 5.12: (Top) Magnitude of the coefficient $|b_1(\Omega)|^2$ in function of Ω , the frequency shift measured from Ω_{\min} , as obtained from projecting the evolved state $|\Psi(t)\rangle$ onto the static first excited state after the diabatic frequency jump. (Bottom) Gradient of the energy gap between the GS and the first excited state as a function of the frequency shift. In both cases, the range of the frequency shift has been calculated to be the maximum value of Ω for which the population in the two lowest eigenstates of the many-body system remains larger than 0.99 for all $N \leq 14$.

5.3 Non-adiabatic rotation frequency shift and Phase accumulation

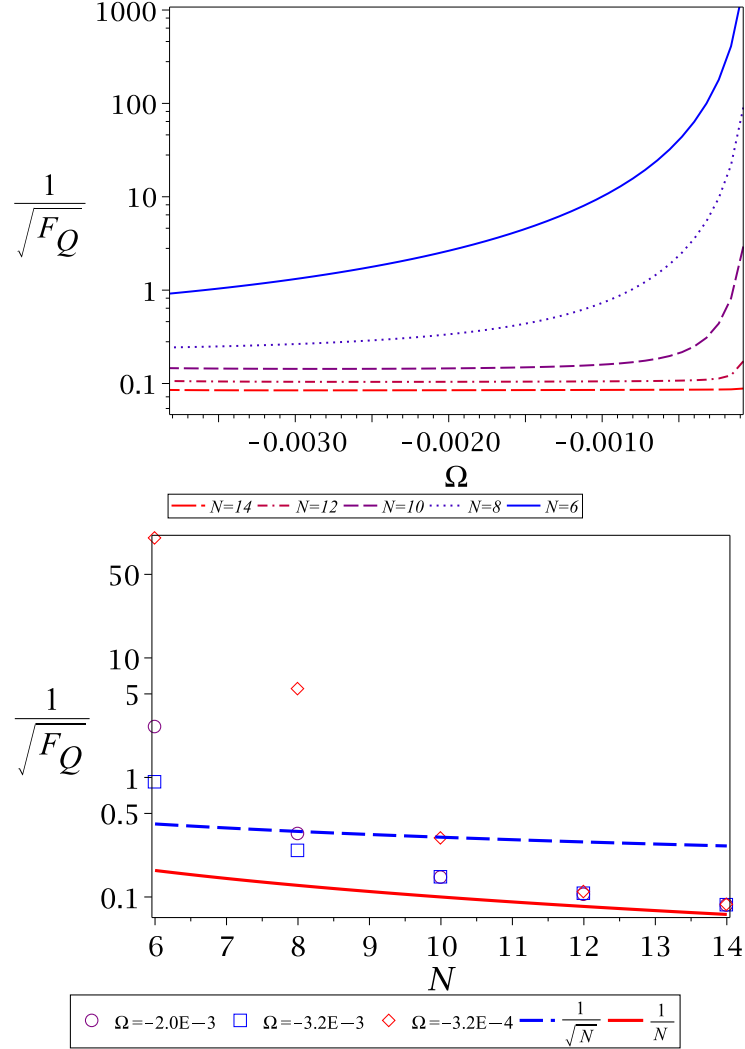


Figure 5.13: Analysis of the quantum Fisher information in the regime of $\tau \gg 1$ using two Landau levels for a fixed value of $g = 0.42$ and $\gamma = 0.46 \times 10^2$ for all cases. (Top) Lower bound for the precision of the frequency shift as a function of Ω , given by the Crámer-Rao inequality. (Bottom) Scaling of the lower bound for the precision of the frequency shift with number of atoms N for three different values of the frequency shift across the considered range. The blue empty box data corresponds to the maximum possible value of the frequency shift compatible with a two-level approximation for all $N \leq 14$. Notice the logarithmic scale in both plots.

5.3 Non-adiabatic rotation frequency shift and Phase accumulation

5.3.2 Short waiting time regime

Now we turn to the case of short waiting times. In this case we calculate the quantum Fisher information by performing a full numerical evaluation using

$$F_Q[|\Psi(\Omega_0; \tau)\rangle] = 4 \left[\langle \Psi'(\Omega_0; \tau) | \Psi'(\Omega_0; \tau) \rangle - |\langle \Psi'(\Omega_0; \tau) | \Psi(\Omega_0; \tau) \rangle|^2 \right], \quad (5.28)$$

where the state $|\Psi(\Omega_0; \tau)\rangle$ is obtained as

$$|\Psi(\Omega_{\min})\rangle \rightarrow \begin{array}{c} \text{Frequency Shift} \\ \text{to } \Omega_0 \end{array} \rightarrow |\Psi(\Omega_0; \tau = 0)\rangle \rightarrow \begin{array}{c} \text{Free Time} \\ \text{Evolution} \end{array} \rightarrow |\Psi(\Omega_0; \tau)\rangle, \quad (5.29)$$

and its derivative approximated as

$$|\Psi'(\Omega_0; \tau)\rangle \approx \frac{|\Psi(\Omega_0 + \delta\Omega; \tau)\rangle - |\Psi(\Omega_0; \tau)\rangle}{\delta\Omega}. \quad (5.30)$$

The value of $\delta\Omega = 1 \times 10^{-5}$ has been fixed in simulations in order to ensure convergence of the approximation to the derivative within numeric precision. Due to computational constraints, we have restricted the simulations to waiting times of 2400 units for $N = 6$, 1200 for both $N = 8$ and $N = 10$, and only 10 units for $N > 10$. Nevertheless, these simulations provide sufficient evidence to assess the suitability of the system for sub-shot noise behavior in the short waiting time regime.

The first thing we address using the full numerical calculation is the estimation of the order of magnitude of τ_L for which the long waiting time regime is reached. In order to estimate τ_L , we found a best fit for the Fisher information using the functional form of Eq.(5.23), after which the fractional error of approximating F_Q with Eq.(5.24) was calculated, defining τ_L as the waiting time for which the fractional error is $\sim 5\%$. For this purpose, we focused on two different values of the rotation frequency shift. The first one, $\Delta\Omega = -3.0 \times 10^{-3}$, for which the two-level approximation ceases to be a good description below this value, and the second one $\Delta\Omega = -3.0 \times 10^{-4}$, which represents exceedingly small frequency shifts that would happen as a result of the “probe” system being almost on resonance with respect to the “test” system. We show in Fig. (5.14) the Fisher information as obtained from the full numerical calculations along with the best fit, and the

5.3 Non-adiabatic rotation frequency shift and Phase accumulation

fractional error of the quadratic approximation for the case of $g = (6/N) \times 0.44$ and $\Delta\Omega = -3 \times 10^{-3}$. In this case, the long waiting time regime is reached when $\tau_L > 5 \times 10^3$ (~ 4 s) for $\Delta\Omega = -3.0 \times 10^{-3}$, and $\tau_L > 6 \times 10^5$ (~ 454 s) for $\Delta\Omega = -3 \times 10^{-4}$, where the time in seconds is calculated using $\omega_\perp = 2\pi \times 210$ Hz. The fact that τ_L increases as the frequency shift decreases can be understood as a consequence of $|b_1(\Omega)|^2$ and $|\partial(\Delta E)/\partial\Omega|$ becoming increasingly small as the frequency shift is reduced. As a result, the magnitude of the quadratic term in the Fisher information decreases, whereas the magnitude of the oscillations remains of the same order. This means that τ needs to be larger in order for the quadratic term to become the leading term in F_Q .

In contrast, for $g = (6/N) \times 1.0$, the long waiting time regime is reached when $\tau_L > 35$ (~ 26 ms) for $\Delta\Omega = -3.0 \times 10^{-3}$, and $\tau_L > 4 \times 10^4$ (~ 30 s) for $\Delta\Omega = -3 \times 10^{-4}$. Therefore, the long waiting time regime is reached faster as the interaction strength is increased. These results show that it takes a prohibitively long time to reach the results of the previous section when the frequency shift is very small. However, we see that for an interaction strength of $g \sim (6/N)$, we should be able to obtain sub-shot noise behavior for very small waiting times and for a wider range of frequency shifts as opposed to the case of very small g . Clearly, these results and the fact that we do not observe sub-shot noise behavior for bat-like states in the long waiting time regime are not very promising and prompt us to investigate the features of the system in the opposite regime. Fortunately, as we will shortly see, we obtain very promising results in the regime of short waiting times.

For waiting times much shorter than τ_L , the oscillations of the Fisher information as a function of the waiting time become more important for the determination of F_Q , and due to the fact that the frequency of the oscillations changes with N , the scaling of the Fisher information with N undergoes major fluctuations. Surprisingly, as τ becomes exceedingly small, where the system enters a regime for which F_Q locally increases in a monotonic way before reaching its first local maximum for all N , we observe sub-shot noise behavior for most configurations previously considered in this section, particularly for those that did not produce sub-shot noise results in the long waiting time regime.

5.3 Non-adiabatic rotation frequency shift and Phase accumulation

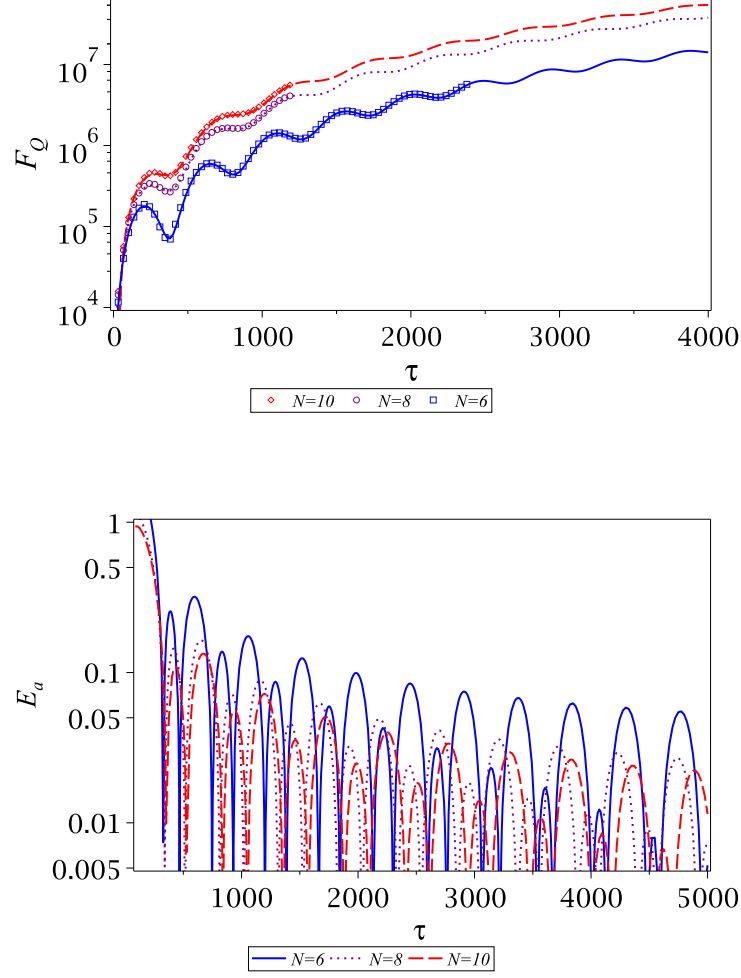


Figure 5.14: Full numeric calculation of the Fisher information for $g = (6/N) \times 0.44$ and a frequency shift of $\Delta\Omega = -3 \times 10^3$. The value $\gamma = 0.46 \times 10^2$ was used for all cases. (Top) The discrete symbols represent the actual results of a full numeric evaluation of the Fisher information, whereas the solid, dotted and dashed lines represent the best fit for the numeric results using the functional form of Eq.(5.23). (Bottom) The fractional error of approximating the Fisher information as obtained from the best fit $F_Q^{(\text{fit})}$ with the quadratic term in Eq.(5.24), $F_Q^{(\tau \gg 1)}$. Where $E_a = |F_Q^{(\text{fit})} - F_Q^{(\tau \gg 1)}| / F_Q^{(\text{fit})}$.

5.3 Non-adiabatic rotation frequency shift and Phase accumulation

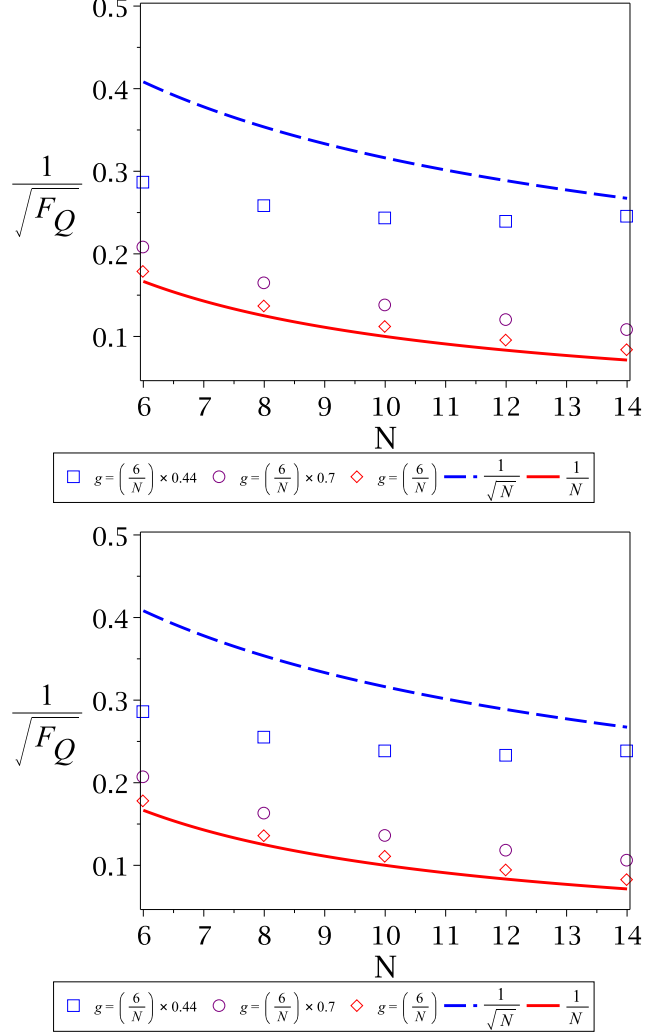


Figure 5.15: Full numeric calculation of the scaling of the lower bound for the rotation frequency precision with N for a different number of interaction strengths. The waiting time for the three sets of data is $\tau = 10$ and $\gamma = 0.46 \times 10^2$ for both panels. Also, the value of $1/\sqrt{F_Q}$ has been multiplied by τ (10 units in this case) for all sets of data for comparison purposes with the Heisenberg and the standard quantum limit. (Top) Rotation frequency precision for a frequency shift of $\Delta\Omega = -3 \times 10^{-5}$. (Bottom) Rotation frequency precision for a frequency shift of $\Delta\Omega = -3 \times 10^{-2}$.

5.3 Non-adiabatic rotation frequency shift and Phase accumulation

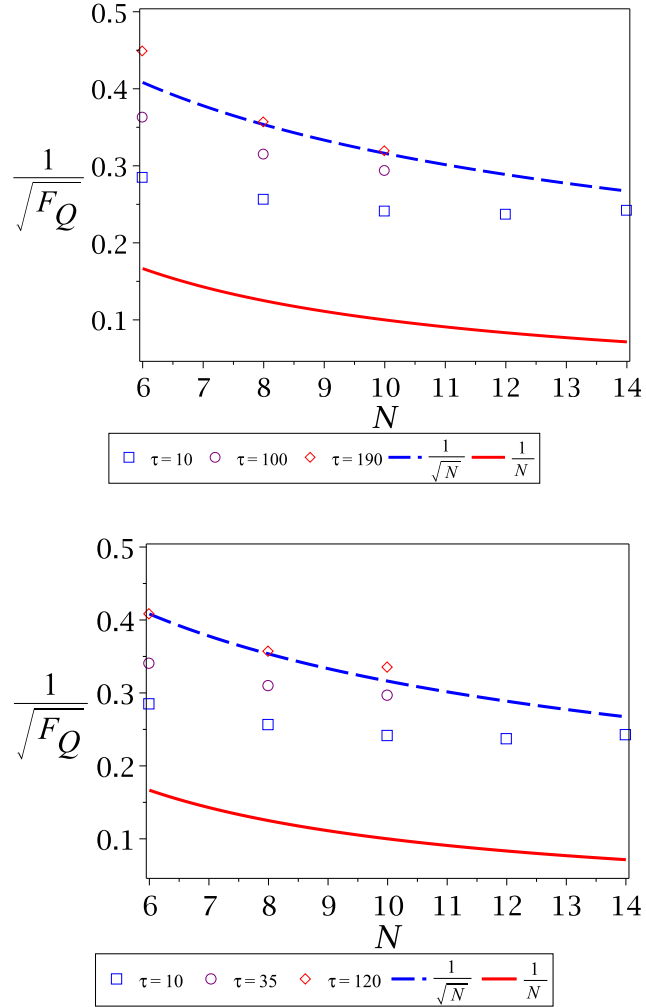


Figure 5.16: Full numeric calculation of the scaling of the lower bound for the rotation frequency precision with N for a different number of waiting times. The interaction strength is $g = (6/N) \times 0.44$ and $\gamma = 0.46 \times 10^2$ for both panels. Also, the value of $1/\sqrt{F_Q}$ has been multiplied by τ for all sets of data for comparison purposes with the Heisenberg and the standard quantum limit. (Top) Rotation frequency precision for a frequency shift of $\Delta\Omega = -3 \times 10^{-3}$. (Bottom) Rotation frequency precision for a frequency shift of $\Delta\Omega = -3 \times 10^{-4}$.

5.3 Non-adiabatic rotation frequency shift and Phase accumulation

In general, we found that for $\tau \approx 10$, quantum-limited precision is obtained for values of the interaction strength ranging from $g = (6/N) \times 0.44$ to $(6/N) \times 1.0$, and for a wide selection of different frequency shifts; these results are shown in Fig. (5.15). We only show results for the smallest and the largest frequency shift considered, $\Delta\Omega = -3 \times 10^{-5}$ and $\Delta\Omega = -3 \times 10^{-2}$ respectively. Nonetheless, we also calculated the Fisher information for two intermediate frequency shifts of $\Delta\Omega = -3 \times 10^{-4}$ and $\Delta\Omega = -3 \times 10^{-3}$, obtaining identical results as those shown in Fig. (5.15). We have used $\gamma = 0.46 \times 10^2$ to obtain these results but we have checked that identical outcomes are obtained for $\gamma \geq 0.46 \times 10^{-2}$. Notice, also, that we were able to calculate the precision of rotation measurements for frequency shifts as large as $\sim -3 \times 10^{-2}$, for which the population of higher states after the diabatic jump is not negligible, due to the fact that we are performing a full numeric calculation and hence, it does not rely on any two-level assumption.

Although we have not been able to calculate the Fisher information for $N > 14$, we surmise from the plots that the quantum-limited precision remains present even for condensates with a large number of atoms $N \gg 14$ for $g = (6/N) \times 1.0$. As the interaction strength is reduced to values of $g \sim (6/N) \times 0.44$, the scaling curve departs from $1/N$ and eventually meets the SQL one $1/\sqrt{N}$ for a certain maximum value of N . Thus, the sub-shot noise behavior is limited to a certain number of atoms depending on the exact form of the entangled state. The fact that the scaling curve for the Bat state in the long waiting time regime has a parabola shape, might indicate that in the short waiting time regime the scaling curve is also a wider parabola that continuously transforms into a narrower one as τ approaches τ_L , although we have not been able to prove this.

As τ increases the sub-shot noise behavior starts to degrade in different degrees depending on the exact value of the interaction strength. We show in Fig. (5.16) the case of $g = (6/N) \times 0.44$ for different short waiting times to depict this feature. It is important to know how long we can sustain sub-shot noise behavior for in the short waiting time regime in order to find the sensitivity of the scheme to inaccuracies in timing. Currently, this subject is under more detailed consideration and is an avenue for future research.

Remarkably, for a fixed number of particles and interaction strength, the magnitude of the Fisher information is almost independent of the frequency shift.

This can be understood in terms of the numeric approximation to F_Q as calculated using Eqs.(5.28), (5.29) and (5.30), which can be expressed as

$$F_Q [|\Psi(\Omega_0; \tau)\rangle] \approx \frac{4}{(\delta\Omega)^2} [1 - |\langle\Psi(\Omega_0; \tau)|\Psi(\Omega_0 + \delta\Omega; \tau)\rangle|^2], \quad (5.31)$$

for $\delta\Omega \ll 1$.

When we perform a very fast diabatic frequency shift from Ω_{\min} to Ω_0 followed by a free evolution with a small waiting time of $\tau \approx 10$, the overlap between $|\Psi(\Omega_{\min})\rangle$ and $|\Psi(\Omega_0)\rangle$ is very large because the state has hardly any time to change and the small waiting time does not make a substantial difference either. Thus, as a consequence of $|\Psi(\Omega_0)\rangle$ and $|\Psi(\Omega_0 + \delta\Omega)\rangle$ not being very different from $|\Psi(\Omega_{\min})\rangle$ for a very quick frequency shift as used in the simulations ($\gamma = 0.46 \times 10^2$), their overlap is large and hardly depends on the actual value of Ω_0 . Consequently, F_Q from Eq.(5.31) is also approximately independent of the frequency shift and its value is a small fraction of $4/(\delta\Omega)^2$. In a realistic scenario, however, it is unlikely that large constant values of γ can be achieved for large values of the frequency shift; therefore, these results will be limited to a certain frequency shift range in experiments.

On the other hand, we see from Eq.(5.31) that the Fisher information can be vastly increased if the overlap $\langle\Psi(\Omega_0; \tau)|\Psi(\Omega_0 + \delta\Omega; \tau)\rangle$ is reduced. This can be achieved by performing the frequency shift nearly adiabatically and close to the avoided crossing where the static ground state changes very rapidly with Ω . We have been able to observe this vast improvement in preliminary simulations and it is currently the basis of future research.

5.4 Conclusions

We have presented a promising interferometric scheme which enables us to engineer a range of entangled states from bat-like to N00N-like ones and obtain sub-shot noise precision for rotation measurements. The tunability of these states is easily achieved using Feshbach resonances to change the magnitude of the interaction strength between atoms. In a general way, the presented part of the scheme consists of three main steps. The first one is an adiabatic ramping of the

rotation frequency to bring the condensate to a critical frequency Ω_c , where the ground state is a highly entangled one. We analyzed the feasibility of this process and concluded that, with proper optimisation, a practical implementation should be possible for small numbers of atoms $N \sim 10$. In fact, this adiabatic ramping has been already demonstrated for $N \sim 5$ by (Gemmelke & Chu, 2010). However, it might be very challenging to create $N00N$ states due to the long nucleation times compared with the typical lifetime of condensates. Nevertheless, our recent results show that even for a non-perfect adiabatic nucleation, we are still able to get quantum enhancement for rotation measurements with a slight modification to our scheme. As a second step, the adiabatic nucleation is followed by a fast diabatic frequency shift which represents the coupling of our BEC “probe” with the “test” system. Then, a third step consists of a free evolution for a waiting time τ . Right after the free time evolution, the quantum Fisher information was calculated in order to assess the quantum enhancement in precision for the scheme.

Remarkably, we found sub-shot noise behavior for all the possible entangled states that can be produced with this scheme for waiting times of $\tau \sim 10$ (~ 8 ms). This enhancement is also independent of the magnitude of the frequency shift for a constant angular acceleration of $\gamma \geq 0.46 \times 10^{-3}$. For bat states with $g = (6/N) \times 0.44$, the sub-shot noise behavior is limited to a maximum number of atoms $N \sim 14$, whereas for a $N00N$ state with $g = (6/N) \times 1.0$, it does not seem to be limited to a certain maximum value of N . As τ increases, the quantum enhancement is degraded in different degrees depending on the exact form of the entangled state. Again, the $N00N$ state preserves the sub-shot noise behavior for long waiting times, whereas the bat state completely loses it. From here, an optimal read-out scheme needs to be engineered in order to reach the lower bound predicted by our results, and it will be addressed in future research.

In short, a promising set-up for the interferometric scheme was found for which quantum-limited precision can be achieved for a range of entangled states from bat states which are robust against particle losses to $N00N$ ones which achieve the highest precision. Finally, we showed that the set-up is amenable for experimental investigation and within reach of current technologies.

Chapter 6

Conclusions

In this chapter, we review the main results of the thesis in a compact and concise manner. Also, we discuss the ideas for future work, avenues of investigation, and some thoughts about improvements over our original ideas.

6.1 Summary

We started off by reviewing the concept of an interferometer and the ideas behind performing measurements in quantum physics in chapter 2. We introduced the concept of quantum Fisher information, which is a standard tool in quantum metrology that allows one to estimate the best precision possible in the measurement of an unknown parameter which is encoded in a particular quantum system using the Crámer-Rao inequality. This lower bound for the precision is independent of the measurement scheme, and theoretically, it is always possible to saturate the bound using a particular optimal read-out scheme, although finding such scheme is usually a difficult problem. Nevertheless, the lower bound that the Crámer-Rao inequality imposes, allows us to solely focus on optimizing the input state to an interferometer in order to attain the best performance that the interferometer is capable of, regardless of the details of the measurement process.

Calculating the quantum Fisher information, we saw that the best precision possible for measuring a linear phase with N unentangled particles scales as $\Delta\phi \sim 1/\sqrt{N}$, which is known as the shot-noise limit or the standard quantum limit of interferometry. This scaling is actually a pure statistical consequence of

classical random processes, as can be seen by invoking the central limit theorem. On the other hand, when the N particles are in a coherent $N00N$ superposition or “cat” state, which can be regarded as a maximally entangled state, the precision scales as $\Delta\phi \sim 1/N$, which is a massive $1/\sqrt{N}$ improvement over the unentangled case. This is the Heisenberg limit, which is believed to be the ultimate precision attainable by any linear interferometric scheme. In general, whenever the input state has some quantum correlations, it has the potential to show some improvement in phase precision over the unentangled case.

We then took a look at the details of particular interferometric schemes to produce some very well-known entangled states in the literature. In particular, the “bat” state was introduced, which was shown to attain nearly Heisenberg limited precision for large N . As opposed to $N00N$ states, the bat state performs much better in realistic scenarios thanks to its robustness against particle losses. Whereas for a $N00N$ state, the knowledge of the whereabouts of a single particle betrays the state in which the rest of them are, collapsing the wave function and destroying the entanglement, the large number variation in the bat state with particles distributed in different configurations over the two modes does not allow to obtain the which-way information of all the other particles when one particle is lost. Therefore, the bat state is better suited for practical implementations.

6.1.1 Main results

We introduced the system studied in this thesis in chapter 3, which is that of N bosons in a two-dimensional harmonic trap interacting through a contact potential whose strength is characterised by the dimensionless constant g . The N particles are set in rotation by with the aid of a rotating anisotropic trap whose strength is measured by $A \ll 1$.

In contrast to a classical fluid, a Bose–Einstein condensate does not acquire angular momentum when stirred until it reaches a particular rotation frequency Ω_1 , where a single quantized vortex is nucleated, and the system suddenly acquires $N\hbar$ units of angular momentum. When $A = 0$, the rotation frequency Ω_1 corresponds to the first energy crossing of the ground state, which has a $(N/2 + 1)$ -fold degeneracy. Then, the inclusion of a small anisotropy $A \ll 1$ lifts

the degeneracy, introducing a gap between the ground state and excited states, as well as an avoided crossing at the critical frequency Ω_c , which is roughly located at $\Omega_c \approx \Omega_1 + A$. Below this critical frequency, the ground state does not rotate and the macroscopic density profile shows a well localised peak at the centre of the trap, whereas above it, the ground state is a single vortex involving all the particles and the macroscopic density shows a sharp dip in the centre of the trap corresponding to the position of the vortex. Because the system always remains in the ground state, it must experience an abrupt symmetry-breaking change as it transits across the avoided crossing. As a consequence, the SPDM has two large eigenvalues at rotation frequencies close to Ω_c , corresponding to a macroscopic occupation of the two single-particle modes by all the bosons. Right at the critical frequency, these two modes have equal populations, heralding a failure of the mean-field description of the system, which in turn implies the existence of quantum correlations and entanglement between the particles. Notably, the form of the entangled state at Ω_c closely resembles the bat state which was introduced in chapter 2.

This symmetry-breaking process and the resulting entangled state at the threshold of the first vortex nucleation were first studied by (Dagnino *et al.*, 2009a), where they relied on the assumption of the system being well described by the lowest Landau level (LLL) approximation, which is valid in the case of weak interactions, and allows for a simplified and more tractable description of the rotating condensate. Under this assumption, the form of the entangled state and its Fisher information are practically invariant under changes in the interaction strength. However, the research carried out in this thesis has shown that these two properties of the ground state at Ω_c change dramatically when calculated with a more precise approximation that includes two Landau levels.

Up to the best of our knowledge, this is the first time that the nucleation of the first vortex in a non-axisymmetric rotating trap has been studied beyond the LLL approximation. Our first novel contribution regards the validity of the LLL approximation in this case. Within the two Landau level framework, we have demonstrated that, unlike the case calculated with a LLL approximation, the ground state at Ω_1 is only doubly degenerate, and the inclusion of a small anisotropy $A \ll 1$ has now a different consequence on the form of the entangled

ground state depending on the particular value of g . For a given value of the interaction strength g , there is a threshold value of the anisotropic strength $A_{\min}(g)$ for which the entangled ground state has a $N00N$ -like form when $A < A_{\min}(g)$. This $N00N$ -like form is in sharp contrast with the bat-like that is predicted by a LLL calculation. An even bigger disagreement is found for the quantum Fisher information as a function of Ω for these states. Whereas the bat state calculated with the LLL approximation has a relatively broad frequency width, the $N00N$ -like state has a Fisher information width that is roughly two orders of magnitude smaller than that of the bat state.

On the other hand, using two Landau levels, for a given value of g and a value of the anisotropy $A > A_{\min}(g)$, we qualitatively recover the LLL approximation results, i.e. a bat-like ground state and a broad Fisher information curve as a function of Ω . The smaller the interaction strength, the better the agreement with the LLL calculation. Particularly, for $gN/6 \approx 0.4$ and $A = 0.03$, the error of approximating the Fisher information using a LLL calculation is roughly of 10% with respect to a two Landau level calculation; also, the width is only twice as broad. A much better agreement with the LLL results is expected for values of $gN/6 < 0.4$; however, a proper study of this requires a larger basis with higher angular momentum states, since the ground state becomes very sensitive to the inclusion of these states when g is very small and thus the critical frequency is very close to the harmonic trap frequency.

In simpler terms, we have shown that, whereas the LLL approximation can identify reasonably the critical frequency or be sufficient for the purpose of studying symmetry breaking, it is vital to consider a larger basis that includes more Landau levels in order to identify the details of the produced entangled state and quantify the quantum Fisher information. As a consequence of this, a rich system is revealed that offers interesting opportunities for engineering different entangled states that range from bat-like to $N00N$ -like.

Our second novel contribution is that of an interferometric scheme proposal that takes advantage of these entangled states in order to achieve nearly Heisenberg limited precision for the measurement of rotations. We showed that, by adiabatically increasing the rotation frequency from $\Omega_0 \ll \Omega_c$, where the system is in the non-rotating ground state achieved by relaxation, all the way to Ω_c and

then performing a sudden rotation frequency shift to $\Omega_c \pm \Delta\Omega$, where we finally let the system evolve freely for a very short time $\tau \sim 8$ ms (when $\omega_{\perp} = 2\pi \times 210$ Hz), the lower bound for the precision of a measurement of $\Delta\Omega$ is nearly Heisenberg limited for the $N00N$ -like state, and sub-shot noise limited for the bat-like state, for all the numbers of particles that we were able to simulate ($N \leq 14$). Remarkably, the precision is independent of $\Delta\Omega$, provided that the diabatic rotation frequency jump is performed very quickly. This is interesting because it allows to measure both small and large rotations with almost the same precision.

All the necessary requirements to realise a proof-of-principle experiment of this proposal are within reach of current experimental technologies. Therefore, it is important to find an optimal read-out scheme that allows us to take advantage of the sub-shot noise precision in practice, before we test our ideas in the laboratory. Needless to say, this is one of the main avenues of future research that we are planning to pursue. In the next section, we discuss this idea and a few other ones which constitute areas of research that branch out of our current work for future consideration.

6.2 Future work

6.2.1 Read-out schemes

As it was mentioned before, it is necessary to find an optimal read-out scheme that achieves the predicted sub-shot noise lower bound of the precision for our interferometric scheme, before we can put our ideas to the experimental test. Although it is always theoretically possible to find a measurement process that saturates the lower bound given by the Crámer-Rao inequality for pure and mixed two-dimensional systems using a two-stage adaptive measurement procedure (Barndorff-Nielsen & Gill, 2000; Luati, 2004), in practice it might prove hard to realise it due to the fact that in general, only for rather special cases will a measurement exist that attains the precision calculated with the Fisher information for all values of the unknown parameter *simultaneously*. Also, there are many practical obstacles which can greatly degrade the precision and thus need to be circumvented, such as inefficiency in the detectors (Kim *et al.*, 1999).

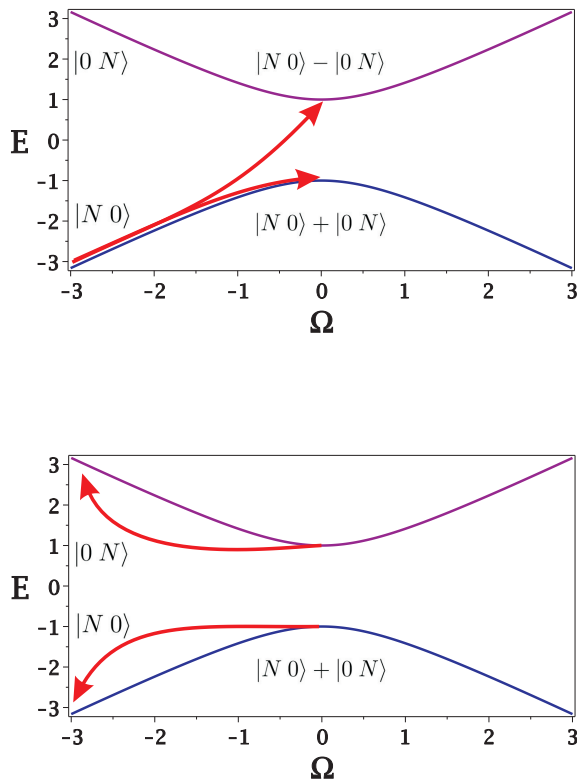


Figure 6.1: Non-adiabatic nucleation of the entangled state at the avoided crossing for the case of a $N00N$ state. (Top) A non-adiabatic evolution of the system populates both the ground state and the first excited state at the anticrossing, where the system is allowed to evolve for a time τ . (Bottom) A fast rotation frequency shift away from the anticrossing populates the states $|N0\rangle$ and $|0N\rangle$, and the system undergoes another free evolution which imprints a phase between these two eigenstates that is proportional to N .

Regarding this topic, we plan to investigate a possible read-out scheme that consists of undoing all the operations performed prior to the free time evolution, analogous to a standard Mach-Zender interferometer, to end up with the condensate in an accessible regime where we can measure the fraction of the atoms rotating and not rotating, which are expected to reflect an interference pattern from which $\Delta\Omega$ can be determined. Another idea that we would like to explore

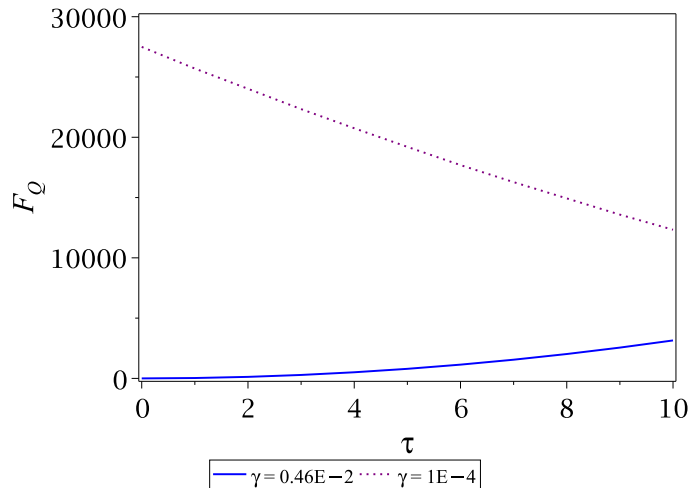


Figure 6.2: Fisher information obtained for two different angular acceleration values for $N = 6$ particles. The Fisher information is calculated for the state that results after shifting away the rotation frequency from the avoided crossing by an amount of 0.003. The calculation is obtained with two Landau levels, the interaction strength is $gN/6 = 1$, and the anisotropy $A = 0.03$.

in connection to the read-out procedure is the simulation of time-of-flight measurements, which are the typical standard way to probe BECs in experiments (Chevy *et al.*, 2000; Cooper, 2008; Dagnino *et al.*, 2009b; Fetter, 2009; Madison *et al.*, 2000a). We hope more ideas about how to measure the rotation shift can be revealed by studying the common way people make measurements on BECs.

6.2.2 Sub-shot noise precision without adiabatic nucleation of the entangled state

One of the most limiting features in our interferometric proposal is the need for nucleating the entangled state via an adiabatic ramping of the rotation frequency. As we saw in chapters 4 and 5, the energy gap between the ground state and the first excited state at the avoided crossing is exceedingly small already for small numbers of particles $N \sim 10$, which means that the adiabatic nucleation can take much longer than the lifetime of the condensate if the process is not optimized, and thus the whole scheme becomes impractical.

One possible way to circumvent this problem is by simply not insisting on having a perfect adiabatic nucleation of the entangled state. To see how this could work, consider the simplified picture of the nucleation of a cat state in Fig. (6.1). When the ground state at the avoided crossing is a $N00N$ state $(|N0\rangle + |0N\rangle)/\sqrt{2}$, the first excited state is orthogonal to it since they correspond to different eigenstates of the Hamiltonian. Without loss of generality, assume that the first excited state is $(|N0\rangle - |0N\rangle)/\sqrt{2}$. Now, if we start with the system in the ground state $|N0\rangle$ away from the anticrossing at $\Omega = \Omega_{\min} - \Delta\Omega$, a non-adiabatic evolution resulting from the ramping of Ω up to the rotation frequency of the avoided crossing will populate both the ground state and first excited state; at this point the state of the condensate is given by

$$|\Psi(\Omega_{\min})\rangle = \frac{a}{\sqrt{2}} (|N0\rangle - |0N\rangle) + \frac{b}{\sqrt{2}} (|N0\rangle + |0N\rangle). \quad (6.1)$$

Now, instead of immediately shifting away from this rotation frequency, we let the system evolve for a time τ at the avoided crossing, which introduces a phase $\Delta E_{\min}\tau$ between these two states. After this free evolution, we proceed as normal with the fast rotation frequency shift and another free evolution at $\Omega_{\min} - \Delta\Omega$, which in turn introduces another phase which can be thought as being equal to $N\phi$ for the $N00N$ state. Up to this point, the condensate is in the state

$$|\Psi(\Omega_{\min} - \Delta\Omega; \phi)\rangle = \frac{1}{2} [(a + be^{-i\Delta E_{\min}\tau}) |N0\rangle + e^{iN\phi} (be^{-i\Delta E_{\min}\tau} - a) |0N\rangle]. \quad (6.2)$$

Straightforward calculation of the Fisher information for this state gives

$$F_Q [|\Psi(\Omega_{\min} - \Delta\Omega; \phi)\rangle] = 4N^2 (|B|^2 - |B|^4), \quad (6.3)$$

where

$$|B|^2 = \frac{1}{2} |be^{-i\Delta E_{\min}\tau} - a|^2 = \frac{1}{2} (1 - 2\text{Re}\{ab^*e^{i\Delta E_{\min}\tau}\}). \quad (6.4)$$

Thus, we see that in order to recover Heisenberg precision ($F_Q = N^2$), we can choose a waiting time that satisfies $\Delta E_{\min}\tau = \pi/4 + \theta$, where θ is the argument of the complex number ab^* . This means that the maximum waiting time that might be needed to obtain Heisenberg limited precision is $\tau = \frac{7\pi}{4\Delta E_{\min}}$. According to our calculations, for $N = 12$ particles, an energy gap of $\Delta E_{\min} \approx 0.0005$,

and $\omega_{\perp} = 2\pi \times 210$ Hz, the waiting time is about $\tau \sim 8$ s. Although this time is still comparable to the typical lifetime of the condensate ~ 16 s, it is a massive improvement over the time that would take to adiabatically nucleate the entangled state (without optimization) in this case, which is $\sim 10^5$ s. In spite of these results being calculated with a simplified model of the system for a cat state, our preliminary calculations show that we obtain similar results from the simulation of the full dynamics of the system. This is exciting from an experimental point of view, and it has a high priority in our plans for future research.

6.2.3 Non-linear phase accumulation

When an unknown parameter is encoded in a quantum system that has N constituents and the Hamiltonian includes all the two-body interactions between the constituents, the parameter can be in principle measured with precision that scales as $N^{3/2}$, even if the system is not initially entangled (Boixo *et al.*, 2007; Luis, 2004). Also, it has been shown that protocols which do not generate entanglement can lead to improvements over the $1/N$ scaling by means of the dynamics alone (Boixo *et al.*, 2008). Therefore, our system with its two-body contact interactions and rich dynamics can lend itself to this type of enhancements. As a matter of fact, we have observed that if the quick rotation frequency shift in our interferometric scheme is performed rather slowly, we obtain a higher Fisher information for small waiting times after this frequency shift. A particular example of this is shown in Fig. (6.2), where it can be observed that a Fisher information greater than $\tau^2 N^2$ is achieved for values of τ up to 10 units, which is an improvement over the Heisenberg precision.

However, one must be careful not to misinterpret the amount of resources required in order to obtain this precision and claim sub-Heisenberg scaling, as it has been pointed out before (Zwierz *et al.*, 2010). Nevertheless, it is theoretically interesting to study this feature since the system offers the possibility of investigating the role of the time that the constituents spend interacting as a “resource” to achieve different scalings of the precision when the most important resource often considered, the number of particles, is fixed.

6.2.4 Decoherence factors

So far, we have mentioned that the bat-like state is more robust against particle losses than the cat-like one, which is the result of research carried out for BECs in ring geometries (Dunningham & Hallwood, 2006). However, the exact details of this robustness for the present case of a BEC in a rotating anisotropic trap are not known. Atoms lost in trapped BECs constitute one of the main relevant decoherence factors for our interferometric scheme, due to the degradation of the entanglement that it implies, and the fact that the exact critical frequency depends on the number of atoms, as well as the order of the quantum phase transition. In the near future, we would like to investigate the impact of three-body recombination processes on the performance of the interferometer. Three-body recombination is one of the main mechanisms responsible for the loss of atoms in the trap, and occurs when three atoms collide, two of them forming a molecule or dimer, and the released energy is carried away by the third atom, resulting in the loss of the three atoms from the condensate since the dimer generally ends up in an excited vibrational state, and the released energy is usually much larger than the typical depth of the trap (Soding *et al.*, 1999).

Another important decoherence mechanism has already been pointed out by (Dagnino *et al.*, 2009a), which is small second-order contributions of the laser fields that make up the stirring potential. This perturbation breaks the parity symmetry and connects terms in the Hamiltonian differing by one and three units of angular momentum. As it was shown by Dagnino and colleagues, the inclusion of a very small parity-breaking term has bold consequences on the features of the system near criticality. For one thing, unlike the case with no parity-breaking term, the energy gap at the avoided crossing closes as N increases, thus making the adiabatic nucleation of the entangled state much more difficult to attain. At the same time, the form of the entangled state changes and no longer resembles a bat-like state in the LLL regime, which is a consequence of the two-mode model not working as well as in the case with no parity-breaking term.

Due to the fact that even a very small parity-breaking perturbation can have the consequences mentioned above, it is important to investigate its effect on the performance of our interferometric scheme.

6.2.5 Miscellaneous

Finally, we would like to briefly mention a couple more ideas that constitute possible subjects for future research.

Being able to parallelise our code in order to speed up calculations and analyse larger numbers of particles or include larger angular momentum states in the basis would be very useful. Also, it could allow us to investigate ideas that were impractical to test using our current computational facilities.

Also, it is evident that small variations in the initial conditions or small uncertainties in parameters, such as the critical frequency or waiting times, can lead to substantial changes in the outcome of our interferometric scheme. Therefore, it is of interest to study the robustness of the scheme against these imperfections.

One last suggestion for the future concerns the study of entanglement tuning via changes in the anisotropy of the trap while the interaction strength is kept fixed. This is of great relevance from the experimental point of view, because it allows the nucleation of bat states farther away from the centrifugal limit, where dynamical instabilities can compromise the experiment. Moreover, tuning entanglement in this way also serves to set the critical frequency by changing the interaction strength without having to modify the frequency of the harmonic trap ω_{\perp} , which we want to be large so that nucleation times of entangled states are short.

Appendix A

Determination of the Matrix Elements

A.1 The anisotropic term

First, we determine the matrix elements of the anisotropic term using the wave functions of Eq.(3.34)

$$\begin{aligned} V_{\mathbf{k}_1\mathbf{k}_2} &= \langle \psi_{\mathbf{k}_1} | 2AM\omega_{xy}^2(x^2 - y^2) | \psi_{\mathbf{k}_2} \rangle = \int \psi_{\mathbf{k}_1}^*(\vec{x}) 2AM\omega_{xy}^2(x^2 - y^2) \psi_{\mathbf{k}_2}(\vec{x}) d^2\vec{x} \\ &= C_{\mathbf{k}_1}^* C_{\mathbf{k}_2} \int_0^{2\pi} \int_0^\infty e^{-im_{\mathbf{k}_1}\phi} R_{\mathbf{k}_1}^*(\rho, \phi) 2AM\omega_{xy}^2 \rho^2 \cos(2\phi) e^{im_{\mathbf{k}_2}\phi} R_{\mathbf{k}_2}(\rho, \phi) \rho d\rho d\phi, \end{aligned} \tag{A.1}$$

where we have used the trigonometric identity $x^2 - y^2 = \rho^2 \cos(2\phi)$ and $C_{\mathbf{k}}$ is the normalization constant of the wave function in Eq.(3.34). Next, we evaluate the radial and angular integral separately

$$V_{\mathbf{k}_1\mathbf{k}_2} = 2AM\omega_{xy}^2 C_{\mathbf{k}_1}^* C_{\mathbf{k}_2} \int_0^{2\pi} e^{i(m_{\mathbf{k}_2} - m_{\mathbf{k}_1})\phi} \cos(2\phi) d\phi \int_0^\infty R_{\mathbf{k}_1}^*(\rho, \phi) \rho^2 R_{\mathbf{k}_2}(\rho, \phi) \rho d\rho. \tag{A.2}$$

Defining $t = m_{\mathbf{k}_2} - m_{\mathbf{k}_1}$, the angular integral is

$$\begin{aligned}
 \int_0^{2\pi} e^{it\phi} \cos(2\phi) d\phi &= \int_0^{2\pi} \cos(t\phi) \cos(2\phi) d\phi + i \int_0^{2\pi} \sin(t\phi) \cos(2\phi) d\phi \\
 &= \int_0^{2\pi} \cos(t\phi) \cos(2\phi) d\phi \\
 &= \left[\left(\frac{\phi}{2} + \frac{\sin(4\phi)}{8} \right) \delta_{|t|,2} + \left(\frac{\sin(t-2)\phi}{2(t-2)} + \frac{\sin(t+2)\phi}{2(t+2)} \right) (1 - \delta_{|t|,2}) \right]_0^{2\pi} \\
 &= \pi \delta_{|t|,2} = \pi \delta_{m_{\mathbf{k}_2}, m_{\mathbf{k}_1} \pm 2}, \tag{A.3}
 \end{aligned}$$

where the $\sin(t\phi) \cos(2\phi)$ integral is zero because its integrand is odd. On the other hand, the radial integral can be expressed in a more convenient parameter-free way by changing variables as $\rho = \rho_0 x^{1/2}$,

$$\begin{aligned}
 \int_0^\infty R_{\mathbf{k}_1}^*(\rho, \phi) \rho^2 R_{\mathbf{k}_2}(\rho, \phi) \rho d\rho &= \int_0^\infty e^{-\frac{\rho^2}{\rho_0^2}} \rho^{|m_{\mathbf{k}_1}| + |m_{\mathbf{k}_2}| + 3} L_{n_{\mathbf{k}_1}}^{|m_{\mathbf{k}_1}|}(\rho^2/\rho_0^2) L_{n_{\mathbf{k}_2}}^{|m_{\mathbf{k}_2}|}(\rho^2/\rho_0^2) d\rho \\
 &= \frac{1}{2} \rho_0^{|m_{\mathbf{k}_1}| + |m_{\mathbf{k}_2}| + 4} I_1(\mathbf{k}_1, \mathbf{k}_2) \tag{A.4}
 \end{aligned}$$

where

$$I_1(\mathbf{k}_1, \mathbf{k}_2) = \int_0^\infty e^{-x} x^{\frac{|m_{\mathbf{k}_1}| + |m_{\mathbf{k}_2}| + 2}{2}} L_{n_{\mathbf{k}_1}}^{|m_{\mathbf{k}_1}|}(x) L_{n_{\mathbf{k}_2}}^{|m_{\mathbf{k}_2}|}(x) dx. \tag{A.5}$$

This last integral does not have a closed form for general values of \mathbf{k}_1 and \mathbf{k}_2 , however, it fairly simplifies when $n_{\mathbf{k}_1} = n_{\mathbf{k}_2} = 0$, the so-called Lowest Landau Level approximation. In this case I_1 reduces to

$$I_1(\mathbf{k}_1', \mathbf{k}_2') = \Gamma\left(\frac{|m_{\mathbf{k}_1}| + |m_{\mathbf{k}_2}| + 2}{2} + 1\right). \tag{A.6}$$

Finally, the anisotropic term in its second quantized form can be written as

$$\begin{aligned}
 \hat{V} &= \sum_{\mathbf{k}_1 \mathbf{k}_2} V_{\mathbf{k}_1 \mathbf{k}_2} a_{\mathbf{k}_1}^\dagger a_{\mathbf{k}_2} \\
 &= 2AM\omega_{xy}^2 \sum_{\mathbf{k}_1 \mathbf{k}_2} C_{\mathbf{k}_1}^* C_{\mathbf{k}_2} \frac{1}{2} \rho_0^{|m_{\mathbf{k}_1}| + |m_{\mathbf{k}_2}| + 4} I_1(\mathbf{k}_1, \mathbf{k}_2) \pi \left(\delta_{m_{\mathbf{k}_2}, m_{\mathbf{k}_1} \pm 2} \right) a_{\mathbf{k}_1}^\dagger a_{\mathbf{k}_2} \\
 &= A\hbar\omega_{xy} \sum_{\mathbf{k}_1 \mathbf{k}_2} \sqrt{\frac{n_{\mathbf{k}_1}! n_{\mathbf{k}_2}!}{(n_{\mathbf{k}_1} + |m_{\mathbf{k}_1}|)! (n_{\mathbf{k}_2} + |m_{\mathbf{k}_2}|)!}} I_1(\mathbf{k}_1, \mathbf{k}_2) \left(\delta_{m_{\mathbf{k}_2}, m_{\mathbf{k}_1} \pm 2} \right) a_{\mathbf{k}_1}^\dagger a_{\mathbf{k}_2} \tag{A.7}
 \end{aligned}$$

where we have used $\rho_0 = \sqrt{\frac{\hbar}{m\omega}}$.

A.2 The interaction term

The matrix elements of the interaction term are given by

$$\begin{aligned}
 U_{\mathbf{k}_1 \mathbf{k}_2 \mathbf{l}_1 \mathbf{l}_2} &= \int \int \psi_{\mathbf{k}_1}^*(\vec{\mathbf{x}}_1) \psi_{\mathbf{k}_2}^*(\vec{\mathbf{x}}_2) g \frac{\hbar^2}{M} \delta(\vec{\mathbf{x}}_2 - \vec{\mathbf{x}}_1) \psi_{\mathbf{l}_1}(\vec{\mathbf{x}}_1) \psi_{\mathbf{l}_2}(\vec{\mathbf{x}}_2) d^2 \vec{\mathbf{x}}_1 d^2 \vec{\mathbf{x}}_2 \\
 &= g \frac{\hbar^2}{M} C_{\mathbf{k}_1}^* C_{\mathbf{k}_2}^* C_{\mathbf{l}_1} C_{\mathbf{l}_2} \int_0^{2\pi} \int_0^\infty e^{i(m_{\mathbf{l}_2} + m_{\mathbf{l}_1} - m_{\mathbf{k}_1} - m_{\mathbf{k}_2})\phi} R_{\mathbf{k}_1}^*(\rho) R_{\mathbf{k}_2}^*(\rho) R_{\mathbf{l}_1}(\rho) R_{\mathbf{l}_2}(\rho) \rho d\rho d\phi.
 \end{aligned} \tag{A.8}$$

The angular integral is very easy to calculate and results in

$$\int_0^{2\pi} e^{i(m_{\mathbf{l}_2} + m_{\mathbf{l}_1} - m_{\mathbf{k}_1} - m_{\mathbf{k}_2})\phi} d\phi = 2\pi \delta_{m_{\mathbf{k}_1} + m_{\mathbf{k}_2}, m_{\mathbf{l}_1} + m_{\mathbf{l}_2}}. \tag{A.9}$$

Again, the radial integral can be conveniently expressed as a parameter-free expression using $\rho = \rho_0(x/2)^{1/2}$,

$$\int_0^\infty R_{\mathbf{k}_1}^*(\rho) R_{\mathbf{k}_2}^*(\rho) R_{\mathbf{l}_1}(\rho) R_{\mathbf{l}_2}(\rho) \rho d\rho = \left(\frac{1}{2}\right)^{\frac{\sum |m_t| + 4}{2}} \rho_0^{\sum |m_t| + 2} I_2(\mathbf{k}_1, \mathbf{k}_2, \mathbf{l}_1, \mathbf{l}_2), \tag{A.10}$$

where $\sum |m_t| = |m_{\mathbf{k}_1}| + |m_{\mathbf{k}_2}| + |m_{\mathbf{l}_1}| + |m_{\mathbf{l}_2}|$ and

$$I_2(\mathbf{k}_1, \mathbf{k}_2, \mathbf{l}_1, \mathbf{l}_2) = \int_0^\infty e^{-x} x^{\frac{\sum |m_t|}{2}} L_{n_{\mathbf{k}_1}}^{|m_{\mathbf{k}_1}|}\left(\frac{x}{2}\right) L_{n_{\mathbf{k}_2}}^{|m_{\mathbf{k}_2}|}\left(\frac{x}{2}\right) L_{n_{\mathbf{l}_1}}^{|m_{\mathbf{l}_1}|}\left(\frac{x}{2}\right) L_{n_{\mathbf{l}_2}}^{|m_{\mathbf{l}_2}|}\left(\frac{x}{2}\right) dx. \tag{A.11}$$

This last integral, just as in the case of the anisotropic term, does not have a closed form except for the case of the Lowest Landau Level approximation for which $n_{\mathbf{k}_1'} = n_{\mathbf{k}_2'} = n_{\mathbf{l}_1'} = n_{\mathbf{l}_2'} = 0$, in such case I_2 reduces to

$$I_2(\mathbf{k}_1', \mathbf{k}_2', \mathbf{l}_1', \mathbf{l}_2') = \Gamma\left(\frac{|m_{\mathbf{k}_1'}| + |m_{\mathbf{k}_2'}| + |m_{\mathbf{l}_1'}| + |m_{\mathbf{l}_2'}|}{2} + 1\right). \tag{A.12}$$

Consequently, the quantized interaction term reads

$$\begin{aligned}
 \hat{U} &= \frac{1}{2} \sum_{\mathbf{k}_1 \mathbf{k}_2} \sum_{\mathbf{l}_1 \mathbf{l}_2} U_{\mathbf{k}_1 \mathbf{k}_2 \mathbf{l}_1 \mathbf{l}_2} \hat{a}_{\mathbf{k}_1}^\dagger \hat{a}_{\mathbf{k}_2}^\dagger \hat{a}_{\mathbf{l}_1} \hat{a}_{\mathbf{l}_2} \\
 &= \frac{g\hbar\omega_{xy}}{4\pi} \sum_{\mathbf{k}_1 \mathbf{k}_2} \sum_{\mathbf{l}_1 \mathbf{l}_2} \frac{1}{2^{\frac{\sum |m_t|}{2}}} \sqrt{\prod_t \frac{n_t!}{(n_t + |m_t|)!}} I_2(\mathbf{k}_1, \mathbf{k}_2, \mathbf{l}_1, \mathbf{l}_2) \delta_{m_{\mathbf{k}_1} + m_{\mathbf{k}_2}, m_{\mathbf{l}_1} + m_{\mathbf{l}_2}} \hat{a}_{\mathbf{k}_1}^\dagger \hat{a}_{\mathbf{k}_2}^\dagger \hat{a}_{\mathbf{l}_1} \hat{a}_{\mathbf{l}_2},
 \end{aligned} \tag{A.13}$$

where

$$\prod_t \frac{n_t!}{(n_t + |m_t|)!} = \frac{n_{\mathbf{k}_1}! n_{\mathbf{k}_2}! n_{\mathbf{l}_1}! n_{\mathbf{l}_2}!}{(n_{\mathbf{k}_1} + |m_{\mathbf{k}_1}|)! (n_{\mathbf{k}_2} + |m_{\mathbf{k}_2}|)! (n_{\mathbf{l}_1} + |m_{\mathbf{l}_1}|)! (n_{\mathbf{l}_2} + |m_{\mathbf{l}_2}|)!} \quad (\text{A.14})$$

References

- AFTALION, A., BLANC, X. & DALIBARD, J. (2005). Vortex patterns in a fast rotating Bose-Einstein condensate. *PHYSICAL REVIEW A*, **71**. [51](#)
- AMICO, L., FAZIO, R., OSTERLOH, A. & VEDRAL, V. (2008). Entanglement in many-body systems. *REVIEWS OF MODERN PHYSICS*, **80**, 517–576. [3](#)
- ANDERSON, M., ENSHER, J., MATTHEWS, M., WIEMAN, C. & CORNELL, E. (1995). Observation of bose-einstein condensation in a dilute atomic vapor. *SCIENCE*, **269**, 198–201. [6](#), [8](#)
- ANDREWS, M., TOWNSEND, C., MIESNER, H., DURFEE, D., KURN, D. & KETTERLE, W. (1997). Observation of interference between two Bose condensates. *SCIENCE*, **275**, 637–641. [11](#)
- ARFKEN, G. (1985). *Mathematical Methods for Physicists*. Academic Press. [41](#)
- ASPECT, A., GRANGIER, P. & ROGER, G. (1981). Experimental tests of realistic local theories via bells theorem. *PHYSICAL REVIEW LETTERS*, **47**, 460–463. [2](#)
- BARNDORFF-NIELSEN, O. & GILL, R. (2000). Fisher information in quantum statistics. *JOURNAL OF PHYSICS A-MATHEMATICAL AND GENERAL*, **33**, 4481–4490. [140](#)
- BELL, J. (1966). On problem of hidden variables in quantum mechanics. *REVIEWS OF MODERN PHYSICS*, **38**, 447–&. [2](#)

REFERENCES

- BENNET, C. & WIESNER, S. (1992). Communication via one-particle and 2-particle operators on einstein-podolsky-rosen states. *PHYSICAL REVIEW LETTERS*, **69**, 2881–2884. [3](#)
- BENNET, C., BRASSARD, G. & MERMIN, N. (1992). Quantum cryptography without bell theorem. *PHYSICAL REVIEW LETTERS*, **68**, 557–559. [3](#)
- BENNET, C., BRASSARD, G., CREPEAU, C., JOZSA, R., PERES, A. & WOOTERS, W. (1993). Teleporting an unknown quantum state via dual classical and einstein-podolsky-rosen channels. *PHYSICAL REVIEW LETTERS*, **70**, 1895–1899. [3](#)
- BERTSCH, G. & PAPENBROCK, T. (1999). Yrast line for weakly interacting trapped bosons. *PHYSICAL REVIEW LETTERS*, **83**, 5412–5414. [56](#)
- BOGOLIUBOV, N. (1947). On the theory of superfluidity. *JOURNAL OF PHYSICS*, **11**. [9](#)
- BOIXO, S., FLAMMIA, S.T., CAVES, C.M. & GEREMIA, J.M. (2007). Generalized limits for single-parameter quantum estimation. *PHYSICAL REVIEW LETTERS*, **98**. [144](#)
- BOIXO, S., DATTA, A., DAVIS, M.J., FLAMMIA, S.T., SHAJI, A. & CAVES, C.M. (2008). Quantum metrology: Dynamics versus entanglement. *PHYSICAL REVIEW LETTERS*, **101**. [144](#)
- BOLLINGER, J., ITANO, W., WINELAND, D. & HEINZEN, D. (1996). Optimal frequency measurements with maximally correlated states. *PHYSICAL REVIEW A*, **54**, R4649–R4652. [22](#)
- BOSE, S. (1924). Thermal equilibrium of the radiation field in the presence of matter. *ZEITSCHRIFT FUR PHYSIK*, **27**, 384–392. [6](#)
- BRADLEY, C., SACKETT, C., TOLLETT, J. & HULET, R. (1995). Evidence of bose-einstein condensation in an atomic gas with attractive interactions. *PHYSICAL REVIEW LETTERS*, **75**, 1687–1690. [6](#)

REFERENCES

- BRAUNSTEIN, S. & CAVES, C. (1994). Statistical distance and the geometry of quantum states. *PHYSICAL REVIEW LETTERS*, **72**, 3439–3443. [28](#), [30](#)
- BRETIN, V., STOCK, S., SEURIN, Y. & DALIBARD, J. (2004). Fast rotation of a Bose-Einstein condensate. *PHYSICAL REVIEW LETTERS*, **92**. [86](#), [108](#), [109](#)
- BRUUS, H. & FLENSBERG, K. (2004). *Many-Body Quantum Theory in Condensed Matter Physics*. Oxford University Press. [37](#)
- BURT, E., GHRIST, R., MYATT, C., HOLLAND, M., CORNELL, E. & WIEMAN, C. (1997). Coherence, correlations, and collisions: What one learns about Bose-Einstein condensates from their decay. *PHYSICAL REVIEW LETTERS*, **79**, 337–340. [11](#)
- CABLE, H. & DOWLING, J.P. (2007). Efficient generation of large number-path entanglement using only linear optics and feed-forward. *PHYSICAL REVIEW LETTERS*, **99**. [5](#)
- CAVES, C. (1981). Quantum-Mechanical noise in an interferometer. *PHYSICAL REVIEW D*, **23**, 1693–1708. [4](#), [5](#)
- CHEVY, F., MADISON, K. & DALIBARD, J. (2000). Measurement of the angular momentum of a rotating Bose-Einstein condensate. *PHYSICAL REVIEW LETTERS*, **85**, 2223–2227. [60](#), [76](#), [86](#), [108](#), [142](#)
- CHOU, C.W., HUME, D.B., ROSEN BAND, T. & WINELAND, D.J. (2010). Optical Clocks and Relativity. *SCIENCE*, **329**, 1630–1633. [4](#)
- COOPER, J.J., HALLWOOD, D.W. & DUNNINGHAM, J.A. (2010). Entanglement-enhanced atomic gyroscope. *PHYSICAL REVIEW A*, **81**. [5](#), [31](#), [32](#), [35](#)
- COOPER, N.R. (2008). Rapidly rotating atomic gases. *ADVANCES IN PHYSICS*, **57**, 539–616. [34](#), [35](#), [142](#)

REFERENCES

- CORNISH, S., CLAUSSEN, N., ROBERTS, J., CORNELL, E. & WIEMAN, C. (2000). Stable Rb-85 Bose-Einstein condensates with widely tunable interactions. *PHYSICAL REVIEW LETTERS*, **85**, 1795–1798. [10](#), [11](#), [84](#)
- CRONIN, A.D., SCHMIEDMAYER, J. & PRITCHARD, D.E. (2009). Optics and interferometry with atoms and molecules. *REVIEWS OF MODERN PHYSICS*, **81**, 1051–1129. [6](#)
- DAGNINO, D., BARBERAN, N., LEWENSTEIN, M. & DALIBARD, J. (2009a). Vortex nucleation as a case study of symmetry breaking in quantum systems. *NATURE PHYSICS*, **5**, 431–437. [36](#), [37](#), [50](#), [60](#), [66](#), [70](#), [73](#), [79](#), [80](#), [103](#), [106](#), [138](#), [145](#)
- DAGNINO, D., BARBERAN, N., LEWENSTEIN, M. & DALIBARD, J. (2009b). Vortex nucleation as a case study of symmetry breaking in quantum systems. *NATURE PHYSICS*, **5**, 431–437. [64](#), [65](#), [142](#)
- DALIBARD, J. (1999). Collisional dynamics of ultra-cold atomic gases. *PROCEEDINGS OF THE INTERNATIONAL SCHOOL OF PHYSICS ENRICO FERMI*, 321. [9](#)
- DAVIS, K., MEWES, M., ANDREWS, M., VANDRUTEN, N., DURFEE, D., KURN, D. & KETTERLE, W. (1995). Bose-Einstein condensation in a gas of sodium atoms. *PHYSICAL REVIEW LETTERS*, **75**, 3969–3973. [6](#)
- DEUTSCH, D. (1985). Quantum-Theory, the church-turing principle and the universal quantum computer. *PROCEEDINGS OF THE ROYAL SOCIETY OF LONDON SERIES A-MATHEMATICAL PHYSICAL AND ENGINEERING SCIENCES*, **400**, 97–117. [3](#)
- DOWLING, J. (1998). Correlated input-port, matter-wave interferometer: Quantum-noise limits to the atom-laser gyroscope. *PHYSICAL REVIEW A*, **57**, 4736–4746. [12](#), [17](#), [19](#), [20](#), [21](#)
- DUBETSKY, B. & KASEVICH, M.A. (2006). Atom interferometer as a selective sensor of rotation or gravity. *PHYSICAL REVIEW A*, **74**. [78](#)

REFERENCES

- DUNNINGHAM, J. & BURNETT, K. (2004). Sub-shot-noise-limited measurements with Bose-Einstein condensates. *PHYSICAL REVIEW A*, **70**. [27](#)
- DUNNINGHAM, J. & HALLWOOD, D. (2006). Creation of macroscopic superpositions of flow states with Bose-Einstein condensates. *PHYSICAL REVIEW A*, **74**. [5](#), [36](#), [78](#), [145](#)
- DUNNINGHAM, J. & KIM, T. (2006). Using quantum interferometers to make measurements at the Heisenberg limit. *JOURNAL OF MODERN OPTICS*, **53**, 557–571. [23](#), [24](#)
- DUNNINGHAM, J.A. (2006). Using quantum theory to improve measurement precision. *CONTEMPORARY PHYSICS*, **47**, 257–267. [3](#), [19](#), [25](#)
- DUNNINGHAM J.A., C.J. & D.W., H. (2011). . *arXiv:1102.0164v1*. [36](#)
- EINSTEIN, A. (1925). Quantum theory of the ideal gas. *SITZUNGSBERICHTE DER PREUSSISCHEN AKADEMIE DER WISSENSCHAFTEN PHYSIKALISCH-MATHEMATISCHE KLASSE*, 18–25. [6](#)
- EINSTEIN, A., PODOLSKY, B. & ROSEN, N. (1935). Can quantum-mechanical description of physical reality be considered complete? *PHYSICAL REVIEW*, **47**, 0777–0780. [1](#)
- EKERT, A. (1991). Quantum cryptography based on bell theorem. *PHYSICAL REVIEW LETTERS*, **67**, 661–663. [3](#)
- FETTER, A.L. (2009). Rotating trapped Bose-Einstein condensates. *REVIEWS OF MODERN PHYSICS*, **81**, 647–691. [37](#), [44](#), [51](#), [52](#), [142](#)
- FETTER, A.L. (2010). Bose-Einstein condensate in a rapidly rotating nonsymmetric trap. *PHYSICAL REVIEW A*, **81**. [60](#)
- FEYNMAN, R. (1982). Simulating physics with computers. *INTERNATIONAL JOURNAL OF THEORETICAL PHYSICS*, **21**, 467–488. [3](#)
- GEMELKE, S.E., N & CHU, S. (2010). Using quantum interferometers to make measurements at the Heisenberg limit. *arXiv:1007.2677*, , . [60](#), [109](#), [135](#)

REFERENCES

- GIOVANNETTI, V. & MACCONE, L. (2012). Sub-Heisenberg Estimation Strategies Are Ineffective. *PHYSICAL REVIEW LETTERS*, **108**. [22](#)
- GIOVANNETTI, V., LLOYD, S. & MACCONE, L. (2011). Advances in quantum metrology. *NATURE PHOTONICS*, **5**, 222–229. [3](#)
- GLAUBER, R. (1963). Coherent and incoherent states of radiation field. *PHYSICAL REVIEW*, **131**, 2766–&. [20](#)
- GROSS, C., ZIBOLD, T., NICKLAS, E., ESTEVE, J. & OBERTHALER, M.K. (2010). Nonlinear atom interferometer surpasses classical precision limit. *NATURE*, **464**, 1165–1169. [12](#)
- GUSTAVSON, T., LANDRAGIN, A. & KASEVICH, M. (2000). Rotation sensing with a dual atom-interferometer Sagnac gyroscope. *CLASSICAL AND QUANTUM GRAVITY*, **17**, 2385–2398, International Symposium on Experimental Gravitation, SAMARKAND, UZBEKISTAN, AUG 16-21, 1999. [4](#), [35](#)
- HALLWOOD, D.W., BURNETT, K. & DUNNINGHAM, J. (2006). Macroscopic superpositions of superfluid flows. *NEW JOURNAL OF PHYSICS*, **8**. [81](#)
- HALLWOOD, D.W., ERNST, T. & BRAND, J. (2010). Robust mesoscopic superposition of strongly correlated ultracold atoms. *PHYSICAL REVIEW A*, **82**. [35](#)
- HELSTROM, C. (1967). Minimum mean-squared error of estimates in quantum statistics. *PHYSICS LETTERS A*, **A 25**, 101–&. [28](#)
- HO, T. (2001). Bose-Einstein condensates with large number of vortices. *PHYSICAL REVIEW LETTERS*, **87**. [53](#)
- HOLLAND, M. & BURNETT, K. (1993). Interferometric detection of optical-phase shifts at the heisenberg limit. *PHYSICAL REVIEW LETTERS*, **71**, 1355–1358. [36](#)
- HORODECKI, R., HORODECKI, P., HORODECKI, M. & HORODECKI, K. (2009). Quantum entanglement. *REVIEWS OF MODERN PHYSICS*, **81**, 865–942. [3](#)

REFERENCES

- JACKSON, A. & KAVOULAKIS, G. (2000). Analytical results for the interaction energy of a trapped, weakly interacting Bose-Einstein condensate. *PHYSICAL REVIEW LETTERS*, **85**, 2854–2856. [50](#), [56](#)
- JOO, J., MUNRO, W.J. & SPILLER, T.P. (2011). Quantum Metrology with Entangled Coherent States. *PHYSICAL REVIEW LETTERS*, **107**. [5](#)
- KACPROWICZ, M., DEMKOWICZ-DOBRZANSKI, R., WASILEWSKI, W., BANASZEK, K. & WALMSLEY, I.A. (2010). Experimental quantum-enhanced estimation of a lossy phase shift. *NATURE PHOTONICS*, **4**, 357–360. [5](#)
- KETTERLE, W. (2002). Nobel lecture: When atoms behave as waves: Bose-Einstein condensation and the atom laser. *REVIEWS OF MODERN PHYSICS*, **74**, 1131–1151. [6](#)
- KIM, T., SHIN, J., HA, Y., KIM, H., PARK, G., NOH, T. & HONG, C. (1998). The phase-sensitivity of a Mach-Zehnder interferometer for the Fock state inputs. *OPTICS COMMUNICATIONS*, **156**, 37–42. [26](#), [27](#)
- KIM, T., HA, Y., SHIN, J., KIM, H., PARK, G., KIM, K., NOH, T. & HONG, C. (1999). Effect of the detector efficiency on the phase sensitivity in a Mach-Zehnder interferometer. *PHYSICAL REVIEW A*, **60**, 708–711. [27](#), [140](#)
- KWIAT, P., MATTLE, K., WEINFURTER, H., ZEILINGER, A., SERGIENKO, A. & SHIH, Y. (1995). New high-intensity source of polarization-entangled photon pairs. *PHYSICAL REVIEW LETTERS*, **75**, 4337–4341. [2](#)
- LUATI, A. (2004). Maximum Fisher information in mixed state quantum systems. *ANNALS OF STATISTICS*, **32**, 1770–1779. [140](#)
- LUECKE, B., SCHERER, M., KRUSE, J., PEZZE, L., DEURETZBACHER, F., HYLLUS, P., TOPIC, O., PEISE, J., ERTMER, W., ARLT, J., SANTOS, L., SMERZI, A. & KLEMP, C. (2011). Twin Matter Waves for Interferometry Beyond the Classical Limit. *SCIENCE*, **334**, 773–776. [27](#)
- LUIS, A. (2004). Nonlinear transformations and the Heisenberg limit. *PHYSICS LETTERS A*, **329**, 8–13. [144](#)

REFERENCES

- MADISON, K., CHEVY, F., WOHLLEBEN, W. & DALIBARD, J. (2000a). Vortex formation in a stirred Bose-Einstein condensate. *PHYSICAL REVIEW LETTERS*, **84**, 806–809. [36](#), [142](#)
- MADISON, K., CHEVY, F., WOHLLEBEN, W. & DALIBARD, J. (2000b). Vortex formation in a stirred Bose-Einstein condensate. *PHYSICAL REVIEW LETTERS*, **84**, 806–809. [104](#)
- MARTIN, P. & ROTHEN, F. (2004). *Many-Body problems and Quantum Field Theory*. [67](#), [68](#)
- MESSIAH, A. (1965). *Quantum Mechanics*. John Wiley and Sons. [104](#)
- MITCHELL, M., LUNDEEN, J. & STEINBERG, A. (2004a). Super-resolving phase measurements with a multiphoton entangled state. *NATURE*, **429**, 161–164. [5](#)
- MITCHELL, M., LUNDEEN, J. & STEINBERG, A. (2004b). Super-resolving phase measurements with a multiphoton entangled state. *NATURE*, **429**, 161–164. [25](#)
- MORRIS, A.G. & FEDER, D.L. (2006). Validity of the lowest-Landau-level approximation for rotating Bose gases. *PHYSICAL REVIEW A*, **74**. [50](#), [53](#), [54](#), [56](#), [82](#), [90](#), [91](#), [92](#)
- NAGATA, T., OKAMOTO, R., O'BRIEN, J.L., SASAKI, K. & TAKEUCHI, S. (2007). Beating the standard quantum limit with four-entangled photons. *SCIENCE*, **316**, 726–729. [5](#)
- NIELSEN, M. & IL, C. (2000). *Quantum Computations and Quantum Information*. Cambridge University Press. [3](#)
- NUNNENKAMP, A., REY, A.M. & BURNETT, K. (2008). Generation of macroscopic superposition states in ring superlattices. *PHYSICAL REVIEW A*, **77**. [36](#), [76](#)

REFERENCES

- OKAMOTO, R., HOFMANN, H.F., NAGATA, T., O'BRIEN, J.L., SASAKI, K. & TAKEUCHI, S. (2008). Beating the standard quantum limit: phase super-sensitivity of N-photon interferometers. *NEW JOURNAL OF PHYSICS*, **10**. [5](#)
- OU, Z. & MANDEL, L. (1988). Violation of bells-inequality and classical probability in a 2-photon correlation experiment. *PHYSICAL REVIEW LETTERS*, **61**, 50–53. [2](#)
- PARKE, M.I., WILKIN, N.K., GUNN, J.M.F. & BOURNE, A. (2008). Exact vortex nucleation and cooperative vortex tunneling in dilute Bose-Einstein condensates. *PHYSICAL REVIEW LETTERS*, **101**. [56](#), [60](#), [63](#)
- PENROSE, O. & ONSAGER, L. (1956). Bose-Einstein condensation and liquid helium. *PHYSICAL REVIEW*, **104**, 576–584. [69](#)
- PENROSE, R. (2001). Consciousness, the brain, and spacetime geometry: An addendum - Some new developments on the Orch OR model for consciousness. In Marijuan, PC, ed., *CAJAL AND CONSCIOUSNESS: SCIENTIFIC APPROACHES TO CONSCIOUSNESS ON THE CENTENNIAL OF RAMON Y CAJAL'S TEXTURA*, vol. 929 of *ANNALS OF THE NEW YORK ACADEMY OF SCIENCES*, 105–110. [2](#)
- PETHICK, C. & SMITH, H. (2008). *Bose-Einstein Condensation in Dilute Gases*. Cambridge University Press. [6](#), [8](#), [9](#), [10](#), [33](#), [37](#), [51](#)
- RICO-GUTIERREZ, L.M., SPILLER, T.P. & DUNNINGHAM, J.A. (2013). Engineering entanglement for metrology with rotating matter waves. *NEW JOURNAL OF PHYSICS*, **15**. [36](#), [73](#), [74](#), [78](#), [79](#), [80](#), [87](#), [91](#), [93](#), [95](#), [97](#)
- ROBINS, N.P., ALTIN, P.A., DEBS, J.E. & CLOSE, J.D. (2013). Atom lasers: Production, properties and prospects for precision inertial measurement. *PHYSICS REPORTS-REVIEW SECTION OF PHYSICS LETTERS*, **529**, 265–296. [6](#)

REFERENCES

- ROSENBAND, T., HUME, D.B., SCHMIDT, P.O., CHOU, C.W., BRUSCH, A., LORINI, L., OSKAY, W.H., DRULLINGER, R.E., FORTIER, T.M., STALNAKER, J.E., DIDDAMS, S.A., SWANN, W.C., NEWBURY, N.R., ITANO, W.M., WINELAND, D.J. & BERGQUIST, J.C. (2008). Frequency ratio of Al⁺ and Hg⁺ single-ion optical clocks; Metrology at the 17th decimal place. *SCIENCE*, **319**, 1808–1812. [4](#)
- ROSENBUSCH, P., PETROV, D., SINHA, S., CHEVY, F., BRETIN, V., CASTIN, Y., SHLYAPNIKOV, G. & DALIBARD, J. (2002). Critical rotation of a harmonically trapped Bose gas. *PHYSICAL REVIEW LETTERS*, **88**. [94](#)
- SACKETT, C., KIELPINSKI, D., KING, B., LANGER, C., MEYER, V., MYATT, C., ROWE, M., TURCHETTE, Q., ITANO, W., WINELAND, D. & MONROE, C. (2000). Experimental entanglement of four particles. *NATURE*, **404**, 256–259. [25](#)
- SAKURAI, J. (1967). *Modern Quantum Mechanics*. Addison-Wesley. [20](#)
- SCHRÖEDINGER, E. (1935). The current situation in quantum mechanics. *NATURWISSENSCHAFTEN*, **23**, 807–812. [1](#)
- SCHWEIKHARD, V., CODDINGTON, I., ENGELS, P., MOGENDORFF, V. & CORNELL, E. (2004). Rapidly rotating Bose-Einstein condensates in and near the lowest Landau level. *PHYSICAL REVIEW LETTERS*, **92**. [34](#)
- SHOR, P. (1995). Scheme for reducing decoherence in quantum computer memory. *PHYSICAL REVIEW A*, **52**, R2493–R2496. [3](#)
- SINHA, S. & CASTIN, Y. (2001). Dynamic instability of a rotating Bose-Einstein condensate. *PHYSICAL REVIEW LETTERS*, **87**. [94](#)
- SODING, J., GUERY-ODELIN, D., DESBIOLLES, P., CHEVY, F., INAMORI, H. & DALIBARD, J. (1999). Three-body decay of a rubidium Bose-Einstein condensate. *APPLIED PHYSICS B-LASERS AND OPTICS*, **69**, 257–261. [108](#), [145](#)

REFERENCES

- SPEKKENS, R. & SIPE, J. (1999). Spatial fragmentation of a Bose-Einstein condensate in a double-well potential. *PHYSICAL REVIEW A*, **59**, 3868–3877. [22](#)
- STWALLEY, W. (1976). Stability of spin-aligned hydrogen at low-temperatures and high magnetic-fields - new field-dependent scattering resonances and pre-dissociations. *PHYSICAL REVIEW LETTERS*, **37**, 1628–1631. [10](#)
- TITTEL, W., BRENDEL, J., ZBINDEN, H. & GISIN, N. (1998). Violation of bell inequalities by photons more than 10 km apart. *PHYSICAL REVIEW LETTERS*, **81**, 3563–3566. [2](#)
- UEDA, M. & NAKAJIMA, T. (2006). Nambu-Goldstone mode in a rotating dilute Bose-Einstein condensate. *PHYSICAL REVIEW A*, **73**. [57](#), [66](#)
- WILKIN, N. & GUNN, J. (2000). Condensation of composite bosons in a rotating BEC. *PHYSICAL REVIEW LETTERS*, **84**, 6–9. [56](#), [58](#)
- WILKIN, N., GUNN, J. & SMITH, R. (1998). Do attractive bosons condense? *PHYSICAL REVIEW LETTERS*, **80**, 2265–2268. [10](#), [59](#)
- YANG, C. (1962). Concept of off-diagonal long-range order and quantum phases of liquid he and of superconductors. *REVIEWS OF MODERN PHYSICS*, **34**, 694–&. [66](#), [68](#)
- YURKE, B. (1986). Input states for enhancement of fermion interferometer sensitivity. *PHYSICAL REVIEW LETTERS*, **56**, 1515–1517. [5](#), [22](#)
- YURKE, B. & STOLER, D. (1992). Einstein-Podolsky-Rosen effects from independent particle sources. *PHYSICAL REVIEW LETTERS*, **68**, 1251–1254. [3](#)
- YURKE, B., MCCALL, S. & KLAUDER, J. (1986). SU(2) and SU(1,1) interferometers. *PHYSICAL REVIEW A*, **33**, 4033–4054. [5](#), [22](#)
- ZANARDI, P. (2001). Entanglement of quantum evolutions. *PHYSICAL REVIEW A*, **63**. [73](#)

REFERENCES

- ZIMMER, F.E. & FLEISCHHAUER, M. (2006). Quantum sensitivity limit of a Sagnac hybrid interferometer based on slow-light propagation in ultracold gases. *PHYSICAL REVIEW A*, **74**. [36](#)
- ZWIERZ, M., PEREZ-DELGADO, C.A. & KOK, P. (2010). General Optimality of the Heisenberg Limit for Quantum Metrology. *PHYSICAL REVIEW LETTERS*, **105**. [144](#)